ALMA MATER STUDIORUM
UNIVERSITÀ DI BOLOGNA

DOTTORATO DI RICERCA IN

INGEGNERIA BIOMEDICA, ELETTRICA E DEI SISTEMI

Ciclo 36

Settore Concorsuale: 09/E2 - INGEGNERIA DELL'ENERGIA ELETTRICA

Settore Scientifico Disciplinare: ING-IND/33 - SISTEMI ELETTRICI PER L'ENERGIA

STABILITY AND OPERATION OF POWER SYSTEMS WITH A HIGH SHARE OF RENEWABLE ENERGY SOURCES AND STORAGE SYSTEMS AT THE TRANSMISSION AND DISTRIBUTION LEVEL

Presentata da: Tadeo Pontecorvo

Coordinatore Dottorato

Michele Monaci

Supervisore

Carlo Alberto Nucci

Co-supervisore

Fabio Napolitano

Esame finale anno 2024

Abstract

This thesis investigates two interrelated aspects of power systems with a high share of renewable energy sources and storage systems at both the transmission and distribution levels. The study comprises: *i*) enhancing frequency stability in transmission networks and *ii*) optimizing energy utilization within Renewable Energy Communities (RECs).

The first part of the dissertation focuses on developing a novel control architecture enabling wind power plants and grid-scale battery energy storage systems to provide synthetic inertial response, thereby addressing frequency stability concerns. By emulating the inertial response of traditional synchronous generators, wind turbines utilize kinetic and electrostatic energy to stabilize grid frequency. Simulation studies conducted on benchmark networks and real-world transmission grids demonstrate the effectiveness of the proposed control scheme in improving both small-signal and transient stability.

In the second part, the thesis delves into the operational management of RECs, proposing and validating an Energy Management System (EMS) to optimize energy distribution within these communities. The EMS operates in real-time, leveraging forecasted energy production, consumption data, and market prices to minimize procurement costs while maximizing renewable energy utilization. Extensive testing using Software-in-the-Loop (SIL) and Power Hardware-in-the-Loop (PHIL) configurations validates the system's reliability and effectiveness in real-world REC scenarios. Challenges such as establishing a robust online metering network and dependency on accurate forecast data are discussed, providing insights for future development.

The research contributes valuable insights into the evolving landscape of power systems with significant RES integration. The proposed control architecture and validated EMS offer practical solutions for addressing current and future challenges in renewable energy management. Furthermore, the adaptability of the EMS to evolving regulatory frameworks underscores its potential for broader implementation across different regions. This research sets the stage for further advancements in enhancing the resilience and reliability of renewable energy systems in power networks.

Acknowledgment

I extend my deepest gratitude to the LISEP group at the University of Bologna, especially my primary advisor, Prof. Carlo Alberto Nucci, alongside my co-supervisor Prof. Fabio Napolitano, their guidance and suggestions have been vital to navigate the projects undertaken during these years. My appreciation also goes to Prof. Alberto Borghetti and Prof. Fabio Tossani as well as my fellow PhD colleagues, with an honorable mention to Eng. Andrea Prevedi. The collaborative effort of this group has been pivotal in the completion of this thesis. The support I received has been instrumental not just in my scientific pursuits but in broader aspects of life.

I am very thankful to Prof. João Abel Peças Lopes and to Eng. Justino Miguel Rodrigues for welcoming me at INESC TEC in Porto. This hands-on and international experience significantly broadened my professional and personal horizons.

With heartfelt warmth, I acknowledge all those who have played a role in my personal and professional development. Their support has been crucial in navigating the demanding journey of doctoral studies.

This work is dedicated to my parents as a token of appreciation and love.

Contents

List of Acronyms

AC	Alternating Current
AGC	Automatic Generation Control
BESS	Battery Energy Storage System
CAAB	Centro Agroalimentare Bologna
CCM	Current-Controlled Mode
CEC	Citizen Energy Community
CEP	Clean Energy Package
DC	Direct Current
DFIG	Doubly-Fed Induction Generator
DP	Dispatching Profile
DSO	Distribution System Operator
EE	Electrostatic Energy
EM	Electro-Mechanical
EMS	Energy Management System
ESS	Energy Storage Systems
EIT	European Institute of Innovation
EU	European Union
FCWT	Full Converter Wind Turbine
FICO	Fabbrica Italiana Contadina
GECO	Green Energy Community
GSC	Grid-Side Converter
GSE	Gestore dei Servizi Energetici
HE	High Export
HI	High Import
HL	High Load
IEMD	Internal Electricity Market Directive
IR	Inertial Response
KE	Kinetic Energy
LISEP	Laboratorio di Ingegneria dei Sistemi Elettrici di Potenza
LL	Low Load
LooS	Lines out of Service
MC	Monte Carlo
MPPT	Maximum Power Point Tracking
PFR	Primary Frequency Response
PHIL	Power Hardware in the Loop
PI	Proportional-Integral
PLL	Phase-Locked Loop
PV	Photovoltaic
PWM	Pulse Width Modulation
REC	Renewable Energy Community
RED II	Renewable Energy Directive II
RES	Renewable Energy Sources
RKC	Rotor Kinetic Energy Control
RoCoF	Rate of Change of Frequency
RSC	Rotor-Side Converter
SG	Synchronous Generator
SGEVEL	Smart Grid and Electric Vehicle Laboratory
SI	Synthetic Inertia
SIL	Software in the Loop
SoC	State of Charge
SVPWM	Space Vector Pulse Width Modulation
UNIBO	University of Bologna
VCM	Voltage-Controlled Mode
VSWT	Variable Speed Wind Turbine
WF	Wind Farm
WPP	Wind Power Plant
WT	Wind Turbine

Chapter 1. Introduction

The development of electrical energy production and consumption has been recognized as the most significant innovation of the 20th century [1]. It has not only revolutionized the way we live and work but has also become a fundamental indicator of societal progress and well-being. As we venture deeper into the 21st century, the electrical energy landscape is poised for another monumental shift. With a global increase in electrical energy consumption and a decisive shift from conventional energy production to a more sustainable, renewable model, the traditional mechanisms of ensuring power system stability and reliability are undergoing a significant transformation [2].

This dissertation is structured into two distinct yet interrelated parts, each targeting key aspects of the energy transition and offering innovative solutions. The first part focuses on Synthetic Inertia (SI) support provided by Renewable Energy Sources (RES), thus on the generation and transmission level of power systems, while the second part is centered on Energy Management Systems (EMS) for Renewable Energy communities (REC), therefore more on the consumption and distribution level of the grid.

Historically, the stability of power grids has been largely dependent on synchronous generators. These generators, through their rotational inertia, have been integral in maintaining frequency stability. However, as the energy sector pivots towards renewable sources, mainly solar and wind, which are interfaced to the grid via power electronic converters, phasing out conventional power plants, a critical challenge emerges. This transition leads to a reduction in the overall system inertia, posing new complexities in maintaining the stability of power systems [3], [4].

In the first part, we address these challenges with emphasis on the frequency and small-signal stability of power systems. Recognizing the decreasing role of traditional synchronous generators and the growing centrality of RES, this part proposes a coordinated SI control strategy tailored for variable-speed wind turbines. This strategy is pivotal in supplementing the grid's inertia and ensuring frequency stability in scenarios where renewable sources are prevalent.

The efficacy of this coordinated SI control approach has been rigorously tested and validated. This validation is twofold: firstly, through benchmark test networks that provide a standardized basis for comparison, and secondly, via application to more intricate and realistic models, specifically of the Sicilian power grid. The latter focuses on forecast scenarios for the years 2030 and 2050, thereby capturing a future landscape where RES play a central role. These analyses not only underscore the feasibility of the proposed control strategy but also highlight its effectiveness in maintaining grid stability under various future energy scenarios. Through a combination of dynamic simulations and modal analysis the impact of the proposed SI control is assessed, particularly in a network with a high renewable energy penetration. Additionally, the role of grid-scale energy storage, and how they can operate in conjunction with wind power plants to enhance system stability has been explored.

The second part of the thesis shifts the focus to the distribution level of the grid, exploring the potential of RECs. These communities, which have been gaining increasing attention in recent years, represent a significant shift in how energy is produced, shared, and managed increasing direct energy utilization and efficiency. The research proposes and evaluates a novel EMS tailored for RECs, aimed at optimizing the operation of the distributed energy resources. The performance and reliability of the EMS are assessed through both Software-in-the-Loop (SIL) and Power Hardware-in-the-Loop (PHIL) real-time testing. This comprehensive evaluation not only validates the EMS but also provides insights into the effective integration and management of renewable resources and battery energy storage within RECs.

In conclusion, this thesis presents an investigation into the adaptation of power systems for a future increasingly reliant on RES. It navigates through the high-level challenges of reduced overall inertia on the transmission side as well as the emerging developments at the distribution level concerning RECs. This dual approach contributes significantly to our broader understanding and practical implementation of sustainable, stable power systems in an era progressively dominated by renewable energies.

1.1 Inertial Response and Synthetic Inertia

The frequency f of a power system constantly fluctuates, reflecting the ongoing balance between power consumption and generation. When this balance is momentarily disrupted, system frequency changes as kinetic energy is either absorbed or released by the rotating masses within the system. The system's frequency response to disturbances, such as disconnections in load or production, depends on the magnitude of the disturbance, the system's inertia, and on the frequency controls responses. Inertia plays a key role in buffering the system against abrupt frequency changes that can lead to stability problems. Traditionally, the primary source of inertia in power systems has been the rotating masses in synchronous generators. However, as the power system incorporates more non-synchronous sources like wind and solar power, the overall inertia decreases [5].

Modern wind turbine generators and other non-synchronously connected production units are linked to the system through power converters, isolating their rotational speed from the system frequency. Consequently, they don't naturally contribute to the system's inertial response. Synthetic Inertia (SI) refers to the provision of additional electrical power that mimics the kinetic energy release of a rotating mass, delivering an electrical torque in proportion to the Rate of Change of Frequency (RoCoF), thus helping to stabilize frequency fluctuations. This concept is sometimes referred to as synthetic inertial response [6].

Wind turbines, however, have been identified as a potential source of frequency support, including the provision of SI, to counteract large frequency deviations following disturbances. SI requires energy storage in systems connected through power electronics, like batteries, wind turbine rotating masses, or other power systems linked via high voltage DC (HVDC) connections. Controlling these sources to supply synthetic inertia is complex, as their power output is not directly related to the system frequency. Significant research has been directed toward developing controllers for wind turbines to respond to frequency disturbances. This thesis focuses on the immediate response of power systems after a disturbance, using metrics like minimum instantaneous frequency and RoCoF.

In equation (1.1), the RoCoF, expressed in Hz/s, is defined in relation to the per-unit power imbalance (ΔP), the nominal frequency of the network (f_n), and the aggregated system inertia (H_{sys}). The system inertia is the weighted sum of the inertia constants of each SG, where the weights correspond to their respective power rating.

$$RoCoF = \frac{df}{dt} = \frac{\Delta P f_n}{2H_{sys}} \tag{1.1}$$

This formulation underscores the inverse relationship between the RoCoF and the system’s inertia. It illustrates that a decrease in the overall system inertia leads to an increase in the RoCoF, emphasizing the direct impact that the system's inertia has on its frequency stability.

The frequency response of a power system to a significant disturbance is categorized into distinct control phases characterized by different time scales: Inertial Response (IR), Primary Frequency Response (PFR) and secondary frequency response also known as Automatic Generation Control or AGC, as depicted in Figure 1. Right after a disturbance, the inertia of the synchronous machines within the system acts as the first line of defense, curbing frequency deviations even before the intervention of governors, Automatic Voltage Regulators (AVR) and Power System Stabilizers (PSS). This initial phase, lasting up to 10 seconds, is generally referred to as IR and it is the natural response of the system. Following IR, PFR comes into play with the goal of stabilizing the frequency at a new equilibrium point and halting any further frequency deviation. In Synchronous Generators (SGs), governors are instrumental in this phase, adjusting the output power in relation to the frequency deviation and sharing the load among multiple generators proportionally to their rated power (droop speed control). Then AGC, acting on a broader area, occurs within a few minutes, aiming to bring the network frequency back to its nominal value. Finally, upon the completion of AGC, the tertiary frequency control phase replenishes the power reserves of the generators used during AGC, preparing them for any impending disturbance.

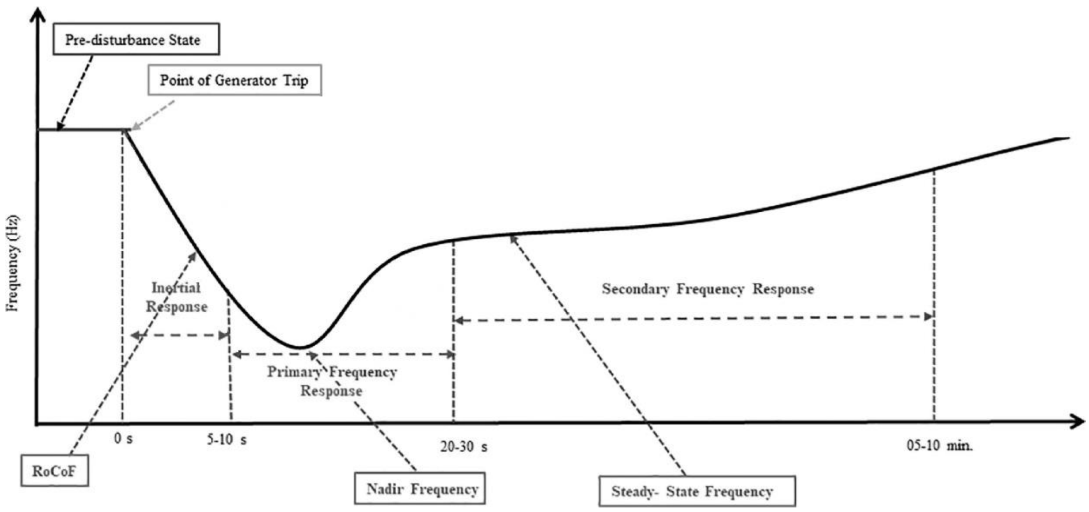

Figure 1. Schematic diagram of comprehensive frequency control (Adapted from [7]).

The swing equation is the fundamental equation governing rotor dynamics in SGs. It is derived by applying Newton's law to the rotating masses of the SGs and relates the power balance to the rotor's acceleration [8].

$$M_m \frac{d^2\delta_m}{dt^2} = P_m - P_e - D_m \frac{d\delta_m}{dt} \tag{1.2}$$

Where δ_m is the angular position in mechanical radians of the rotor, $M_m = J\omega_{sm}$ is the angular momentum of the rotor at its synchronous speed $(kg \cdot m^2 \cdot s^{-1})$, P_m and P_e are the input mechanical power and the output electrical power respectively (W), and the last term is the damping power, given by the product of the damping coefficient D_m $(N \cdot m)$ and the speed deviation accounting for the mechanical rotational losses due to windage and friction.

It is common practice in power systems to express M_m in terms of the generator's power rating S_n through a normalized constant of inertia H, measured in seconds. That is,

$$H = \frac{1}{2}\frac{J\omega_{sm}^2}{S_n} \tag{1.3}$$

Which represents the kinetic energy stored at synchronous speed, expressed in MJ, divided by the power rating S_n of the SG, measured in MVA. This way all generators of a given type will have a similar inertia constant regardless of their rating.

Summarizing, IR refers to the ability of SGs, by providing a reserve of kinetic energy, to resist to sudden changes in system frequency, directly related to their rotational speed. Inertia in power systems helps to stabilize the system following a disturbance by reducing the RoCoF.

SI is a concept introduced to address the challenges associated with the integration of RES, such as wind and solar, which may not inherently contribute to the overall system inertia. Since these sources often lack the rotating masses that traditional synchronous generators have, or these masses are asynchronously connected to the grid, SI involves using control strategies to emulate the effects of mechanical inertia.

Therefore, SI can be defined as the controlled contribution of electrical power from a unit that is proportional to the RoCoF at its terminals. One common method for implementing SI is through power electronic converters. By adjusting the control of these converters, it is possible to mimic the inertial response of SGs. The additional power injection or absorption by these devices helps stabilize the system during frequency deviations.

A simple expression for synthetic inertia control can be represented in $p.u.$ as follows:

$$\Delta P_e = -H_{SI}\frac{d\omega_s}{dt}\omega_s \cong -H_{SI}\frac{d\omega_s}{dt} \tag{1.3}$$

Where ΔP_e is the variation in electrical power of the unit, ω_s is the frequency at its terminals, approximately 1 in p.u., and H_{SI} it is the SI contribution of the unit. The term H_{SI} is none other than the relation between RoCoF and electrical power output variation in the control scheme of the unit, it depends on the specific implementation, and it usually contains some gains. In this way, SI control contributes to stabilizing the power system by providing additional power proportional to the rate of change of frequency. Specific implementations involve complex control algorithms and models.

1.2 Renewable Energy Communities

Since 2011, the European Union (EU) has been dedicated to achieving complete decarbonization of its energy system by 2050. Intermediate objectives aim for a 32% contribution from Renewable Energy Sources (RESs) to final energy consumption, a reduction in greenhouse gas emissions of up to 40%, and a 32.5% increase in energy efficiency by 2030, relative to the 1990 baseline [9]. Meeting these goals presents both challenges and opportunities in innovating energy supply systems, positioning European consumers at the forefront of the energy transition.

In this regard, in 2016, the European Commission introduced the Clean Energy for all Europeans Package (CEP). This package consists of directives aimed at revamping the EU energy sector through measures focusing on energy efficiency, renewable energy, electricity market restructuring, electricity supply security, and governance rules. Notably, two laws within this package formally recognize the rights of individuals and communities to actively participate in the energy sector. These are the Renewable Energy Directive (RED II), effective from December 2018 [10], and the Internal Electricity Market Directive (IEMD), launched in June 2019. RED II promotes renewable-based distributed systems, allowing neighbors connected by micro-grids to share electricity generated from RESs, creating Renewable Energy Communities (RECs). In contrast, IEMD introduces Citizen Energy Communities (CECs), where shared energy can originate from both RESs and fossil fuels, and participants can be geographically dispersed. The primary distinction between RECs and CECs lies in their energy sources and participant proximity, but both share the goals of legalizing energy sharing among European citizens and establishing them as central players in the energy market. All EU Member States were mandated to incorporate RED II and IEMD into their national laws by the end of 2021. However, various factors, including the pandemic, have led to delays in this process. The way these directives are transposed into national laws significantly impacts the optimal management of energy communities, adding another layer of complexity to this issue.

According to Italian regulation, "a REC is a group of citizens, small and medium-sized enterprises, territorial bodies, and local authorities, […], that share renewable electrical energy produced by facilities available to one or more members associated with the community. In a REC, renewable electrical energy can be shared among the various producers and consumers, located within the same geographic perimeter, thanks to the use of the national electric distribution network, which enables the virtual sharing of such energy" [11].

The main objective of a REC is to provide environmental, economic, and social benefits to its members or associates and to the local areas in which it operates, through the self-consumption of renewable energy. Moreover, RECs are a tool capable of significantly contributing to the spread of renewable energy installations, reducing greenhouse gas emissions, and achieving energy independence for the country.

The concept of RECs has gained considerable attention in recent years. The benefits of renewable energy sharing among diverse users have been recognized in scientific literature even before the formal establishment of RECs [12]. In rural areas, remote locations, and islands, decentralized RES-based electricity production and sharing have long been the norm for cost-effective electricity access [13].

RECs serve as a potential solution to increase the flexibility of the power grid. They do this by coordinating distributed generation and storage technologies through the use of measurements, forecasts, and information and communication technology. The economic rationale for establishing an energy community lies in the anticipated remuneration schemes. Nonetheless, there may be a notable disparity between the energy price offered by external suppliers and that which the community sells back to the grid. Therefore, the collective organization of prosumers in such schemes is deemed advantageous. Investigating the most beneficial solutions for these communities is critical, both in the planning stage and in operational management. To manage the energy consumption, production, and storage of these communities effectively, the implementation of an Energy Management System (EMS) is essential.

The implementation of a successful REC hinges significantly on establishing an effective automatic EMS. The primary objective in efficiently scheduling the controllable resources within an energy community is to minimize the collective energy procurement costs for the community members over a daily timeframe, as evidenced by studies such as [14] and [15]. In the realm of distributed approaches, the exchange of information among prosumers is deliberately limited so to reduce complexity. To tackle uncertainties inherent in load forecasts, several strategies come into play. Stochastic approaches [16] and adjustments made within the day-to-day scheduling based on updated information [17] are commonly employed.

Moreover, to address the challenges posed by uncertainties, robust optimization techniques are suggested [18]. Additionally, a three-stage scheduling framework is proposed, encompassing day-ahead, intra-day, and real-time stages [19], see Figure 2. This multi-stage approach proves effective in handling uncertainties in a comprehensive manner. However, when it comes to short-term load forecasting, especially for RECs with their relatively small size and high randomness, the task becomes intricate, as highlighted in [20], particularly when dealing with microgrids.

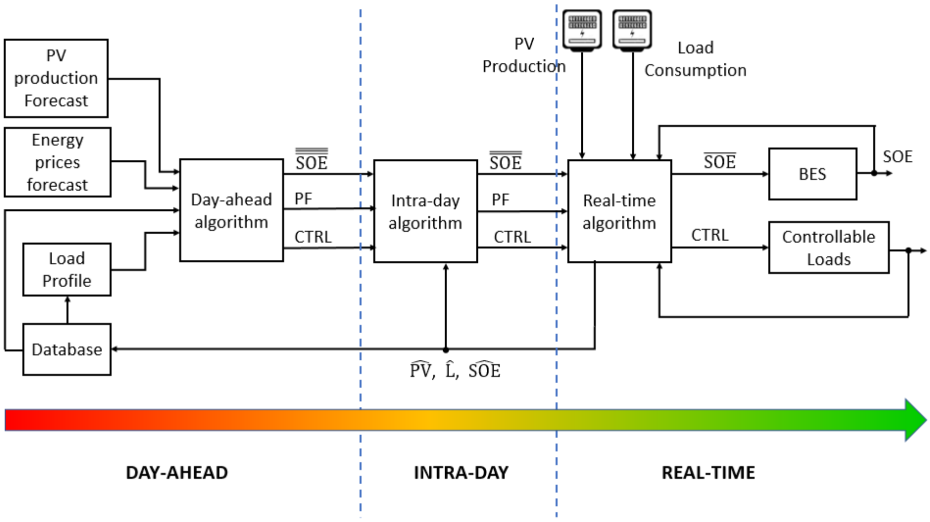

Figure 2. Three-stage scheduling framework depicting the typical decision-making process of an EMS and their time scale.

Various forecasting methods, including stochastic models and sophisticated techniques like artificial neural networks [21], are considered. While these approaches contribute significantly to load forecasting accuracy, it's essential to acknowledge that they often come with a computational burden that may not align with the real-time scheduling requirements. Striking a balance between the complexity of forecasting methods and the real-time constraints of scheduling systems becomes a crucial consideration in the pursuit of effective energy community management.

Chapter 2. Small-Perturbation Angular Stability

The stability of power systems has been, and remains, a central issue in the operation of large transmission networks. Due to an increasing number of interconnections between distinct areas and the installation of new generation plants, modern power systems have reached remarkable levels of complexity. Additionally, the combination of a growing demand for electric energy, the tendency to install larger generators with smaller inertia constants [8], and the rise of renewable energy production is pushing power systems to operate closer to their stability limits. Environmental constraints and high investment costs in new transmission lines make over-sizing the system practically impossible. Moreover, the operators' interest in optimizing management costs further contributes to the stability problem by reducing safety margins. These factors, coupled with the fact that even short service interruptions cause significant economic losses and inconvenience to millions of users, necessitate the development of increasingly efficient methods to assess the stability of vast and complex power networks.

By their nature, power systems can experience two types of disturbances that alter their operational state: contingent disturbances or load variations. Contingent disturbances include the loss of generators or parts of the transmission network (transformers, lines, substations) due to short circuits, which can be caused by a variety of weather events and/or technical failures and typically lead to a change in the network topology due to the activation of protections. Load variations, on the other hand, do not alter the structure of the network and are equivalent to changes in power demand at nodes and/or power exchanges between nodes. Power systems are designed and built to withstand disturbances of reasonable magnitude. Larger disturbances can result in unacceptable operational states and in frequency, voltage, or rotor speed variations outside permitted limits [22].

In particular, the problem of angular instability in power systems limits the power transferable in networks, especially when transmission distances are long. Small-perturbation angular stability relates to the assessment of the dynamic of the generators in response to small variations in load demand and generation, that occurs continuously on the power systems and not necessarily related to a transient disturbance. This kind of instability can be related to the lack of either synchronizing torque or damping torque. Currently, this instability mostly concerns the insufficient damping of the systems oscillations, related to large groups of closely coupled machines connected by weak tie lines [23].

In the context of small-signal stability of electrical power systems, modal analysis refers to the study of the system's dynamic response to small disturbances. It does so by focusing on the linearized behavior of the power system around its operating point, considering small deviations from the steady-state conditions. Modal analysis helps identify the system's electromechanical modes and assess their stability. Moreover, the modal behavior of a system is independent on the type of perturbation but is an intrinsic property of the power system under exam. The procedure is as follows:

- **Linearization**: The power system equations are linearized around the operating point, assuming that the disturbances are small. This results in a linearized state-space representation of the system.
- **Eigenvalue Analysis**: The linearized system is then analyzed to find its eigenvalues. The eigenvalues represent the natural frequencies and damping ratios of the system's electromechanical modes. Each mode corresponds to a specific oscillatory behavior.
- **Mode Shape Analysis**: The associated eigenvectors are examined to understand the mode shapes. Mode shapes provide insights into how different components of the power system contribute to each mode's behavior.
- **Damping Ratio Assessment**: The damping ratio of each mode is crucial for assessing stability. Modes with damping ratios above 5% are typically considered sufficiently stable. If a mode has a low damping ratio, it indicates poor stability and may require additional control measures.
- **Control System Design**: Modal analysis helps engineers design control systems, such as Power System Stabilizers (PSS), to improve the damping of critical modes and enhance the overall small signal stability of the power system.

By performing modal analysis, power system engineers can gain a deeper understanding of the system's natural dynamic response to small disturbances and make informed decisions to enhance grid stability and reliability.

In formulas, a dynamic system described by state matrix $\boldsymbol{A}$ is said to be stable to small angle perturbations if all eigenvalues $\lambda = \sigma + j\omega$ have negative real part. In general, a nonlinear system can be described by a set of differential equations

$$\dot{\boldsymbol{x}} = \boldsymbol{F}(\boldsymbol{x}) \tag{2.1}$$

where $\boldsymbol{x}$ represents the vector of n state variables. The system is stable in the equilibrium points $\hat{\boldsymbol{x}}$, that is $\boldsymbol{F}(\hat{\boldsymbol{x}}) = 0$, and the value of the state variables does not change over time. Expanding $\boldsymbol{F}(\boldsymbol{x})$ in a Taylor series near $\hat{\boldsymbol{x}}$, and neglecting the terms of higher order than the first, allows obtaining the linear approximation of the system in the form

$$\Delta\dot{\boldsymbol{x}} = \boldsymbol{A}\,\Delta\boldsymbol{x} \tag{2.2}$$

where $\Delta\boldsymbol{x} = \boldsymbol{x} - \hat{\boldsymbol{x}}$ is the state variables variation from equilibrium, and $\boldsymbol{A} = \partial\boldsymbol{F}/\partial\boldsymbol{x}$ is the Jacobian matrix calculated at the point $\hat{\boldsymbol{x}}$. The diagonalization of the real square matrix $\boldsymbol{A}$ into its eigenvalues yields to a straightforward solution by decoupling the system of differential equations, similar to that the scalar equation:

$$\boldsymbol{x}(t) = e^{\boldsymbol{A}t}\boldsymbol{x}_0 \tag{2.3}$$

Once again, the system is said to be stable if and only if all the eigenvalues of state matrix $\boldsymbol{A}$ have a negative real part. Damping refers to pairs of complex eigenvalues $\lambda = \sigma \pm j\omega$, which introduce oscillatory modes with frequency equal to $f = \frac{\omega}{2\pi}$, and it is a measure of the rate of decay of the amplitude of the oscillations. To quantify this, the damping ratio is introduced:

$$\zeta = -\frac{\Re e\{\lambda\}}{|\lambda|} = -\frac{\sigma}{\sqrt{\sigma^2 + \omega^2}} \tag{2.4}$$

which corresponds to the opposite of the real part of the eigenvalue divided by its module. The damping ratio, if the mode is stable, is a number included between 0 and 1. If the eigenvalue is purely real ($\lambda = \sigma$) and the real part is negative, then $\zeta = 1$ and the response is a decreasing exponential, thus stable. If the eigenvalue is purely imaginary ($\lambda = \omega$), then $\zeta = 0$ and the response corresponds to an undamped oscillation that persists indefinitely. The damping coefficient thus expresses the amount of damping present in the mode's response, or how much the amplitudes of the oscillations decrease from period to period. After 5 oscillation periods, with $\zeta = 0.1$, the amplitude of the oscillations decreases by 96%, with $\zeta = 0.05$, the amplitude decreases by 79%. In the practice of electric power systems, a system is said to be stable, and oscillations properly damped, if for every mode $\zeta \geq 0.05$ (i.e., if the damping ratio is greater than 5%). In some cases, to be more conservative, a value of 10% is used, but usually 5% is the considered threshold of stability.

An important role in power system small perturbation angle stability analysis is played by the right eigenvectors of state matrix $\boldsymbol{A}$, which allow for its diagonalization by converting the state variables into modal variables. That is,

$$\boldsymbol{x} = \boldsymbol{Wz} \tag{2.5}$$

where $\boldsymbol{W}$ is the matrix of the right eigenvectors. If the eigenvectors are normalized, then the i^{th} element of right eigenvector k, that is $w_k(i)$, determines the share of modal variable $z_k(t)$ in the activity of state variable $x_i(t)$. This is usually referred to as observability or mode shape, which describe the response of the system at each natural frequency. The mode shapes are important because represent an inherent feature of a linear dynamic system and do not depend on where and how a disturbance is applied. Regarding electromechanical modes (i.e., modes involving swings of rotors generators), the generator speed mode shape is the key factor for determining the influence of individual oscillatory modes on swings of the rotors of individual generators.

Other important coefficients are the participation factors, obtained multiplying element by element left and right eigenvectors related to the same mode. Participation factors are a good measure of correlation between modes and state variables; they are typically used to determine the siting of stability enhancing devices. Generally, a stabilizer is preferably installed where the modal variables associated with a given eigenvalue are both well observable and controllable (i.e., the magnitude of the participation factor is large). Electromechanical modes can be identified as those modes in which rotor angle deviation and rotor speed deviation have a large participation factor. These types of modes will be the primary focus of this report. However, only the magnitude of the participation factor carries relevant information. For this reason, it is useful to define the *oscillation vector* which is composed by the magnitude of the participation vector and the angle of the observability [24]. Plotting the oscillation vectors allows identifying the state variables mainly involved in that mode and, by looking at the angle differences, understand how the oscillations are manifested in the state variables, e.g., if in phase or counter-phase. In formulas, the oscillation vector of state variable x_i with respect to mode k is:

$$ov_{ki} = |pf_{ki}|\angle w_k(i) \tag{2.6}$$

where pf_{ki} is the participation factor of state variable x_i in the k^{th} mode and w_k(i) is the i^{th} element of observability vector k (i.e., the right eigenvector associated to mode k). This feature will be used to identify the properties specific to each relevant oscillation mode, in particular electromechanical modes, and the behaviour of the involved generators.

As an example, in Figure 3 the oscillation vector of the inter-area mode of the well-known “two-areas four-generators” system by Kundur is shown [23]. The interpretation of this oscillation vector is that, if a disturbance excites this mode, the rotor speeds of generators 3 and 4 will swing, coherently to each other, in counterphase with respect to those of generators 1 and 2, which in turn will swing coherently. Since the two pairs of generators belong to two different areas, this allows inferring that the considered mode is an interarea mode, characteristic which is also confirmed by its low frequency. Furthermore, by looking at the magnitude of the oscillation vectors, that is the participation factor, we can understand that the oscillations of generators 3 and 4 will be significantly more severe than those of generators 1 and 2.

Electromechanical modes can be generally classified in three categories depending on the location of the generators involved. In order of increasing frequency, interarea modes involve generator belonging to distinctly different areas of the grid (e.g., Sicily and the peninsula), inter-plant or local modes are modes involving units of the same area but different plant, intra-plant modes are modes involving units of the same plant. Throughout the report, modes presenting the same dynamic phenomenon, hence with a very similar oscillation vector, will be referred to using the same denomination. As an example, the interarea mode involving generators in Sicily and the generator slack in the peninsula, identified by its oscillation vector, will be referred to, for the relevant dispatching profiles, as M1.

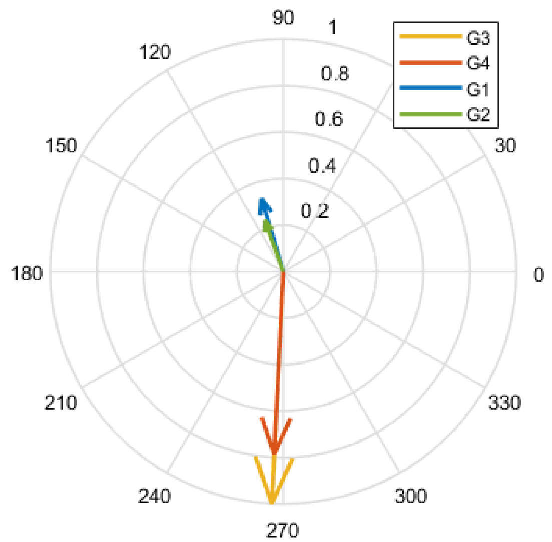

Figure 3. Oscillation vector of the interarea mode of the “2-areas 4-generators” benchmark test network [23].

Chapter 3. Wind Turbines Synthetic Inertia Control Schemes

In this chapter the electromechanical model used to describe variable speed wind turbines is described. This includes the mechanical and aerodynamic model as well as the control schemes of the back-to-back convert that connects the generator of the wind turbine to the grid.

The second part of the chapter expands upon the control logics and the energy reserves that allow wind turbines and thus wind power plants to emulate both the inertial response and the primary frequency regulation of conventional synchronous generators. This includes the use of supercapacitor to store energy in the DC-link of the back-to-back converter, deloading techniques to allow the wind turbine to produce more power when needed and the installation and control of battery energy storage system that can be installed in various possible locations within the wind farm.

3.1 Modelling of Wind Turbines

A basic scheme of wind turbine equipped with a Doubly-Fed Induction Generator (DFIG) is reported in Figure 4. At the mechanical level the model of a wind turbine includes the aerodynamic model and the pitch angle control model, at the electrical level it includes the model of the generator and the model of the back-to-back converter. This encompasses the Rotor-Side convert (RSC) and the Grid-Side Converter (GSC) and their respective control schemes.

The specific type of wind turbine only influences the model the generator and its control strategy when interconnected with the power grid. Wind farms (WFs) are often characterized by fully aggregated models representing multiple WT units, as outlined in [25], [26]. The subsequent section provides a detailed description of a wind turbine equipped with a DFIG.

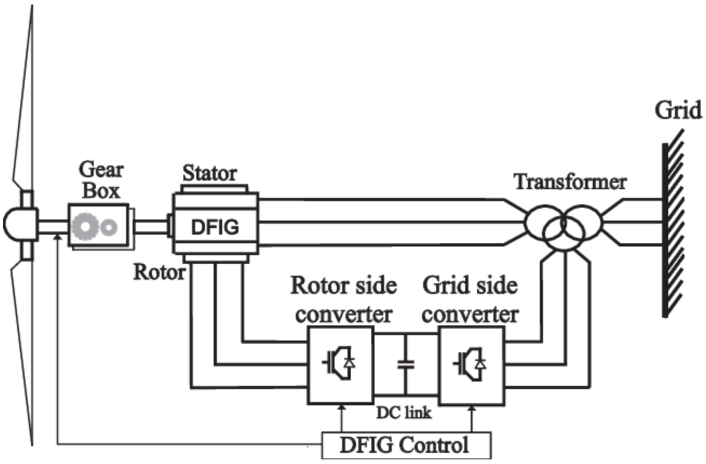

Figure 4. Basic configuration of a DFIG WT (Adapted from [27]).

3.1.1 Wind turbine model

The drive train of the wind turbine is modelled by a two-mass model as depicted in Figure 5. A large mass with inertia J_T represents the rotor of the turbine and a lighter mass with inertia J_G represents the rotor of the generator. The shaft connecting the rotors is modelled by a stiffness coefficient K_{sh} and a damping coefficient D_{sh}.

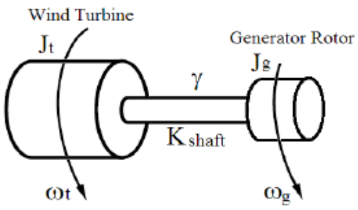

Figure 5. Two-mass system model of the drive train (Adapted from [27]).

The equations governing the model are the following:

$$
\begin{gathered}
T_W - T_{sh} = J_T \dot{\omega}_t \\
T_{sh} - T_G = J_G \dot{\omega}_r \\
\dot{\vartheta} = \omega_t - \omega_r \\
T_{sh} = \vartheta K_{sh} - \dot{\vartheta} D_{sh}
\end{gathered}
\tag{3.1}
$$

Where T_W is the torque applied by the wind, T_{sh} is the torque of the shaft and T_G is the torque applied by the electrical generator. The angular difference between the ends of the shaft is denoted by ϑ and its time variation depends on the difference between the rotational speed of the turbine and that of the generator's rotor, denoted respectively by ω_t and ω_r. The mechanical power P_W extracted by the wind and the mechanical power of the generator P_G are related to T_W and T_G by equations

$$P_W = T_W \omega_t$$
$$P_G = T_G \omega_r \tag{3.2}$$

Furthermore P_W can be expressed as a function of the wind speed v_W and the speed of rotation of the turbine via the power coefficient C_p and the tip speed ratio $TSR = \omega_t R / v_W$

$$P_W = \frac{1}{2} \rho A \cdot Cp(TSR, \beta) \cdot {v_W}^3 \tag{3.3}$$

where ρ is the air density, $A = \pi R^2$ is the surface area swept by the blades and the power coefficient is a function of the TSR and the pitch angle of the blades, denoted by β [28].

3.1.2 Pitch angle control

The power coefficient C_p has a maximum theoretical value, known as Betz's limit, equal to $C_{p\,max} = 16/27 \cong 0.59$, and represents the maximum power that can be extracted from the wind. Modern, sizable wind turbines attain maximum values for the power coefficient within the range of 0.45 to 0.50, constituting approximately 75–85% of the theoretically achievable limit [29]. In instances of high wind speeds, with the turbine operating at its rated power, the pitch angle control adjusts the angle of attack of the blades, increasing drag and reducing lift, so to reduce Cp, safeguarding itself from potential damage. With the wind speed doubling from 12.5 to 25 m/s, wind power increases by a factor of 8. Consequently, Cp must decrease proportionally, reaching values as low as 0.06 in winds of 25 m/s. In particular, as shown in Figure 8, the pitch angle control system is designed to prevent the wind turbine rotor from over-speeding under normal operating conditions and during grid faults. The controller takes as input the difference between the measured generator speed and the maximum allowable generator speed. Below the maximum speed of the generator, the output of the PI controller remains zero. However, in the event of over-speeding, such as when the generator speed exceeds the maximum limit due to excess wind power or faults, the PI controller output increases to decelerate the generator back towards the specified limit. The first-order actuator in the system models the physical process of adjusting the pitch angle β to its reference value, with constraints imposed on both the value of the pitch angle and its rate of change.

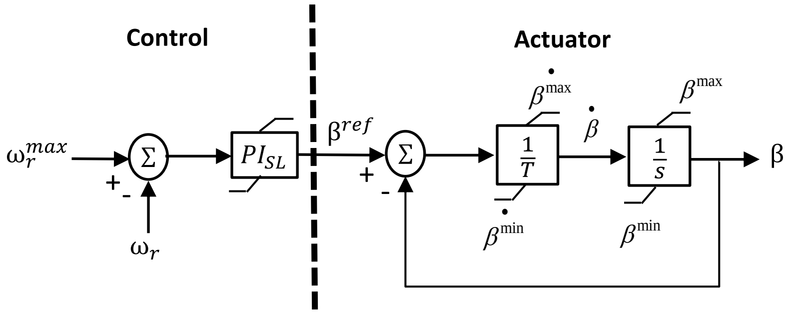

Figure 6. Pitch control and actuator model.

3.1.3 Rotor-side converter control architecture

The Rotor-Side Converter (RSC) control architecture comprises d-axis and q-axis channels, both employing typical PI controllers. In the center of Figure 7 only the d-axis current control is shown as the q-axis channel follows a similar logic. The deloading scheme, highlighted in red, is followed by the pitch angle control and it will be discussed together with the Rotor Kinetic Control (RKC) scheme, highlighted in blue, in the next section.

The d-axis channel, featuring three PI control loops in cascade, governs the generator's active power P_{WT}. The process is as follows: following the Maximum Power Point Tracking (MPPT) curve, which automatically positions the wind generator at the point of highest efficiency, the rotor speed reference for maximum power extraction is determined by a predefined power-speed MPPT characteristics. In this context, we assume a quadratic relationship between the reference speed generated by the MPPT controller and the wind turbine output power. The first PI controller operates on the disparity between the measured rotor speed and the reference speed from the MPPT controller, establishing the active power reference for the RSC. The second PI controller manages the WT's output active power concerning the reference from the speed controller. It generates the d-axis reference rotor current for the rapid inner current PI control loop, governing the d-axis current component to define the modulation index for the converter.

The q-axis channel, comprising two cascaded PI control loops, oversees the generator stator reactive power. Here's how it functions: the first PI controller regulates the WT's output reactive power to a designated reference, producing the q-axis reference rotor current for the swift inner current PI control loop. This inner loop manages the q-axis current component to define the modulation index for the converter.

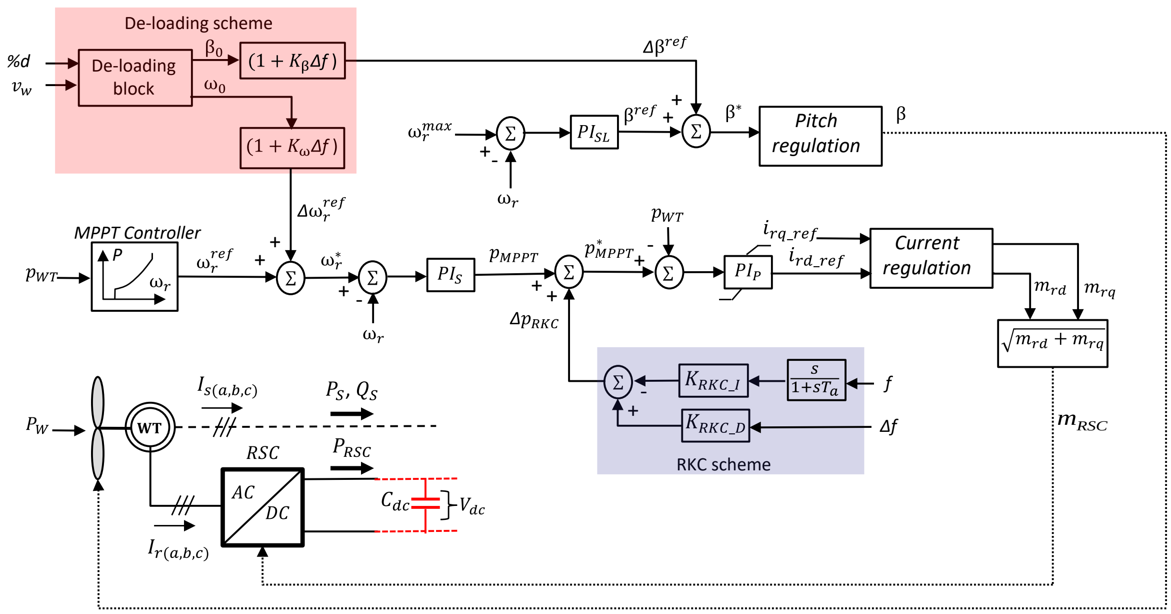

Figure 7. Schematic diagram of the RSC control architecture implementing RKC IR and the deloading scheme providing PFR.

3.1.4 Grid-side converter control architecture

Similarly to the rotor-side converter control, the Grid-Side Converter (GSC) control system incorporates d-axis and q-axis channels, both employing PI controllers, as depicted in Figure 8. The d-axis channel (on top), featuring two cascaded PI control loops, operates as follows: the initial PI controller oversees the voltage of the DC-link, maintaining it at a specified reference value irrespective of the power flow magnitude and direction coming from the RSC. It generates the d-axis reference rotor current for the swift inner current PI control loop, regulating the d-axis current component to determine the modulation index for the converter.

The q-axis channel, not shown in the figure, involves only one PI control loop, which regulates the q-axis reference rotor current to a zero reference (unitary power factor). This adjustment defines the q-axis modulation index for the converter. Consequently, the GSC's reactive power flow is set to zero, reducing the GSC rating.

In Figure 8, the control loops that allow to emulate the inertial response accessing the energy in the DC-link of the back-to-back converter are both shown. All control signals are expressed in per unit. A Phase-Locked Loop (PLL) measures the network frequency which is fed into a first-order low-passing filter with time constant $T_f = 0.1\ s$. The Voltage Control Mode (VCM), highlighted in green, compares it to the nominal frequency f_0 and through the gain K_{in_V} acts upon the DC-link voltage v_{dc_ref} through a voltage variation Δv_{dc_ref}. The Current Control Mode (CCM), highlighted in red, takes the network frequency as input and calculates its derivative, known as RoCoF, and through the gain K_{in_I} acts upon the direct current reference i_{cd_ref}, generated by the voltage controller, thus regulating the active power injected into the grid. In the next section these concepts will be expanded upon.

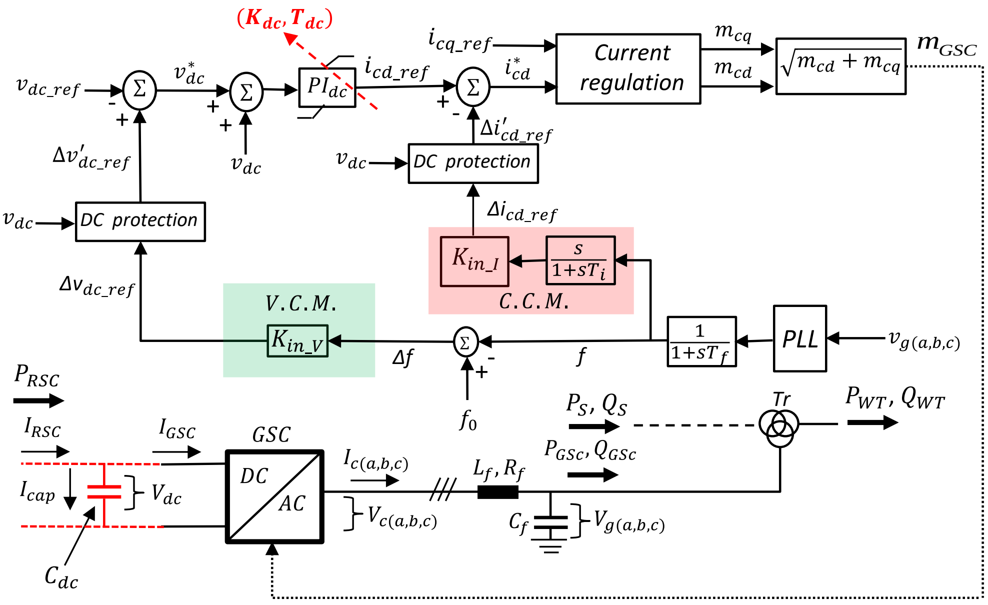

Figure 8. Schematic diagram of GSC control architecture for DC-link SI.

3.1.5 *Power converter model*

Given the emphasis of this study on power system stability, switching frequencies and high frequencies phenomena are not considered, and the system response is investigated solely in the vicinity of the nominal frequency. For this reason, the model of the converters is based on a fundamental frequency model, operating within a stator voltage-oriented reference frame. In the context of the sinusoidal Pulse Width Modulation (PWM) technique with a modulation index $|m| < 1$, the relationship between the line-to-line RMS AC voltage U_{AC} and DC voltage U_{DC} is expressed as:

$$U_{AC} = \frac{1}{2}\sqrt{\frac{3}{2}}\, m\, U_{DC} \tag{3.4}$$

where $m = \sqrt{m_d + m_q}$ with m_d and m_q being respectively the d-axis and q-axis components of the modulation index. The DIgSILENT PWM-converter model takes m_d and m_q as inputs, with the former governing the converter's active power output and the latter controlling the reactive power output. For $|m|$ values exceeding 1, the converter enters saturation, accompanied by the emergence of low-order harmonics. The Space Vector Pulse Width Modulation Technique (SVPWM) allows to increase m up to the value of 1.15.

3.2 Frequency Support Schemes

Variable-speed wind turbines (VSWTs) can emulate both the Inertial Response (IR) and Power-Frequency Response (PFR) characteristics of traditional synchronous generators through the implementation of suitable control strategies and energy reserves. For the short-term power demanded by IR, additional controllers must be integrated into the converters of VSWTs to manage the Electrical Energy (EE) stored in the DC-link capacitors or the Kinetic Energy (KE) of their rotors. The rotor kinetic energy control (RKC) method is one such approach.

To actively contribute to PFR, VSWTs need to possess adequate power margin for consistent power exchange. Achieving this typically involves either operating the wind turbines below the MPP conditions, a strategy referred to as deloading, or foresee the use of external Energy Storage Systems (ESS), such as Battery Energy Storage Systems (BESS) installed either at the wind turbine level or at the wind farm level, as it will be discussed.

3.2.1 DC-link and grid-side converter synthetic inertial control scheme

DC-link capacitors find application in nearly all grid-connected power converters, serving purposes such as DC-link voltage support, voltage ripple filtering, and reactive power compensation [30], [31]. In wind turbines their use is crucial for maintaining power balance between the rotor-side Converter and the grid-side converter as any power imbalance leads to a change in the DC voltage. Despite their limited capacitance, the electrostatic energy stored in these capacitors can be utilized for SI through the grid-side converter control architecture introduced in section 3.1.4. As shown in Figure 8, two control schemes to implement DC-link SI are possible, the Current-Controlled Mode (CCM), in red, and the Voltage-Controlled Mode (VCM), in green. Although these two methods are presented simultaneously in the control scheme, they are mutually exclusive and either one or the other will be implemented. These methods are not limited only to wind turbines but can be applied to any grid-interfaced back-to-back converter and involves adjusting the dc-link voltage V_{dc} in response to frequency variations.

A. *Current-controlled mode*

Highlighted in light red in Figure 8, the CCM approach establishes a derivative relationship between the injected power, accessed via the direct current reference i_{cd_ref}, and the measured network frequency f. This control scheme calculates the RoCoF from the grid voltages and multiplies it by a constant gain K_{in_I} yielding the variation of the direct current reference Δi_{cd_ref} which in turn regulates the active power injected into the grid [32], [33]. To filter out noise from the derivative signal and prevent abrupt changes, an additional first-order low-pass filter with a time constant T_i is applied.

Subtracting this signal variation to the direct current reference allows active power injection during under-frequency events, capitalizing on the discharge of the DC capacitors and vice versa. Achieving SI through this method requires the dynamics of the DC-link voltage controller to be deliberately slow. This slowness allows the stored electrostatic energy to be released or absorbed before the voltage controller reacts, restoring the DC voltage to its nominal value.

The active power contribution to the SI from the DC-link capacitors using the CCM architecture can be expressed as follows:

$$\Delta p_{DC} = \frac{2H_{DC}}{(1+sT_f)(1+sT_i)}\frac{df}{dt} \tag{3.5}$$

By neglecting the filtering time constants T_f and T_i this expression can be approximated as:

$$\Delta p_{DC} = 2H_{DC}\frac{df}{dt} \tag{3.6}$$

Therefore, the relation between the inertia constant that the DC-link CCM SI emulation scheme is able to provide, and the related gain, is the following:

$$H_{DC} = \frac{K_{in\_I}}{2} \tag{3.7}$$

In practical applications, the maximum allowable DC voltage variation is determined by considerations on insulation levels and PWM constrains. It becomes evident that for significant frequency transients, even small values of the SI gain may fail to keep the DC voltage within acceptable limits. Thus, a protective mechanism needs to be implemented to safeguard the DC-link. This protection scheme ensures that the design of the SI gain is decoupled from the characteristics of the grid, maintaining the DC-link voltage within an acceptable range.

The logic of the DC voltage protection scheme is reported in Figure 9. This protection scheme takes the output of the CCM SI scheme and the measured DC voltage as inputs and activates the SI only when the charging or discharging process aligns with the measured DC voltage and its rating. Specifically, the discharging process is inhibited while the charging process is permitted when the DC voltage is lower than its lower bound v_{DC}^{min}. Conversely, the charging process is inhibited while the discharging process is allowed when the DC voltage exceeds its upper bound v_{DC}^{max}. Section 3.2.1.C provides a comprehensive discussion of the DC voltage limits necessary to design the DC protection logic, ensuring the optimal utilization of the available electrostatic energy reserve while adhering to technical and security constraints associated with the power electronic converters.

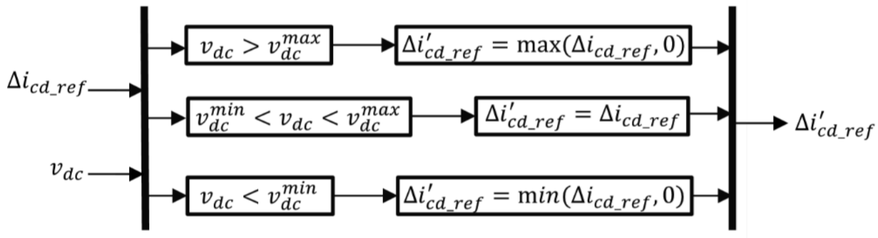

Figure 9. DC voltage protection logic in the current-controlled mode inertial response emulation scheme.

B. Voltage-controlled mode

Highlighted in light green in Figure 8, the VCM approach establishes a linear proportional relationship between the dc-link voltage reference and the measured network frequency deviation. Among others, this approach has been presented in [34]. In this scheme, a frequency controller with a constant gain K_{in_V} takes the frequency deviation signal Δf as input and outputs the DC voltage reference variation Δv_{dc_ref}. For the SI to be realized in this manner, the dynamics of the DC-link voltage controller are set to be quite fast. This design enables the prompt release or absorption of stored electrostatic energy in response to DC-link voltage deviations.

In the VCM architecture, the energy stored in the capacitor (or in the supercapacitors) to provide IR can be accessed via the grid-side converter by varying the DC-link voltage V_{DC}. Neglecting power losses in the converters, the power balance between the power injected into the rotor-side converter P_{RSC} and the power transmitted to the grid via the GSC P_{GSC} is reflected by the DC-link voltage. The power absorbed or released by the capacitor can be expressed in per-unit form as:

$$\Delta p_{DC} = p_{GSC} - p_{RSC} = c_{DC} v_{DC} \frac{dv_{DC}}{dt} \tag{3.8}$$

where:

$$c_{DC} = \frac{C_{DC} V_{DC0}^2}{S_{WT}} \tag{3.9}$$

with c_{DC} being the total DC-link capacitance in p.u., C_{DC} the capacitance in Farad and S_{WT} the rated power of the wind turbine. Moreover, v_{DC} is the dc-link voltage in per-unit form, V_{DC0} represents the nominal DC voltage in volts, p_{RSC} and p_{GSC} are the per-unit forms of P_{RSC} and P_{GSC} respectively, and Δp_{DC} is the per-unit power contribution from charging or discharging the capacitors.

To equate the WT GSC with an inertia constant (H_{DC}), the following relationship is derived by equating Δp_{DC} to the power variation associated with a frequency variation in a synchronous generator, that is:

$$c_{DC} v_{DC} \frac{dv_{DC}}{dt} = 2H_{DC} f \frac{df}{dt} \tag{3.10}$$

where H_{DC} can be thought as the equivalent SI constant provided by the electrostatic energy of the DC-link, Integrating both sides of this equation:

$$\int_{f_0}^{f} 2H_{DC} f df = \int_{v_{dc0}}^{v_{dc0}} C_{dc} v_{dc} dv_{dc} \tag{3.11}$$

yields to:

$$H_{DC}(f^2 - f_0^2) = \frac{1}{2} c_{DC} (v_{DC}^2 - v_{DC0}^2) \tag{3.12}$$

whit f_0 being the nominal frequency of the network. For small variations of the DC voltage, this equation can be linearized around its equilibrium point as:

$$2H_{DC} f_0 \Delta f = c_{DC} v_{DC0} \Delta v_{DC} \tag{3.13}$$

and since:

$$K_{in\_V} = \Delta v_{DC} / \Delta f \tag{3.14}$$

we obtain:

$$H_{DC} = K_{in\_V} \frac{c_{DC} v_{DC0}}{2f_0} \tag{3.15}$$

The implementation of the VCM DC protection scheme, depicted in Figure 10, follows a similar logic to the one related to the CCM in terms of maintaining the DC voltage within its rated values. This protection scheme takes the output of the SI control and the measured DC voltage as inputs, limiting the SI outputs to values compatible with the DC voltage ratings. Specifically, the IR output is limited to a value of $v_{DC0} - v_{DC}^{min}$ during the discharging process, and only charging is allowed when the dc voltage is lower than its lower bound. Conversely, the SI output is limited to a value of $v_{DC}^{max} - v_{DC0}$ during the charging process, and only discharging is allowed when the DC voltage exceeds its upper bound.

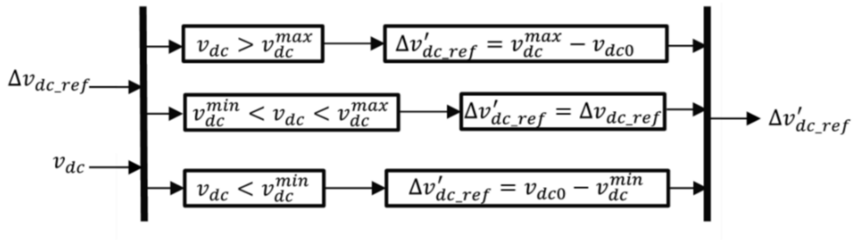

Figure 10. DC voltage protection logic in the voltage-controlled mode inertial response emulation scheme.

To ensure that both the VCM and the CCM SI control schemes work as intended, a crucial factor to consider is the parameters of the DC voltage controller, as mentioned. The parameters of the DC voltage PI controller are set to secure a slow response in the case of the CCM SI architecture, this allows to access the stored energy via the CCM before that the PI restores the DC voltage within its nominal values. Conversely, for the VCM SI architecture, the DC voltage PI controller parameters are configured to achieve a fast response so that any power demand is matched by a fast voltage variation. Taking these considerations into account, the values of the gain K_{DC} and of the time constant T_{DC} of the PI controller of Figure 8, whether the CCM or the VCM is used, are reported in Table 1.

Table 1. CCM and VCM parameters of the PI DC-link voltage control.

Parameter	CCM	VCM
K_{DC} $[s^{-1}]$	0.1	5
T_{DC} $[s]$	30	0.02

C. DC-link voltage limits and voltage controller

In the implementation of the DC-link scheme for SI, where the power released during a frequency disturbance is associated with the magnitude of the DC voltage variation, the operation of the GSC imposes constraints on the maximum range of DC-link voltage deviation. During over-frequency events, the capacitors are controlled to absorb energy by raising the voltage. The maximum permissible voltage, denoted as V_{DC}^{max}, is dictated by the voltage ratings of the active and passive components of the GSC unit. Conversely, for under-frequency events, the control is designed to release electrostatic energy by reducing the voltage. However, the minimum allowable DC-link voltage, denoted as V_{DC}^{min}, is restricted by PWM constraints.

In this section, a mathematical analysis is provided, addressing the estimation of the upper and lower bound of the DC-link voltage in both steady-state and transient conditions, along with a discussion of the factors influencing it. The correct evaluation of this range is essential for designing the DC-link protection schemes to properly implement the IR control schemes. In this specific case, the analysis is exemplified considering the GSC of a DFIG wind turbine. However, it is valid to any grid-interfaced converter source.

The GSC is interfaced with the grid through an inductive filter characterized by an inductance L_f and a resistance R_f. To streamline the control process, the *dq* transformation method is employed with a reference frame oriented along the vector of the voltage supply. This approach enables to control independently the active and reactive power flow between the supply and the GSC [35]. The voltage balance across the inductance expressed in the *dq*-frame is given by:

$$\begin{cases} V_{sd} = R_f I_{cd} + L_f \dfrac{di_{cd}}{dt} - \omega_{dq} L_f I_{cq} + V_{cd} \\ V_{sq} = R_f I_{cq} + L_f \dfrac{di_{cq}}{dt} - \omega_{dq} L_f I_{cd} + V_{cq} \end{cases} \tag{3.16}$$

where V_s is the grid voltage at the low voltage side of the transformer, V_c and I_c are the voltage and the current at the AC side of the GSC, subscripts d and q stand for the direct and quadrature component and ω_{dq} is the angular frequency of the grid. Expressing the complex power injected by the GSC into the grid using these quantities gives:

$$S_{GSC} = \frac{3}{2}\left[\left(V_{sd} I_{cd} + V_{sq} I_{cq}\right) + j\left(V_{sq} I_{cd} - V_{sd} I_{cq}\right)\right] \tag{3.17}$$

By orienting the *d*-axis of the reference frame along the grid voltage, the *q*-axis component will be null, therefore, the active and reactive power expressions simplify into:

$$\begin{cases} P_{GSC} = \dfrac{3}{2} V_s I_{cd} \\ Q_{GSC} = -\dfrac{3}{2} V_s I_{cq} \end{cases} \tag{3.18}$$

rearranging so to highlight the GSC currents leads to:

$$\begin{cases} I_{cd} = \frac{2}{3}\frac{P_{GSC}}{V_s} \\ I_{cq} = -\frac{2}{3}\frac{Q_{GSC}}{V_s} \end{cases} \tag{3.19}$$

substituting the currents into equation 3.16, rearranging and neglecting the voltage drop across R_f allows to express the GSC voltages in terms of the grid voltage and of the power output:

$$\begin{cases} V_{cd} = \frac{2}{3}\frac{L_f}{V_s}\left(-\frac{dP_{GSC}}{dt} - \omega_{dq}Q_{GSC}\right) + V_s \\ V_{cq} = \frac{2}{3}\frac{L_f}{V_s}\left(\frac{dQ_{GSC}}{dt} - \omega_{dq}P_{GSC}\right) \end{cases} \tag{3.20}$$

Considering the SVPWM technique the modulation index of the converter can reach values up to $m_{max} = 1.15$ and the following expression holds true [36]:

$$V_c = \frac{1}{2}\sqrt{\frac{3}{2}}mV_{DC} \tag{3.21}$$

Therefore, the lower bound for DC-link voltage necessary to provide adequate AC-side voltage is given by the maximum value of the modulation index as:

$$V_{DC}^{min} = 2\sqrt{\frac{2}{3}}\frac{V_c}{m_{max}} \tag{3.22}$$

since

$$V_c = \sqrt{\frac{3}{2}(V_{cd}^2 + V_{cq}^2)} \tag{3.23}$$

substituting 3.23 into 3.22, taking 3.20 into account, and neglecting terms of the second order yields:

$$V_{DC}^{min} \cong \frac{2}{m_{max}}\sqrt{V_s^2 - \frac{4}{3}L_f\left(\frac{dP_{GSC}}{dt} + \omega_{dq}Q_{GSC}\right)} \tag{3.24}$$

This equation allows to conclude that the lower bound of the DC-link voltage V_{DC} is set by the grid voltage, the modulation technique and especially by the amount of active and reactive power transferred to the grid. During steady state conditions the DC voltage is mainly limited by reactive power Q_{GSC} injection, while the active power contribution is negligible. During transient conditions, V_{DC}^{min} is more sensitive to active power injection rather than reactive power [37].

D. DC-link energy capacity and sizing

Having determined the maximum allowable range of excursion of the DC voltage, the accessible electrostatic energy in the DC-link can be calculated. The electrostatic energy stored in the DC-link is given by:

$$E_{DC} = \frac{1}{2} C_{DC} V_{DC0}^2 \tag{3.25}$$

in which V_{DC0} is the rated voltage and C_{DC} the capacitance of the link. Therefore, the available electrostatic energy for underfrequency IR support is given by:

$$E_{DC}^{use} = E_{DC}(1 - \frac{V_{DC\_min}^2}{V_{DC0}^2}) \tag{3.26}$$

or, in terms of the voltage variation:

$$E_{DC}^{use} = E_{DC}[1 - (1 - \frac{\Delta V_{DC}}{V_{DC0}})^2] \tag{3.27}$$

The accessible energy is, therefore, just a fraction of the total electrostatic energy and the lower the minimum voltage the larger it is. In Figure 11, the ratio of the usable energy E_{DC}^{use} and the total electrostatic energy E_{DC} is plotted against the ratio of the voltage variation ΔV_{DC} over the nominal voltage V_{DC0}.

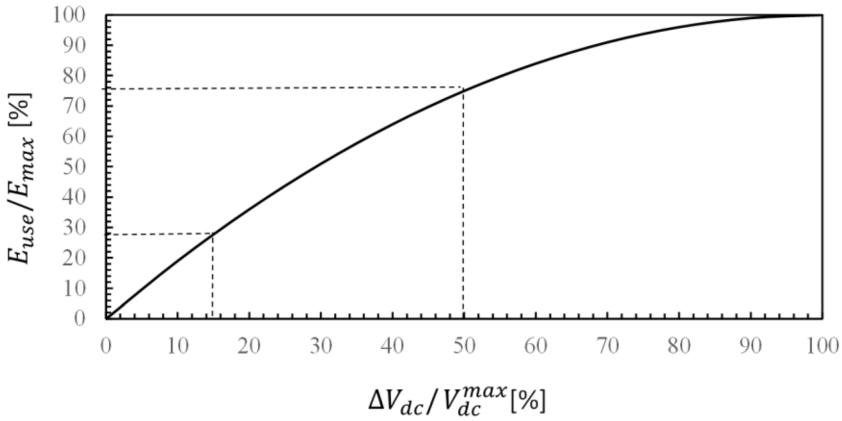

Figure 11. Ratio of the available energy over overall energy stored versus the ratio of the voltage deviation over the maximum voltage.

Considering a GSC with an AC voltage rated at $0.69\ kV$ and a DC voltage rated at $1.15\ kV$, the minimum allowable voltage, calculated using (3.22), is equal to $V_{DC}^{min} \cong 0.98\ kV$.

Therefore, the voltage variation is approximately equal to 15% and the accessible energy is 28% of the electrostatic stored in the DC-link.

To allow for adequate SI support, the capacitance of the DC-link, can be sized based on a given percentage n of the wind turbine rated power S_{WT} that is designed to be delivered during a frequency transient with an expected time duration Δt:

$$C_{DC} = \frac{1}{2}\frac{nS_{WT}\Delta t}{V_{DC0}^{2} - (V_{DC}^{min})^{2}} \tag{3.28}$$

3.2.2 Rotor kinetic energy and rotor-side converter synthetic inertia control scheme

To provide inertial response using the Rotor Kinetic energy Control (RKC), the wind turbine (WT) rotor is controlled to release or absorb Kinetic Energy (KE) in response to network's frequency changes. This is achieved by adding a frequency-sensitive auxiliary signal Δp_{RKC} to the active power reference of the RSC control, as depicted in light purple in Figure 7, and found in [38] – [42]. Unlike Synchronous Generators (SGs), whose speeds are directly coupled to the network frequency, Variable-Speed Wind Turbines (VSWTs) operate at a rotor angular speed (ω_r) different from the synchronous speed (ω_s). Furthermore, the speed variation of VSWTs can be significantly larger than the change in network frequency. Consequently, the inertial response of VSWTs, which is influenced by the pre-disturbance rotor speed, can be several times that of its natural inertia. The total kinetic energy ΔE_{RKC} that can be released or absorbed by the RKC, expressed in p.u., is given by:

$$\Delta E_{RKC} = \int_{t_0}^{t_1} \Delta p_{RKC}(t)dt = \frac{1}{2}J(\omega_{r1}^2 - \omega_{r0}^2) = \frac{1}{2}J(2\omega_{r0}\Delta\omega_r + \Delta\omega_r^2) \tag{3.29}$$

in which ω_{r1} is the rotor angular speed after the control has been applied, $\Delta\omega_r = \omega_{r1} - \omega_{r0}$ is the rotor speed variation, J is the angular moment of inertia of the rotor of the wind turbine and the IR support lasts for the time interval $\Delta t = t_1 - t_0$. For and under frequency event the RKC slows down the rotor to provide, for a brief period of time, more power to the grid. Therefore, the speed variation $\Delta\omega_r$ is negative as well as the KE variation ΔE_{RKC} of the WT's rotor which is in turn fed into the grid. From equation (3.29), is evident that the quantity of energy released by the RKC increases with a higher pre-disturbance speed ω_{r0} for a given rotor speed variation $\Delta\omega_r$. It is crucial to emphasize that the capacity of the RKC to provide IR is contingent on the available margin of KE in the initial operating conditions. In instances where a WT operates near the cut-in speed, characterized by low wind, RKC is infeasible for under-frequency events due to insufficient KE to be released. Similarly, when a WT operates in proximity to the maximum speed, RKC is not achievable during over-frequency events.

The active power variation Δp_{RKC} is given by the sum of a component linearly proportional to the RoCoF and a component linearly proportional to the frequency deviation:

$$\Delta p_{RKC} = -K_{RKC_I}\frac{df}{dt} + K_{RKC_D}\Delta f \tag{3.30}$$

where the two gains are constant, the first one represents the coefficient of inertia and the second one the droop coefficient. The active power deviation is added to the active power set-point provided by the MPPT control giving:

$$p_{MPPT}^{*} = p_{MPPT} - \Delta p_{RKC} \tag{3.31}$$

where p_{MPPT}^{*} is the adjusted active power set-point. The power mismatch between the WT's active power output p_{WT} and the WT's mechanical power p_W leads to rotor's acceleration until equilibrium is achieved. This can be written in the form of a typical swing equation as:

$$2H_S\omega_r\frac{d\omega_r}{dt} = p_W - p_{WT} \tag{3.32}$$

in which H_S is the total mechanical constant of inertia of the WT given by the sum of the turbine's constant of inertia H_T and the generator's inertia constant H_g. That is:

$$H_S = H_T + H_G \tag{3.33}$$

Given the fast response of the converters it is reasonable to assume that $p_{MPPT}^{*} = p_{WT}$, and substituting in (3.32) gives:

$$2H_S\omega_r\frac{d\omega_r}{dt} = p_W - p_{MPPT}^{*} \tag{3.34}$$

Since in steady state the equality relation $p_W = p_{WT}$ holds true and in order to quantify the constant of inertia H_R of the IR provided by the RKC this equation can also be rewritten in terms of network frequency variation, giving:

$$2H_R f\frac{df}{dt} = 2H_S\omega_r\frac{d\omega_r}{dt} \tag{3.35}$$

integrating in time both sides of (3.35) leads to:

$$\int_{f_0}^{f} 2H_R f df = \int_{\omega_{r0}}^{\omega_r} 2H_S\omega_r d\omega_r \tag{3.36}$$

$$H_R(f^2 - f_0^2) = H_S(\omega_r^2 - \omega_{r0}^2) \tag{3.37}$$

Another reasonable assumption is that this equation can be linearized around the initial operating point, that is frequency and angular speed undergo small variations, therefore:

$$H_R f_0 \Delta f = H_S \omega_{r0} \Delta\omega_r \tag{3.38}$$

rearranging:

$$H_R = \frac{H_S \omega_{r0} \Delta\omega_r}{f_0 \Delta f} \tag{3.39}$$

Therefore, the inertia constant associated with the IR of the RKC is directly proportional to the total WT inertia constant H_S, given by the sum of the rotor and the generator inertia constants, directly proportional to the pre-disturbance speed ω_{r0} and to the rotor speed variation $\Delta\omega_r$.

Conversely, to fully understand how the inertia coefficient K_{RKC_I} and the droop coefficient K_{RKC_D} of the RKC contribute to the inertia coefficient H_R, equation 3.31 can be substituted into 3.35 highlighting the contribution of the active power variation Δp_{RKC}:

$$2H_R f \frac{df}{dt} = p_{WT_0} - p_{MPPT} - \Delta p_{RKC} \tag{3.40}$$

integrating both sides in time gives:

$$\int_{t_0}^{t} 2H_R f df = \int_{t_0}^{t} p_{WT_0} dt - \int_{t_0}^{t} p_{MPPT} dt - \int_{t_0}^{t} \Delta p_{RKC} dt \tag{3.41}$$

$$H_R f_0 \Delta f = p_{WT_0} \Delta t - \int_{t_0}^{t} p_{MPPT} dt - \int_{t_0}^{t} \Delta p_{RKC} dt \tag{3.42}$$

$$H_R = \frac{p_{WT_0} \Delta t - \int_{t_0}^{t} p_{MPPT} dt - \int_{t_0}^{t} \Delta p_{RKC} dt}{f_0 \Delta f} \tag{3.43}$$

substituting (3.30) into (3.43) gives:

$$H_R = \frac{p_{WT_0} \Delta t - \int_{t_0}^{t} p_{MPPT} dt - \int_{t_0}^{t} K_{RKC_D} \Delta f dt + \int_{t_0}^{t} K_{RKC_I} df}{f_0 \Delta f} \tag{3.44}$$

In the RSC control, the angular speed of the WT is determined by a PI controller with gains calibrated in such a way as to allow rapid speed variations necessary to provide RKC support, followed by a swift speed recovery. During this phase in which the speed goes back to its reference value, the WT does not produce energy, resulting in a period of under-production where the output power is lower than the pre-disturbance value. This situation can be problematic, especially if the speed recovery coincides with other conventional generators not having yet increased their output sufficiently to compensate for the frequency variation.

For optimal generator performance, a rotor speed recovery time of 20 seconds is considered sufficiently fast [38]. However, the duration of the network frequency transient is contingent upon the dynamics of the network. In networks with fast dynamics, frequency transients occur rapidly, typically within 2-3 seconds. In such cases, a speed-recovery time of 20 seconds proves adequate to provide dynamic frequency support. Conversely, in networks with very slow dynamics, frequency transients may unfold over a more extended period, exceeding 20 seconds. In such instances, Rotor Kinetic Energy Control (RKC) may exacerbate the frequency nadir rather than providing support.

3.2.3 Frequency response emulation from deloading technique

The implementation of MPPT control aims to optimize energy conversion efficiency but renders WTS incapable of providing frequency support for extended periods of time. To enable WTs to contribute to frequency regulation, a certain amount of primary reserve must be provided. This is achieved through continuous deloading of the turbine output, which can be accomplished in three different ways [43]. Either by reducing the maximum active power by a constant percentage (referred to as delta control), or by imposing an upper limit on the turbine output (balance control) or reserving a constant pre-defined amount of active power (fixed reserve). In this thesis, the delta deloading control is adopted, designed to secure a fixed percentage ($\%d$) of the WT output as power reserve. This is achieved through either over-speed deloading (ω_0) or pitch deloading methods (β_0), which are highlighted in light red in the RSC control architecture shown in Figure 7.

The deloading technique is depicted in Figure 12, for a given wind speed the turbine is operating at the optimal blades' pitch angle (β_1) producing the maximum amount of mechanical power (point A). Whether the rotor speed is increased (e.g., from point A to B) or decreased (from A to C), the mechanical power output decreases. These methods are known as over-speed deloading and under-speed deloading, respectively. However, from a power system perspective, the under-speed deloading method may be considered unstable [42]. An alternative method, namely pitch deloading, can be implemented by increasing the pitch angle from the value β_1 to β_2 while maintaining the optimal rotor speed, moving the operating point from A to D.

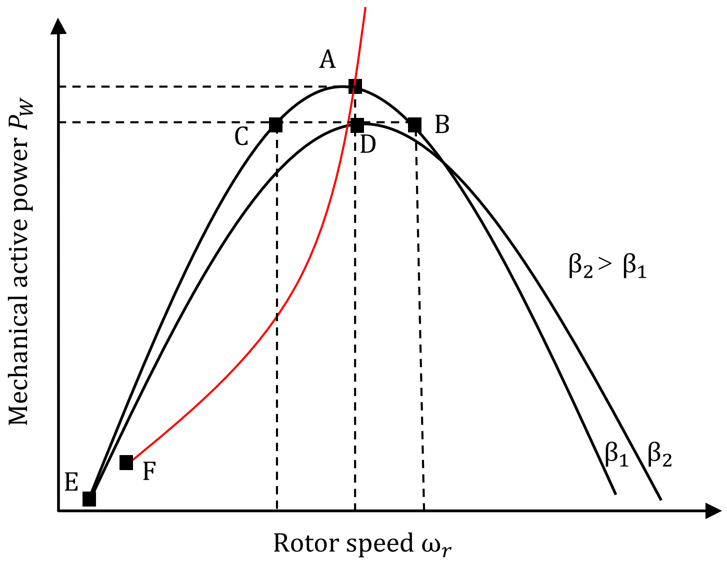

Figure 12. Deloading options for a WT operating at a given wind speed in point D. The red curve represents the maximum power curve.

The over-speed deloading technique increases the kinetic energy reserve of the rotating mass by allowing the rotor speed to go beyond its optimum value. This is achieved by incrementing the rotor speed reference produced by the MPPT control, denoted in Figure 7 as ω_r^{ref}, by a factor $\Delta\omega_r^{ref} = \omega_0$, corresponding to the desired active power deloading percentage $\%d$. Moreover, to implement PFR, the WT responds to frequency deviations Δf by modifying ω_0 through the following relationship:

$$\Delta\omega_r^{ref} = \omega_0(1 + K_\omega \Delta f) \tag{3.45}$$

In case of an under-frequency event ($\Delta f < 0$), and a positive value of the adjustment factor K_ω, the adjusted rotor speed is less than the speed set to achieve over-speed deloading $\Delta\omega_r^{ref} < \omega_0$. Therefore, the WT can produce more power and contributing to the stemming of frequency deviation.

In the case of pitch deloading, the pitch angle reference, denoted as β^{ref}, generated from the rotor speed limiting controller is increased by a factor $\Delta\beta^{ref} = \beta_0$, corresponding to the deloading percentage $\%d$. Furthermore, to implement PFR, the WT responds to frequency deviations Δf by adjusting $\Delta\beta^{ref}$ through the following relationship:

$$\Delta\beta_r^{ref} = \beta_0(1 + K_\beta \Delta f) \tag{3.46}$$

Depending on the desired active power deloading percentage the values of β_0 and ω_0 are calculated based on power curve and WTs' dependent technical datasheets.

Given the two different deloading control strategies presented, the power curve characteristic of a wind turbine can be divided into three wind speed regimes. The power optimization operative region, that goes from the cut-in wind speed to the rated wind speed, can be divide into two zones. The power limitation regime, that goes from the rated wind speed to the cut-out wind speed, corresponds to the third zone. In the proposed deloading control strategy, over-speed deloading is employed in the low-speed zone, ($\omega < 1.5\, rad/s$), a coordinated use of both over-speed and pitch deloading is adopted in the medium-speed zone ($1.5\, rad/s < \omega < 1.5\, rad/s$), and only pitch deloading is applied in the high-speed zone ($\omega > 2.5\, rad/s$).

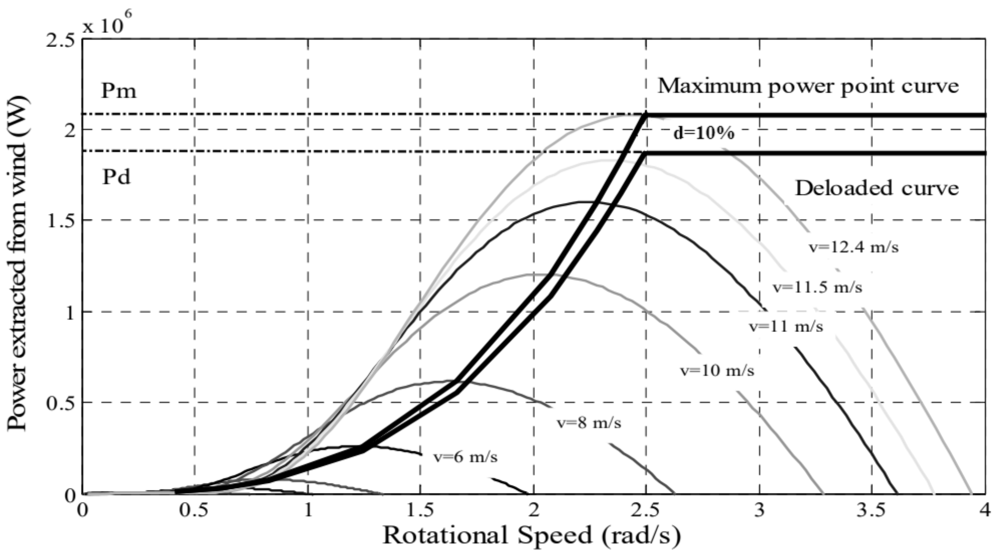

Figure 13. Wind turbine power curve with MPPT and de-loading (Adapted from [44]).

3.3 Battery Energy Storage Systems Coupled with Wind Farms

In the evolving landscape of power systems, the integration of BESS has emerged as a pivotal solution for enhancing network stability and reliability. These systems, whether deployed as standalone grid-connected entities or in tandem with renewable energy sources like PV plants and wind farms, offer a versatile approach to addressing the challenges posed by the variability and intermittency of renewable energy generation. Various energy storage technologies have been categorized and explored for diverse grid applications, including enhancing power quality and delivering frequency regulation to the grid in the event of network disturbances [43], [45]. This section delves into the diverse technologies and solutions encompassed within BESS, highlighting their potential to contribute significantly to both frequency and small-signal stability of power grids.

By offering rapid response capabilities, these systems can inject or absorb power to counterbalance frequency deviations, thereby ensuring a consistent and reliable power supply. Furthermore, through dynamic control strategies, BESS can provide damping and support to counteract the effects of small disturbances, enhancing overall grid resilience.

When coupled with wind farms, BESS can effectively smooth out the power output fluctuations caused by varying wind speeds. Similarly, pairing BESS with PV plants addresses the inherent intermittency of solar power. This synergy enhances the predictability and reliability of RES and allows for more efficient utilization of the generated power.

This section aims to provide a concise overview of the diverse range of energy storage technologies, with a focus on lithium-ion batteries and supercapacitors. Each of these technologies has a different set of characteristics in terms of energy density, output power and lifecycle that determine their most suitable application within the power grid.

Following the exploration of BESS technologies, the focus will shift to their integration within wind farms. The discussion will extend to stan-alone grid-scale BESS and the operational dynamics of converters in these settings, encompassing both grid-following and grid-forming modes.

Finally, the BES control model adopted in this study and its frequency controller, will be discussed. This controller enables the BESS to provide SI and PFR allowing it to contribute to the grid's frequency support.

3.3.1 Energy storage technologies overview

Energy storage solutions span a variety of rapidly evolving technologies with radically different characteristics and applications. The Ragone plot is the well-known graphical representation used in the context of ESS. Shown in Figure 14, it plots the power rating of a specific energy storage solution against its energy capacity, isochrone lines are drawn to indicate the typical discharge time.

On the left side of the chart, technologies with shorter discharge times and high power densities, such as supercapacitors, can be found. While these technologies can be suitable for IR, they are not capable of providing energy for an extended period of time, necessary for PFR. In contrast, technologies like lithium-ion batteries, with discharge times typically ranging from 1 to 10 hours, possess the necessary energy capacity to sustain support throughout the duration of PFR.

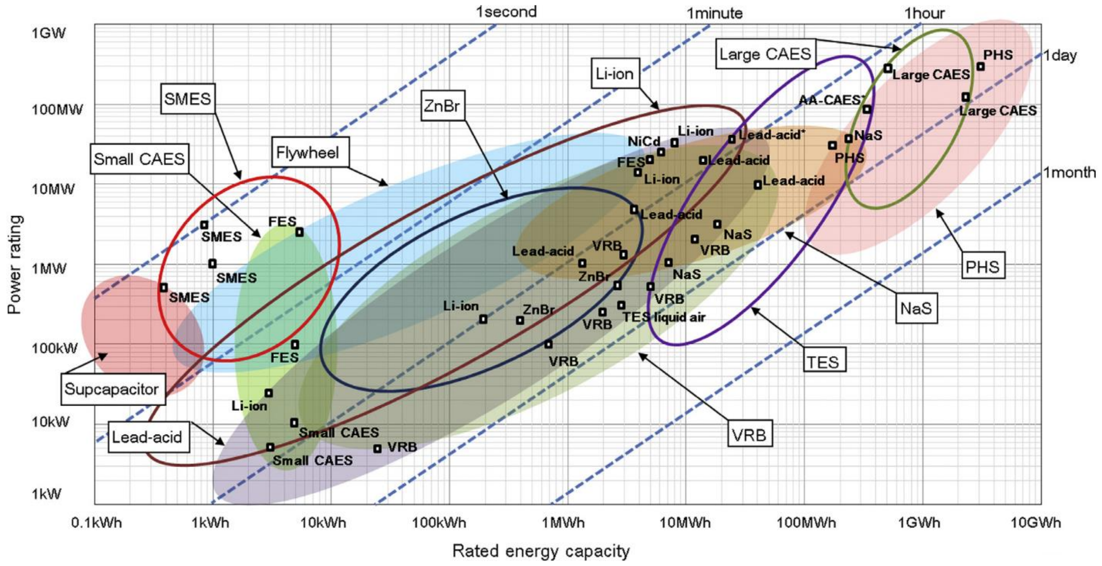

Figure 14. Energy storage options, ranked by power rating and energy capacity. Isochrone lines indicate the typical discharging time [46].

The number and the size grid-scale BESS installations has increased tremendously in recent years. One of such system is the 150 MW/194 MWh Hornsdale Power Reserve (HPR) which is coupled with a wind farm, and in 2017, at the time of its installation, was the largest BES installation in the world [47]. In its first period of operation, HPR has proved to be both profitable and essential in guarantying frequency stability of the South Australian grid [48]. In 2022, it started providing 2000 MWs of SI to the grid, being the first BESS to provide a type of ancillary service usually provided by synchronous generators. Many of such plants have been installed in recent years and many more are planned in the coming years, simultaneously driven and driving lithium-ion batteries' prices down.

3.3.2 Energy storage architecture within a wind farm

In the following, the possible locations for the installation of supercapacitors and BES, within a wind farm, as explored in the literature and shown in Figure 15 is discussed.

a) **Direct DC-Link Interface**: Shown in Figure 15(a), the ESS is connected directly to the wind turbine's DC-link, without a DC/DC converter. For instance, Li-ion supercapacitors directly linked to the DC-link have been proposed to stabilize power output [49]. This configuration can provide SI support, reducing the RoCoF and dampening frequency oscillations. Advantages include lower cost and energy loss due to the absence of an additional conversion stage, and simplified control coordination. However, drawbacks include the need for GSC rerating to handle the total expected power and limited usable energy from the supercapacitors due to GSC's maximum DC voltage variation limitations.

b) **DC-Link Interface via DC/DC Converter:** Shown in Figure 15(b), this configuration employs a DC/DC converter for ESS connection to the DC-link. Supercapacitors connected this way can provide the necessary SI and enhance small-signal stability [50]. The supercapacitor's minimum voltage isn't limited by the GSC's PWM constraints, allowing full utilization of stored energy. However, it shares the same drawback of needing GSC rerating, and introduces additional costs and energy losses due to the extra conversion stage, along with increased control complexity.

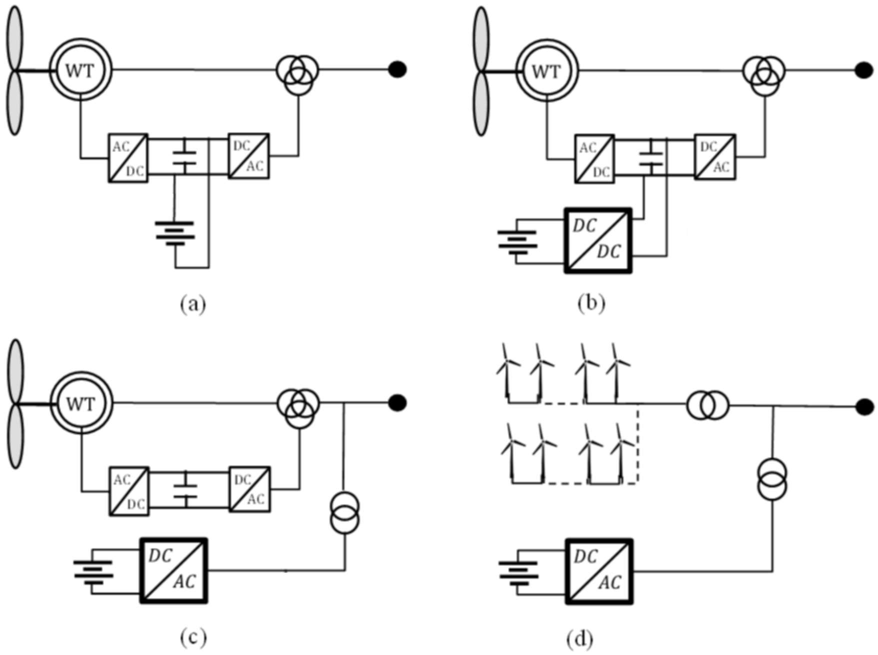

Figure 15. Possible locations for the installations of ESS within a wind farm.

c) **AC Side Interface via DC/AC Converter**: Shown in Figure 15(c), it is similar to location (b) in terms of energy transmission, this option involves interfacing the ESS to the WT via a DC/AC converter at the AC side of the GSC. A BESS operating as a virtual synchronous generator connected this way avoids the need for GSC rerating [51]. However, it also increases costs and energy losses due to the additional conversion stage and complicates control coordination.

d) **WF Level, Common Coupling Point:** Shown in Figure 15(d), this placement involves interfacing the ESS at the wind farm level, at the point of common coupling. This approach has been previously explored in studies [52].

3.3.3 Grid-forming and grid-following operating modes

Literature commonly categorizes the control strategies ESS in power system frequency response into two principal types: current-controlled and voltage-controlled frameworks. The current-controlled approach is further divided into:

- **Grid-Following Converters**: These converters function as current sources, injecting active and reactive power into the grid based on predefined references. They determine the grid voltage angle through a phase-locked loop. However, this method does not provide dynamic frequency support to the grid.
- **Grid-Supporting Converters:** Like grid-following converters, but with an additional feature of dynamic frequency response. They adjust their active power output in response to frequency variations. This approach is often described as a virtual synchronous generator [53].

On the other hand, the voltage-controlled approach splits into:

- **Grid-Leading Converters:** These converters actively establish grid voltage by maintaining a constant voltage angle and frequency. Commonly used in isolated grids like small islands or offshore networks, this V/f control strategy forms the grid voltage solely through one converter.
- **Grid-Forming Converters:** These converters not only establish grid voltage but also synchronize with other converters or generators. Various grid-forming control concepts, including virtual synchronous machines, synchronverters, and droop control, have been suggested in the literature [54].

3.3.4 BES model and frequency controller

This subsection introduces the BESS model and its associated control mechanisms, as utilized in the simulation studies detailed in the following chapters. This study employs a straightforward battery model that characterizes the battery's terminal voltage and internal resistance. The internal resistance is considered constant, while the terminal voltage varies based on the battery's State of Charge (SoC), as defined in (3.47).

$$V_{dc} = V_{max}(1 - SoC) - Z_i I_{bat} \tag{3.47}$$

Where V_{dc} denotes the terminal voltage and I_{bat} represents the battery current.

The BESS control architecture is composed of several key components:

Frequency Controller: As illustrated in Figure 19, where it's marked in red, the frequency controller's role is to adjust the active power reference. This adjustment includes elements of both frequency derivative and frequency deviation. The branch proportional to the frequency derivative, denoted by the gain K_I, represents the SI component while the branch proportional to the frequency deviation and passing through gain K_D, represents the PFR component. A value of K_D equal to 20 pu corresponds to a droop equal to 5 %.

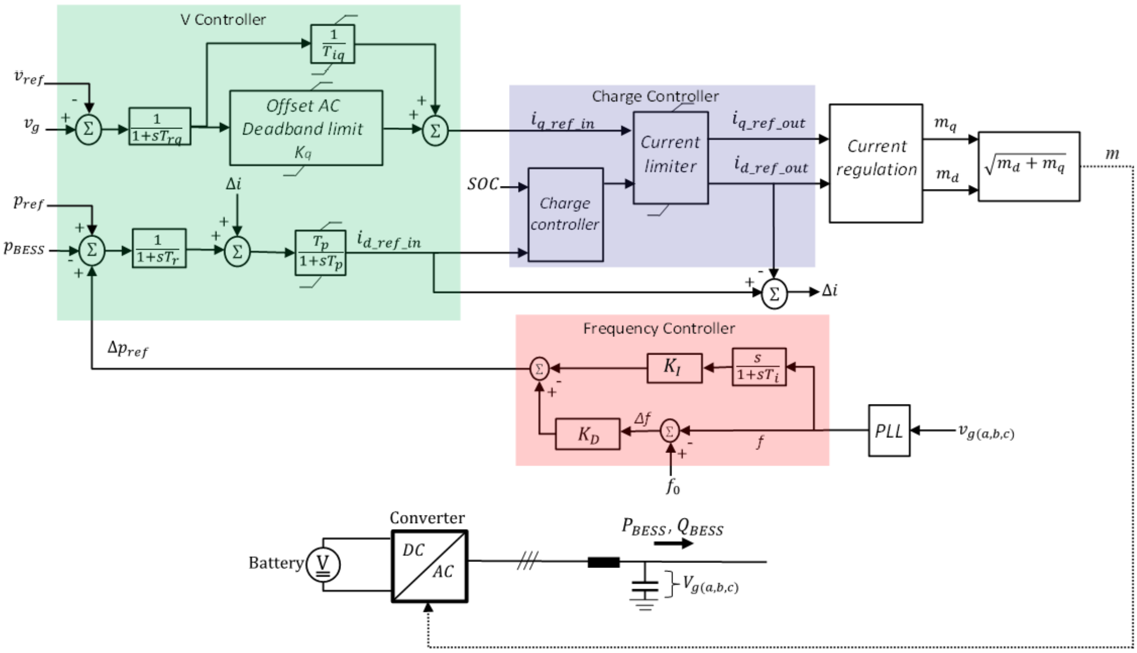

Figure 16. Grid-supporting BESS control architecture.

Voltage Controller: Indicated in green in Figure 19, the voltage controller's function is to regulate the output active power and output voltage to the predetermined reference values. It incorporates a slow-acting integer-controller for tracking set points, alongside a proportional voltage support mechanism characterized by a slope with a dead band.

Charger Controller: Shown in blue in Figure 19, the charge controller is tasked with limiting the absolute value of the current, ensuring it stays within the designated range. It also ensures that the SoC stays within its maximum and minimum value, stopping the battery from recharging when the maximum value is reached and from discharging when the minimum value is reached. The battery SoC is determined by a Coulomb counting model:

$$SoC(t) = -\frac{1}{C_b \cdot 3600}\int_0^t I_{DC}(\tau)d\tau + SoC_0, \tag{3.48}$$

where $C_b$is the battery capacity in Ah and SoC_0 represents the initial condition. Two important assumptions worth to be mentioned are that capacity C_b is constant, and voltage U_{DC} is linearly dependent on the SoC. These approximations are acceptable in the context of the present study since dynamical simulations are executed in a short time scale, from hundreds of milliseconds up to tens of seconds.

Chapter 4. Coordinated Synthetic Inertia Support by Wind Turbine Generators

In the previous chapter two control architectures that allow Variable-Speed Wind Turbines (VSWTs) to provide SI have been presented. Namely the Grid-Side Converter (GSC) control, shown in Figure 8, which allows to access to the electrostatic energy stored in the DC-link by varying the voltage V_{DC} in response to frequency changes and the Rotor-Side Converter (RSC) control, shown in Figure 7, which allows to act upon the speed of rotation of the wind turbine to release or absorb kinetic energy to provide IR. Even though these controls have been presented considering a Doubly-Fed Induction Generator (DFIG) wind turbine, the main characteristics of the proposed approach can be adapted also for other types of VSWTs (e.g., Permanent Magnet Synchronous Generator (PMSG) wind turbines).

In this chapter a coordinated control architecture that combines the DC-link GSC control and the rotor kinetic energy control (RKC) is proposed. Regarding the DC-link GSC control architecture two control modes have been previously discussed, namely the Current-Controlled Mode (CCM) and the Voltage-Controlled Mode (VCM). However, as discussed in section 3.2.1B, the parameters of the DC voltage PI controller are set to ensure a slow response for the CCM IR architecture, allowing it to access the stored energy before that the PI restores the DC voltage within its nominal values. This characteristic does not allow to integrate the CCM in a coordinated control strategy as to guarantee a correct functioning of the RKC the voltage of the DC-link cannot deviate from its operational range for extended periods of time. On the other hand, the short response time of the DC-link VCM IR strategy, allows it to couple with the RKC architecture implemented on the RSC control.

In the next chapter, wind turbines implementing this control strategy and flexibility options provided by battery energy storage and other RES, will be utilized to assess the stability of two forecasted scenarios for a very large and complex system, the Sicilian network. Before venturing in the stability analysis of a large and intricate network, the influence of the coordinated control strategy on small-signal and frequency stability is studied on a smaller benchmark test network known as the Two-Areas Four-Generators (2A4G) test network. This transmission network, firstly presented by Kundur as been proposed as an IEEE stability benchmark test network, and it is especially designed to show an unstable inter-area mode and to test different kind of solutions to enhance its stability [56].

4.1 DC-link and Rotor Kinetic Energy coordinated control strategy

The coordinated control is obtained by combining the DC-link VCM IR support and RKC SI support with a power reserve guaranteed by a constant 5% deloading. Papers [57] – [59] explore the use of supercapacitors integrated into the DC-link of the turbine to guarantee the required support. Similarly, authors in [60] – [62] utilize the rotor's control to harness the stored energy in the turbines for the same purpose. Additionally, the potential of leveraging both the electrostatic energy stored in the DC-link and the rotor's kinetic energy provide SI support is presented in [63] –[65], with results indicating that the coordinated scheme leads to enhancements in network frequency response with respect to the single schemes considered separately.

However, the stability of the power system remains uncertain without considering the impact of the improved SI support on small-signal stability. While findings presented in [66] hint at a positive influence on small-signal stability, conclusions drawn in [67] point to the fact that SI support can yield either a positive or negative impact on system damping. This variability hinges on the parameters of the PLL. Additionally, outcomes presented in [68] imply a reduction in small-signal stability when SI support is integrated into the control architecture of the DFIG wind turbine. Likewise, findings in [69] state that network instability might happen with control parameters set inappropriately, leading to the suggestion of specific, delimited regions to prevent the detrimental effects on small-signal stability. Finally, in [70], a method is proposed for setting coordinated control parameters in wind farms employing SI support that aims at concurrently address both frequency and small-signal stability.

The SI contribution in terms of constant of inertia provided by the coordinated control strategy can be estimated for each wind turbine, and thus for the whole wind farm, by adding the inertia constants associated to each control, that is (3.15) and (3.19):

$$H_{WT} = K_{DC}\frac{c_{DC}v_{DC0}}{2f_0} + \frac{H_S\omega_{r0}\Delta\omega_r}{f_0\Delta f} \tag{4.1}$$

where the gain K_{in_V} has been renamed K_{DC} since there is no more ambiguity whether the GSC is operated in VCM or CCM, the latter is incompatible with the RKC. The first term of the equation corresponds to the contribution provided by the GSC control while the second one to the RSC control. In which the constant of inertia H_S, represents the actual inertia of the wind turbine comprised by the sum of the rotor and the generator's constant of inertia.

4.2 Benchmark test network: 2-Area 4-Generator

In this section, the influence of the coordinated control strategy on the small-signal stability and on the frequency response of the benchmark test network "2-Area 4-Generator" is examined. This 230 kV transmission network consists of 2 symmetric areas with 2 generators and 5 buses each interconnected by a double tie line for a total of 11 buses. This test system is very well-known, and it has been thoroughly documented [23]. Given its symmetric structure, it displays two local modes associated with areas 1 and 2 that may exhibit nearly identical oscillation frequencies, contingent on various factors, including power flow conditions [55]. Although, the main characteristic of the network is a poorly damped inter-area mode, between areas 1 and 2, with a lower oscillation frequency than the local modes. This network holds historical significance, and it has been used to showcase that Power System Stabilizers (PSSs) can effectively contribute to the simultaneous damping of both inter-area and local electromechanical modes with closely matched frequencies. For all these reasons, the *IEEE Task Force on Benchmark Systems for Stability Controls* has selected it, among others, as a benchmark test network for small-signal and frequency stability studies [56]. In the original system, each generator has a rating of 900 MVA and a rated voltage of 20 kV, Figure 17 shows its single line diagram. The network is symmetric with respect to bus 8 and the tie-line connecting bus 7 and bus 9 is 220 km long, to these two buses there are a load and capacitor bank connected. The system is slightly asymmetric in the sense that the generators are identical within each area but slightly different between the two areas, the constant of inertia of the generators in area 1 is equal to 6.5 s while the constant of inertia of the generators in area 2 is equal to 6.175 s.

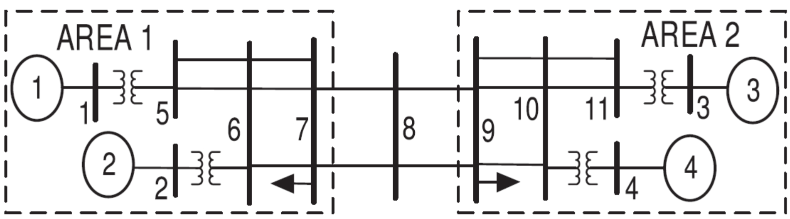

Figure 17. Single line diagram of the "2-Area 4-Generator" benchmark test network [56].

In order to test the effectiveness of the wind turbines' IR coordinated control scheme. the 2A4G network has been adapted to our study case by connecting a 600 MVA wind farm to bus 6, corresponding to a fourth of the installed power in area 1, has shown in Figure 18.

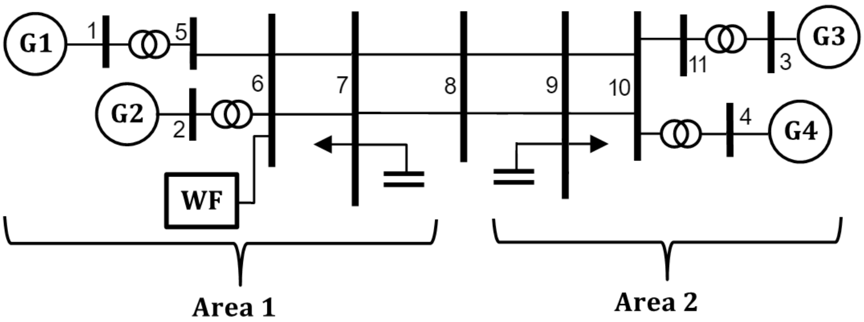

Figure 18. Adapted version of the 2-Area 4-Generator benchmark test network, a wind farm is connected to bus 6 [66].

To assess the impact of the added wind farm on the small-signal stability we shall begin by performing a modal analysis on the original 2A4G network as well as on its adapted version. For the time being the wind farm does not provide any IR support. As known, the network displays three ElectroMechanical (EM) oscillatory modes: a local mode for each area, in which the two generators oscillate against each other (e.g., The local mode of area 1, G1 oscillates in counter phase with respect to G2), and an inter-area mode in which the generators within each area oscillates in phase with respect to each other but in counterphase with respect to the generators of the opposite area (e.g., G1 and G2 oscillate against G3 and G4). In Table 2, the modal analysis comparing the properties of the 3 EM modes is presented for the original and adapted 2A4G network. The eigenvalues, the frequency of oscillation and the damping factor of each mode are reported, an explanation on how to calculate these values is discussed in the introduction.

Table 2. Modal analysis results for the original and adapted version of the 2A4G network.

Network	EM mode	Generators	Eigenvalues	$f\ (Hz)$	ζ (%)
Original 2A4G	Inter-area	1, 2 vs 3,4	- 0.002 ± j 3.582	0.57	0.07
	Local area 1	1 vs 2	- 0.519 ± j 6.259	0.99	8.26
	Local area 2	3 vs 4	- 0.471 ± j 6.473	1.03	7.26
Adapted 2A4G	Inter-area	1, 2 vs 3,4	- 0.017 ± j 3.644	0.58	0.46
	Local area 1	1 vs 2	- 0.735 ± j 6.032	0.96	12.1
	Local area 2	3 vs 4	- 0.471 ± j 6.472	1.03	7.26

To better comprehend and more easily visualize the results of the modal analysis, the eigenvalues of the 3 EM modes are plotted in Figure 19 for both the original network, shown as blue circles, and for the adapted network, red crosses. The dashed line corresponds to a damping factor equal to 5%, which is the minimum accepted small-signal stability threshold. The amplitude of an oscillatory mode with a 5% damping factor reduces by 79% after 5 periods, while with a damping of 10% the amplitude of the oscillations reduces by 96% after 5 periods [8]. Modes which eigenvalues are to the right of the 5% damping line are properly damped, while modes to its left, even if with a negative real part, cannot considered to be stable. The unstable inter-area mode, to the right of the dashed line, moves slightly towards the left half-plane with the introduction of the wind farm in area 1. The local mode of area 2, namely M_2, is completely unaffected by the introduction of the wind farm in area 1, while the local mode of area 1, M_1, moves significantly to the left. The damping factor of mode M_1 increases from a value of 8.26% in the original network to a value of 12.1% in the wind-farm-adapted one, which is above of the 10% conservative threshold.

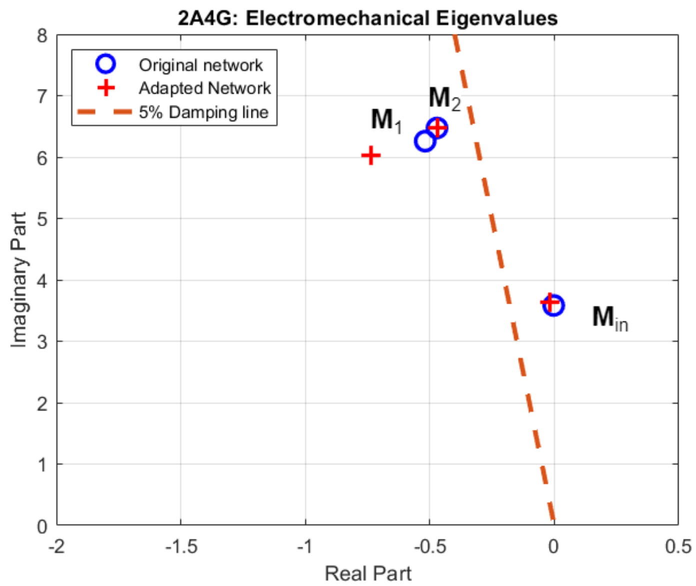

Figure 19. Root loci of the eigenvalues of the electromechanical modes of the original and adapted version of the "2-Area 4-Generator" test network.

As we will see, the local mode of area 2 its completely unaffected by the wind farm in area 1, whether it provides SI support or not. Therefore, the focus of the following analysis will be the contribution of the wind turbines to the stabilization of the poorly damped inter-area mode and to a lesser extent the effect of the IR support on local mode M_1. In Figure 20, the oscillation vector of inter-area mode M_{in} is reported, which shows how the speed deviations of the units G1 and G2 oscillate in counterphase with respect to the speed deviations of units G3 and G4, and the units of area 2 have a higher participation factor in the inter-area mode. This is due to the fact that, given the same governor and AVR control, the generation units of area 2 have a 5% smaller inertia constant.

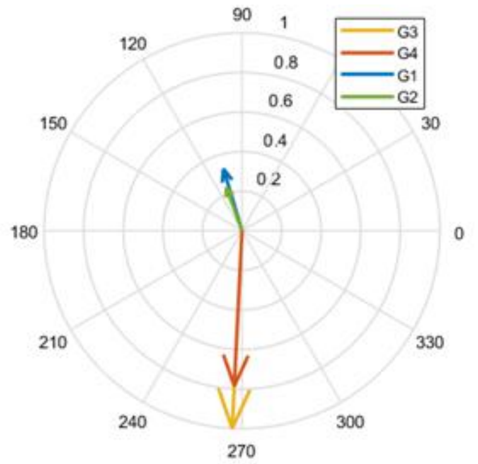

Figure 20. Oscillation vector of the inter-area mode of the "2-Area 4-Generator" test network.

To assess the impact of the wind turbines' SI support control strategies on the small-signal stability of the network, the gains of the DC-link control strategy and of the RKC are increased in discrete steps of 2, ranging from a value of 0, corresponding to no SI support, to a value of 30. This is done for the two controls separately as well as for the coordinated SI control strategy, in which the two controls operate in conjunction. The results are reported in Table 3, and for the sake of conciseness, of the total number of tested values only 4 significant ones are reported, i.e., 0, 10, 20 and 30. The results are reported in Table 3, and for the sake of conciseness, of the total number of tested values only 4 significant ones are reported, i.e., 0, 10, 20 and 30.

Table 3. Frequency and damping factor of the three electromechanical modes in the modified 2A4G network with different degrees and combinations of SI support from the wind turbines.

IR Support	(K_{RKC}, K_{DC})	Inter-area M_{in}		Local M_1		Local M_2	
		$f(Hz)$	$\zeta(\%)$	$f(Hz)$	$\zeta(\%)$	$f(Hz)$	$\zeta(\%)$
None	(0, 0)	0.58	0.46	0.96	12.1	1.03	7.26
DC-link	(0, 10)	0.57	2.82	0.96	12.2	1.03	7.27
	(0, 20)	0.56	4.21	0.98	12.6	1.03	7.27
	(0, 30)	0.55	4.79	0.99	11.9	1.03	7.27
RKC	(10, 0)	0.57	0.67	0.96	12.1	1.03	7.26
	(20, 0)	0.56	1.28	0.97	12.6	1.03	7.27
	(30, 0)	0.56	1.71	0.99	12.0	1.03	7.27
Coordinated	(10, 10)	0.57	2.87	0.97	12.3	1.03	7.27
	(20, 20)	0.56	4.24	0.99	12.7	1.03	7.27
	(30, 30)	0.55	4.95	1.00	11.8	1.03	7.27

As previously anticipated, the local mode of area 2 is totally unaffected by the SI support strategies implemented in area 1, as one might reasonably expect. Regarding the poorly damped inter-area mode, the SI support strategies affect its frequency of oscillation by just a few percent while increasing its damping ratio by a factor greater than 10. Considering only DC-link support, the damping factor increases from a value of 0.46% to a value of 4.79% for a gain value of 30. The contribution of just the RKC increases the damping ratio up to a value of 1.71% while the coordinated action of the two controllers takes it up to 4.95%, very close to the 5% small-signal stability threshold and a few percent more than with just the DC-link support. The result of this sensitivity analysis on the root locus of the EM modes with respect to linearly increasing values of the gains of the coordinated SI support scheme are plotted in Figure 21 for the inter-area and for the local mode of area 1.

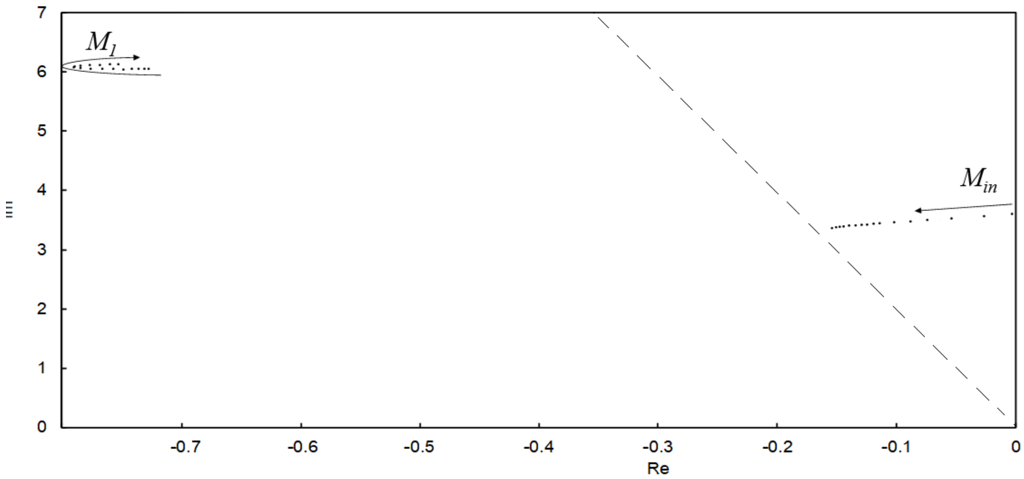

Figure 21. Root locus of the inter-area mode (M_{in}) and of the local mode (M_1) of area 1 for increasing values of the gains of the coordinated SI support strategy.

Regarding the inter-area mode M_{in}, increasing linearly the values of the two gains simultaneously from 0 to 30, it migrates towards the left half-plane at a decelerating pace following a straight line and stopping just before the 5% damping threshold. With respect to the local mode M_1, on the other hand, as the value of the two gains increases, the eigenvalue moves initially towards the left half-plane reversing its direction when the value of the two gains reaches 20 and giving back all the improvements made in terms of damping factor at a value of 30.

From the small-signal stability analysis it can be concluded that, albeit slightly better in terms of damping the oscillatory modes, the coordinated IR support strategy provides marginal benefits compared to the two strategies considered separately.

The increase in damping factor is not linear with raising the values of the two gains. After a value of 20 the direction of mode M_1 reverses and the pace of migration of mode M_{in} slows down. Nonetheless, the coordination of the two control schemes increases the damping factor of the unstable inter-area mode more than tenfold without compromising the stability of the two local modes nor sensibly affecting their frequency. Two sensible judgement criteria could be adopted to choose the most suitable gain combination for the coordinated control scheme. Either the one that maximizes the stability of the interarea mode without compromising the stability of the local mode (e.g., $(K_{RKC}, K_{DC}) = (30{,}30)$) or the one that maximizes the stability of the local mode while still increasing the stability of the inter-area mode (e.g., $(K_{RKC}, K_{DC}) = (20{,}20)$) and taking advantage of most of the improvement.

To excite the unstable inter-area mode and comparing the frequency response of the network with and without the support of the coordinated IR scheme, the loss of one of the four sections of the tie-line connecting area 1 and 2 is simulated at $t = 2s$, as shown in Figure 22. The fault is simulated in an operating condition in which the wind energy produced in area 1 has a power penetration level of 25%. The results are presented considering the following controller configurations:

1) no SI support: $(K_{RKC}, K_{DC}) = (0{,}0)$
2) DC-link SI: $(K_{RKC}, K_{DC}) = (0{,}30)$
3) RKC SI: $(K_{RKC}, K_{DC}) = (30{,}0)$
4) Coordinated SI support: $(K_{RKC}, K_{DC}) = (30{,}30)$

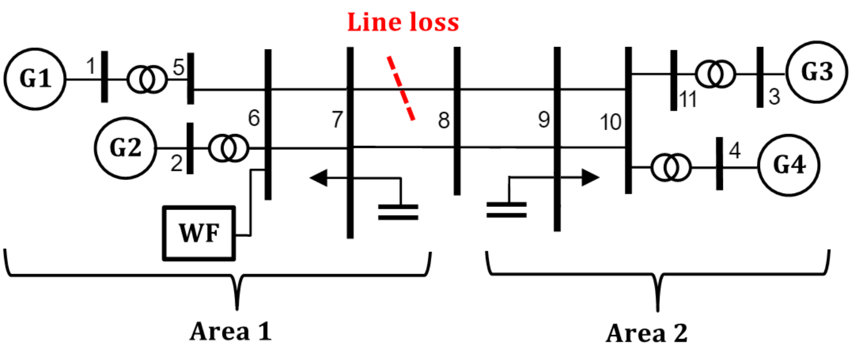

Figure 22. Simulated fault in the adapted 2A4G network.

Since generating unit G3 is the one with the highest participation factor in the inter-area mode, we will be looking at its speed deviation, directly linked at the frequency of area 2, as well as the power output for the wind farm for the four different IR support cases. The speed deviation of G3 after the perturbation is shown in p.u. in Figure 23, without any IR support (in red), the speed oscillations are poorly damped and persist with a significant amplitude for more than 20 seconds. The introduction of any IR support, damps significantly the speed oscillations, with the coordinated control strategy (in dashed black) reducing the speed zenith excursion the most, followed by the DC-link IR control (in dot-dashed blue) and finally by the RKC (in dashed green).

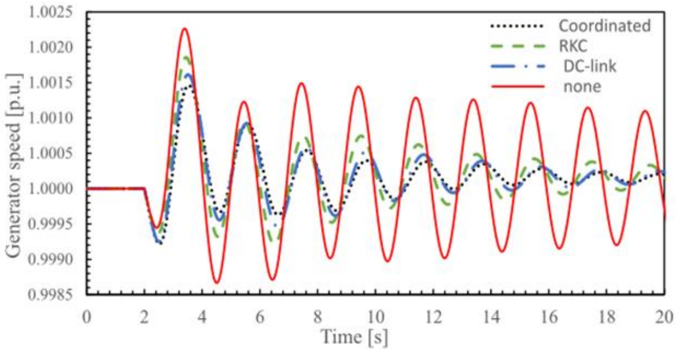

Figure 23. Speed deviations of synchronous generator G3 after the loss of segment of the tie-line in the 2A4G network for different degrees of IR support.

Finally, the wind farm's active power output following the perturbation is shown for the different cases in Figure 24. The coordinated control strategy is slightly more capable of absorbing and releasing power with respect of the DC-link IR support, closely followed by the RKC.

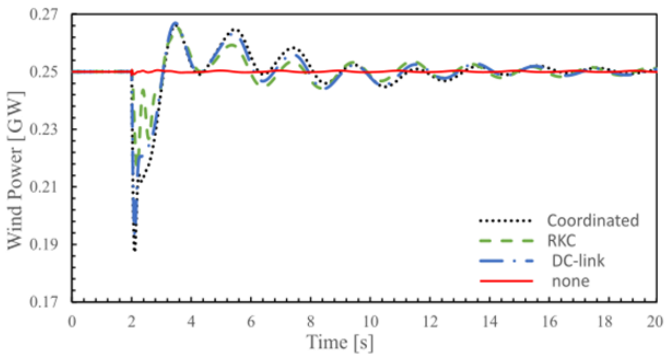

Figure 24. Wind farm active power output after the loss of segment of the tie-line in the 2A4G network for different degrees of IR support.

Chapter 5. The Case of the Sicilian Network: Contribution of RES ancillary services to Power System Small-Signal Stability

This chapter comprehensively summarizes the research conducted by the University of Bologna for the European project OSMOSE [72]. The task of the Ensiel Consortium within project Osmose was to evaluate the impact of innovative flexibility sources on power system stability, mainly with reference to the sources identified by Réseau de Transport d'Électricité (RTE), the French TSO [73]. The dynamic stability of the grid is evaluated against typical power system disturbances. This evaluation is conducted using advanced models of power system and controls in the DIgSILENT PowerFactory software.

Two timeframes, 2030 and 2050, are considered, based on forecasted scenarios identified by the Technische Universität Berlin (TUB). For each scenario, 6 dispatching profiles, i.e., operating conditions encompassing every major corner case, are identified by Monte Carlo simulation [74]. The electrical network model for the simulations is supplied by Terna, the Italian TSO, subject to data disclosure restrictions, focusing on a part of the Italian system, the Sicilian network.

In this thesis, particular focus is posed on the influence of IR services provided by RES on the small-signal stability. For the 2030 forecasted scenario, the controller implementing the proposed RKC and DC-link IR schemes in wind power plants is under scrutiny. For the 2050 scenario, this approach is extended to IR and PFR provided by grid-scale BESS.

The chapter begins with a description of the modal analysis procedure followed, then the grid model and the necessary updates to match the forecasted scenarios are presented. After the stage as been set, we dive into the small-signal stability analysis of the 6 different operating conditions identified for each forecasted scenario.

5.1 Modal Analysis Procedure

The modal/eigenvalue analysis tool, incorporated in the DIgSILENT PowerFactory software, has been employed for conducting small-signal stability analysis. This tool utilizes numerical algorithms to establish the state matrix $\boldsymbol{A}$ and applies a standard QR method to compute its eigenvalues. The process involves expressing the matrix as the product of an orthogonal and an upper triangular matrix, multiply the factors in the reverse order, and iterate.

Given the size of the grid and number of synchronous generators, in this report, oscillatory modes with a damping ratio above 10% are considered properly damped and are excluded from the analysis. Oscillatory modes with a damping ratio below 5% are considered poorly damped and thoughtfully examined to check what type of flexibility options can enhance their stability and to what extent. Modes exhibiting a damping ratio in the 5 to 10% range are considered adequately stable. However, we meticulously analyse their behaviour to ensure that the implemented stability enhancements don't adversely affect them. It's crucial to maintain their stability while introducing broader improvements to the overall system stability.

For every forecasted scenario a base configuration is identified in which frequency support is provided only by conventional resources and stabilizers. The modal analysis is then performed for each dispatching profile identifying the critical oscillatory modes and repeated after “switching on” the frequency support provided by RES, assessing their contribution to the small-signal stability of the system.

5.2 Sicilian Network and Forecasted Scenarios Description

The analysis is based on a portion of Italy's transmission grid representing Sicily, as shown in Figure 25. Sicily is identified by the market zone *56IT*, Terna provided the model and the data, which has then been updated and customized for dynamic simulations. The DIgSILENT model provided includes generation plants, HV transmission grid and MV distribution grid. Sicily's grid configuration includes a limited number of lines with voltages at or above 220 kV.

Table 4. RES installed in Sicily (beginning of 2020) [75].

Technology	Total Installed [MW]	MV connected [%]	HV connected [%]
Wind	1887	6	94
Photovoltaic	1422	97	3
Hydro	274	4	96

Given its geographic size and significant generation capacity, the grid has a sparse mesh. Since 2016, Sicily has been connected to the Italian mainland through two 380 kV AC interconnections, both originating at the Rizziconi substation on the mainland and reaching the Sorgente substation on the island. The 380 kV transmission lines, marked in red in Figure 25, forms a single backbone stretching from the northeastern link to the Syracuse petrochemical area in the southeast, passing through major substations like Sorgente, Paternò, and Chiaramonte Gulfi, and reaching the ISAB plants near Priolo Gargallo. The primary transmission system comprises a large 230 kV ring along the coastal areas, depicted in green in Figure 25. At the beginning of 2020, the total installed RES capacity included about 1.9 GW of wind energy, mostly connected to the HV transmission network, about 1.4 GW of PV, mostly connected to the MV distribution network and almost 300 MW of hydropower.

Figure 25. The Sicilian high-voltage transmission network, in red the 380 kV transmission lines, in green the 220 kV transmission lines [76].

The modes of oscillations depend strongly on the strength of the network interconnecting the generation sources and, especially their frequency, by the distance between them. Figure 26 (a) displays the positions of the 23 synchronous generators in the Sicilian grid. Most of the units and also the largest ones are concentrated in the petrochemical complex of Augusta-Priolo located on the east coast of the Island, near Siracuse. Table 5 provides comprehensive details on their locations, rated power, and inertia constants. Figure 26 (b) illustrates the location of full converter wind turbine power plants, while Figure 26 (c) shows the locations of the DFIG Wind Farms. Figure 26 (d) combines these, depicting the locations of both DFIG and FCWT

Wind Farms along with synchronous generators and their substations. As the focus is on Electromechanical (EM) modes,

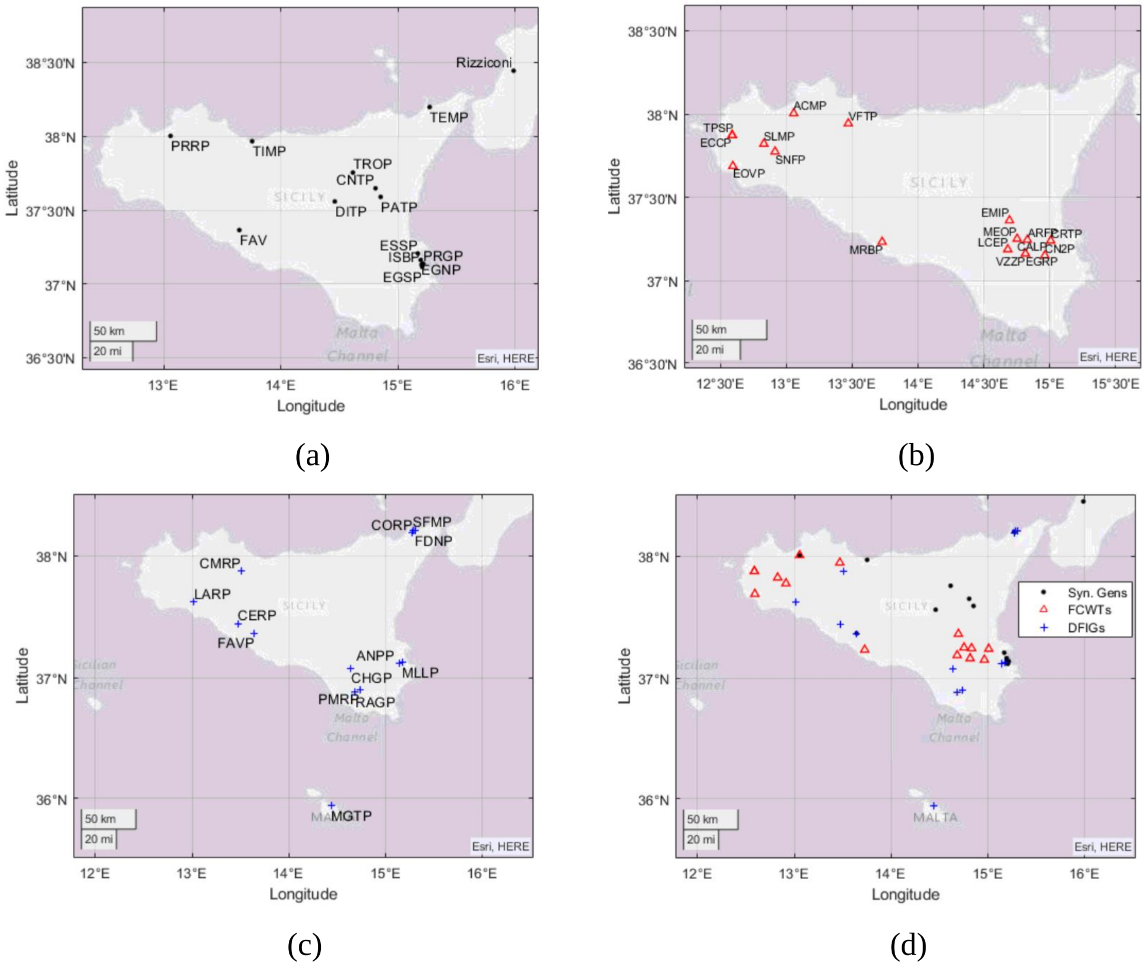

Figure 26. Locations of the (a) SGs, (b) FCWTs (c) DFIG WTs and (d) SGs, the FCWTs, and the DFIGs substations in the networks. The DFIGs are present only in the 2050 network. The slack generator is located on the peninsula in the substation of Rizziconi.

Table 5. Location and rating of the power plants in the Sicilian grid, for a total of 23 synchronous generators.

Location	No. of Units	Identification Name	Rating (MVA)	H (s)
Contrasto	1	CNTP	24	3.75
Dittaino	1	DITP	23	3.75
Priolo Gargallo	6	EGNP	576	3.75 – 6
Città Giardino	3	EGSP	90	3.75
Augusta	2	ESSP	80	3.75
Priolo Gargallo	2	ISBP	344	6
Paternò	1	PATP	9	3.75
Priolo Gargallo	2	PRGP	658	3.75
Milazzo	1	TEMP	185	3.75
Termini Imerese	3	TIMP	946	3.75 – 7.5
Troina	1	TROP	14	3.75

5.2.1 *Forecasted scenario: year 2030*

For the 2030 network scenario, compared to the 2015 grid model, the following key changes have been made:

- **Increased Power Rating of Mainland Links:** The power rating of links with the mainland has been increased to align with the projected 2030 Available Transfer Capacity (ATC), facilitating greater power transfer between Sicily and the mainland.
- **Equivalent Synchronous Machine:** An equivalent synchronous machine has been installed near the continental terminal of the Sicily-continental Italy link. This machine is designed to replicate the dynamic behavior of the Italian mainland's grid, with its power rated based on the active power of synchronous machines in other Italian market zones, adjusted by a power factor of 0.8, and a starting time constant of 10 seconds. This machine, equipped with a governor, automatic voltage regulator, and power system stabilizer, represents a portion of the continental units capable of providing primary frequency control.
- **Wind Farm Upgrades for Synthetic Inertia:** The existing 20 wind farms have been upgraded with a model capable of providing synthetic inertia, enhancing grid stability.
- **Modeling of High Voltage Photovoltaic Plants:** HV PV plants have been modeled, including their LV/MV transformers, and have been installed at MV busbars of 285 primary substations to simulate dispersed generation in distribution grids. These models include over frequency protections as per Italian standards.
- **Upgraded Generator Capacities:** The capacities of all generators in the grid have been upgraded based on provided data.

These changes are essential to accurately model the Sicilian grid for the 2030 scenario, taking into account the technological advancements and grid developments expected in the next decade. This modeling allows for a realistic assessment of the grid's performance and its capability to handle future energy demands and generation profiles.

Table 6. Installed capacity [MW] for 2030 for Sicily.

Zone	Battery	Biomass	PV	Hydro	Wind	Waste	Gas
56IT	0	99	2618	242	3820	781	2896

5.2.2 Forecasted scenario: year 2050

The major updates to the 2030 Sicilian grid for adapting to the 2050 scenario, include:

- **Increased Mainland Cable Capacity:** The power rating of the connection between Sicily and the mainland has been raised to 2300 MW.
- **Additional Wind Plants:** Alongside existing wind plants with IR controllers, 15 new wind plants capable of PFR have been added.
- **BESS Installations for Frequency Control:** Batteries capable of primary frequency control have been installed. These are placed near new wind plants or at sites with existing synchronous generators, with each site's battery capacity limited to 20% of the existing plant's capacity.
- **Controlled Loads for Frequency and Voltage Control:** Controlled loads are installed near 16 existing large loads (13 MW or larger), enhancing grid stability.
- **Expansion of the 220 kV Ring Circuit:** The 220 kV ring circuit on the island has been doubled to meet the projected demand.
- **Upgraded Generator Capacities:** All generators' capacities have been increased as per the data and approach from T1.1, consistent with the 2030 upgrades.
- **Updated Equivalent Synchronous Machine in Continental Italy:** The equivalent machine representing the Italian mainland's grid has been updated, with its rated power based on the active power of other Italian market zones' synchronous machines.

These changes reflect a significant enhancement in grid capacity, renewable energy integration, storage, and control mechanisms, preparing the Sicilian grid for the demands and technological advancements anticipated by 2050.

Table 7. Installed capacity [MW] for 2050 for Sicily.

Zone	Battery	PV	Hydro	Wind	Waste	Gas	P2G
56IT	1572	6075	313	6360	566	162	1947

5.2.3 Dispatching Profiles

Six dispatching profiles (DPs) encompassing the most common operating conditions of the Sicilian grid as well as some edge cases, have been identified by Monte Carlo simulation by RTE. For both the years 2030 and 2050, although characterized by a different mix of production and consumption, the dispatching profiles considered in the stability analysis of Sicily are:

1. *High Export*: characterized by an elevated PV production, low traditional generation, and high zonal export toward the rest of Italy.
2. *High Import*: characterized by almost no PV production and high load demand; such active power request is provided by rest of Italy.
3. *High Load*: characterized by high load demand; high PV, medium wind and low traditional generation.
4. *Low Load*: characterized by low load and low generation by thermal plants, dispatched at their minimum active power, and medium wind production.
5. *Island*: it is the *High Load* dispatching profile, with the link with the mainland out of service.
6. *Lines out of service*: it is the *Low Load* dispatching profile with the 230 kV Favara-Chiaramonte and Caracoli-Sorgente lines out of service.

5.3 Modal Analysis: Base Configuration

For the base case of each forecasted scenario, that is without any IR support from RES, the modal analysis is performed. The main oscillatory modes are identified by the associated eigenvalues and their frequency and damping ratio determined. By plotting the associated mode shapes, reporting the oscillation vectors of the rotor speed deviation of the units responsible for each mode, the main power plants involved are identified, and the relation between the generating units, i.e., whether they are oscillating in phase or counterphase is established.

5.3.1 Forecasted scenario: year 2030

For the 2030 base case forecasted scenario for the results for each dispatching profile are the following. As anticipated, in the base case the RES do not contribute to the IR of the grid, that is the gains of the relevant frequency controllers are set to 0.

A. “High Export” dispatching profile

For the *High Export* dispatching profile, the modal analysis showed 5 electromechanical modes with damping ratio below 10% as shown in Table 8. The modes are named in order of increasing damping ration, mode M1, that represents an interarea mode, is the only mode with a damping ratio below 5 % (i.e., 1 %), and it is does considered unstable.

Table 8. Electromechanical modes with damping ratio below 10% for the 2030 High Export dispatching profile.

Mode	Eigenvalues	Frequency, f (Hz)	Damping, ζ (%)	Involved Plants
M1	-0.07 ± 4.59j	0.73	1.48	TIMP, PRGP, SLACK
M2	-0.61 ± 8.18j	1.30	7.47	EGSP, PRGP
M3	-0.45 ± 5.58j	0.89	8.04	EGNP, PRGP, ISBP
M4	-0.88 ± 9.96j	1.58	8.84	EGSP
M5	-0.89 ± 9.95j	1.58	8.92	EGSP

By looking at the oscillation vectors of these modes, it is possible to identify their characteristics and the generators involved, these are shown in Figure 27 (a)-(e), and allow us to conclude that:

- M1 is an interarea mode, as its frequency suggests, in which the slack generator in Rizziconi oscillates against TIMP1, TIMP2 and the generator in Priolo Gargallo, named PRGP1. However, the participation factors of PRGP1 and of the slack are significantly lower. The generators mainly affected by this oscillatory mode are the generators of the thermoelectric plant in Termini Imerese, named TIMP1 and TIMP2. As the following analysis will show, this mode can be properly damped both by tuning the gain of the PSS in TIMP and by providing inertial response through the FCWT.
- M2 is a local mode in which the generators EGSP1, EGSP2 and EGSP3 oscillate against the generators PRGP1 and PRGP2 which do however have a very low participation factor in it.
- M3 is a local mode characterized by generators EGNP1 and EGNP2 oscillating against generators ISBP1 and PRGP1.
- M4 is an intraplant mode in which EGSP3 oscillates against EGSP1 and EGSP2.
- M5 is another intraplant mode of the same plant in which EGSP1 oscillates against EGSP2 and EGSP3.

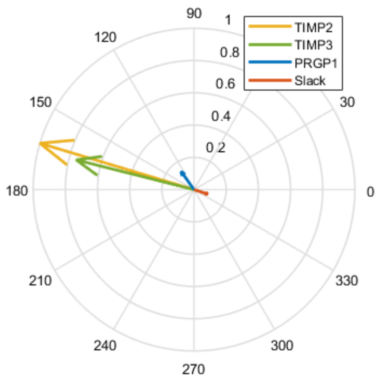

(a)

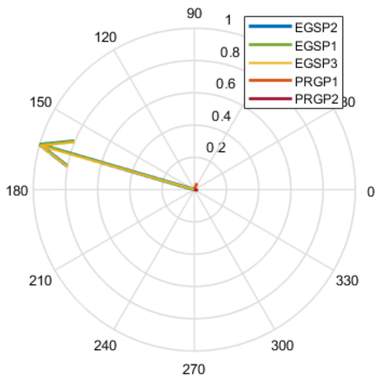

(b)

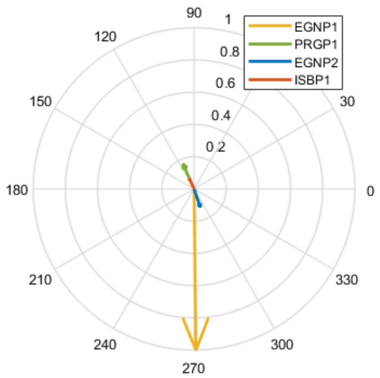

(c)

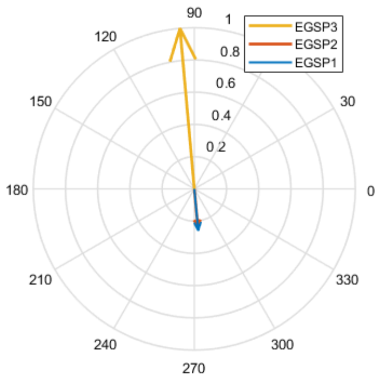

(d)

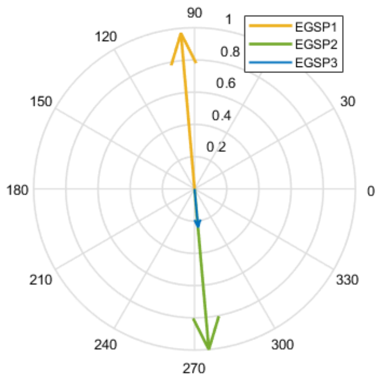

(e)

Figure 27. Oscillation vector of mode: (a) M1, (b) M2, (c) M3, (d) M4 and (e) M5.

B. “High Import” dispatching profile

For the *High Import* dispatching profile, the modal analysis revealed two electromechanical modes with a damping ratio below 10%, both properly damped and shown in Table 9. All the other modes are stable. The modes, M1 and M3, are the same already described in the previous profile. However, there is a considerable increase in the damping ratio of M1 and a slight decrease in frequency. The damping ratio of M1 is in this case above 5 % and the mode is hence well damped. Similarly, the damping ratio of M3 is slightly increased here, compared to the *High Export* profile and the frequency stays the same.

Table 9. Electromechanical modes with damping ratio below 10% for the 2030 High Import dispatching profile.

Mode	Eigenvalues	Frequency, $f\ (Hz)$	Damping, ζ (%)	Involved Plants
M1	-0.33 ± 4.25j	0.68	7.69	TIMPP, PRGP, SLACK
M3	-0.50 ± 5.56j	0.89	8.98	EGNP, PRGP, ISBP

C. “Low Load” dispatching profile

In the *Low Load* profile, the modal analysis showed 1 electromechanical mode with a damping ratio slightly below 10% as shown in Table 10:

Table 10. Electromechanical modes with damping ratio below 10% for the 2030 Low Load dispatching profile.

Mode	Eigenvalues	Frequency, $f\ (Hz)$	Damping, ζ (%)	Involved Plants
M6	-1.03 ± 10.8j	1.72	9.50	TROP, EGNP

This is an electromechanical mode that did not appear in the previous hourly profiles; hence it will be named sequentially (i.e., M6) and its dynamic behaviour is examined by means of the oscillation vector shown in Figure 28:

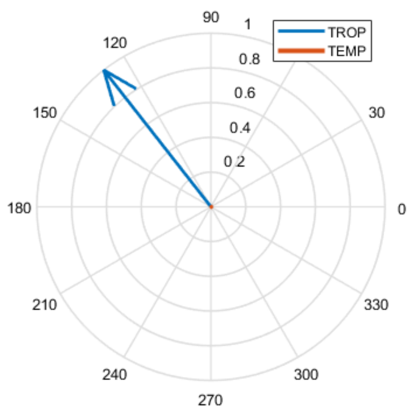

Figure 28. Oscillation vector of mode M6.

- M6 displays the unit in Troina (TROP) oscillating against the one in Milazzo (TEMP). Generator TROP, however, is not equipped with a PSS and has a rated power more than 10 times smaller than generator TEMP, which it is practically not affected by the oscillatory mode, hence justifying the big difference in participation factor magnitudes.

The remaining dispatching profiles, which include the *High Load* DP, the *Island* DP and the *Lines out of Service* DP do not present EM modes with a damping ratio below 10%. Hence, they can be regarded as of no small-signal stability concern.

5.3.2 *Forecasted scenario: year 2050*

Conversely, in the 2050 forecasted scenario the *High Export* DP, *High Load* DP and the *Island* DP do not present any oscillatory modes below the 10% threshold. The modal analysis of the DPs presenting EM modes with a damping ratio below 10% is discussed here after.

A. "High Import" dispatching profile

For the *High Import* dispatching profile, the modal analysis revealed five modes, four have been already encountered and examined in the 2030 network while mode M7, with a damping ratio very close to 10%, has not been discussed yet. The results are reported in Table 11.

Table 11. Electromechanical modes with damping ratio below 10% for the 2050 High Import dispatching profile.

Mode	Eigenvalues	Frequency, f (Hz)	Damping, ζ (%)	Involved Units/Plants
M1	-0.31 ± 4.83j	0.77	5.66	TIMP, PRGP, SLACK
M2	-0.59 ± 8.18j	1.30	7.24	EGSP, PRGP
M4	-0.88 ± 9.98j	1.59	8.83	EGSP
M5	-0.89 ± 9.97j	1.59	8.90	EGSP
M7	-1.04 ± 10.4j	1.66	9.89	DITP, ESSP, PRGP

The characteristics and the generators involved in M7, shown in Figure 29, are:

- M7 is a local mode in which generator in Dittaino (DITP) and the generator in Augusta (ESSP2) oscillate against the larger generator located in Priolo Gargallo, PRGP1.

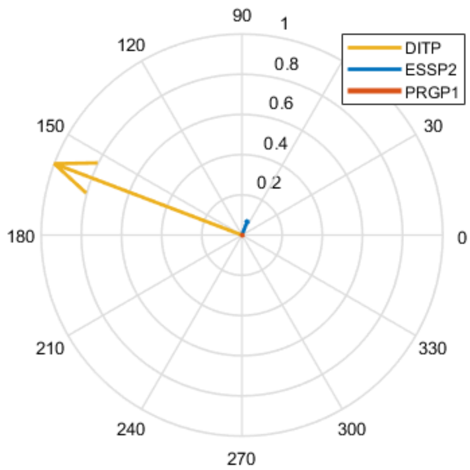

Figure 29. Oscillation vector of mode M7.

B. *“Low Load” dispatching profile*

In the *Low Load* dispatching profile, the modal analysis revealed 3 electromechanical modes with a damping ratio below 10% one of which, interarea mode M1, with an unacceptable value of 3.88%. The results are reported in Table 12. As it will be shown, the interarea mode can be properly damped either with the contribution of virtual inertia provided by RES (contribution of both FCWT and BESS) or by tuning the gain of the relevant PSS, or by a combination of both.

Table 12. Electromechanical modes with damping ratio below 10% for the 2050 Low Load dispatching profile.

Mode	Eigenvalues	Frequency, f (Hz)	Damping, ζ (%)	Involved Plants
M1	-0.19 ± 4.95j	0.79	3.88	TIMP, PRGP, SLACK
M8	-0.80 ± 10.86j	1.73	7.38	CNTP, PRGP
M9	-0.85 ± 11.09j	1.77	7.67	PATP, CNTP

The characteristics and the generators involved in M8 and M9, shown in Figure 30, are:

- M8: In this mode the generator in Contrasto (CNTP) oscillates against one of the units in Priolo Gargallo (PRGP1).
- M9: This mode involves the unit in Paternò (PATP) oscillating against the unit in Contrasto (CNTP).

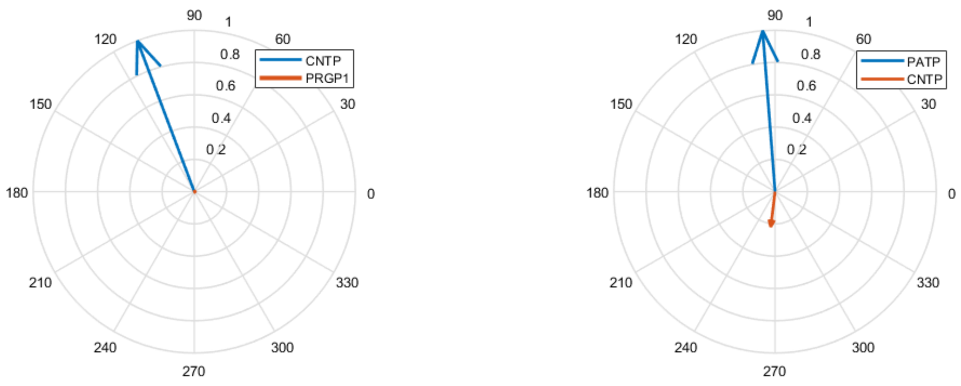

(a) (b)

Figure 30. Oscillation vector of mode (a) M8 and (b) M9.

C. “Lines out of Service” dispatching profile

In the *Line out of Service* dispatching profile, which is a variation of the *Low Load* one, the modal analysis presents the same modes. The results are presented in Table 13. In this dispatching profile two important 230 kV lines are out of service. For this reason, the damping ratio of mode M1 decreases from the value of 3.88% (*Low Load* dispatching profile) to a value of 1.78%. Mode M1 is particularly affected here because the line Caracoli-Sorgente basically connects the plant in Termini Imerese (TIMP) to the interconnection with continental Italy, right before the substation of Rizziconi on the mainland. Like for the *Low Load* dispatching profile, a combination of virtual inertia support schemes and PSS tuning it is going to be adopted to properly damp the critical interarea mode. Modes M8 and M9, maybe because of the location of the plants involved which are not connected by the lines out of service, are beneficially affected in this dispatching profile and their damping ratio is increased.

Table 13. Electromechanical modes with a damping ratio below 10% for the 2050 Lines out of Service dispatching profile.

Mode	Eigenvalues	Frequency, $f\ (Hz)$	Damping, ζ (%)	Involved Plants
M1	-0.08 ± 4.74j	0.75	1.78	TIMP, PRGP, SLACK
M8	-0.86 ± 10.82j	1.72	7.95	CNTP, PRGP
M9	-0.92 ± 11.05j	1.76	8.26	PATP, CNTP

5.4 Synthetic Inertia Contribution of RES to the Small-Signal Stability

In this section, the extent to which the IR contribution of RES improves the small perturbation stability of the network is evaluated for both forecasted scenarios. Regarding the year 2030 that is the coordinated IR provided by FCWT. For the year 2050, the IR contribution from BESSs is added to the mix. This is done through a sensitivity analysis, increasing gradually the gain of the controllers and performing a modal analysis at each step, and checking whether or not the impact on the damping factor of the EM modes was beneficial. The procedure is identical to that discussed in the coordinated inertial response analysis performed on the 2-Area 4-Generator benchmark test network. That is, to assess the impact of the wind turbines’ IR support control strategies on the small-signal stability of the network, the gains of the DC-link control strategy and of the RKC are increased in discrete steps of 2, ranging from a value of 0, corresponding to no IR support, to a value of 30. This is done for the two controls separately as well as for the coordinated IR control strategy, in which the two controls operate in conjunction. As of before, for the sake of conciseness, of the total number of tested values only 4 significant ones are reported, i.e., 0, 10, 20 and 30. Again, following a common procedure, to strengthen the findings of the modal analysis, some perturbations specifically targeted to excite the EM modes of interest are simulated, for brevity not all of them are reported.

5.4.1 Year 2030 scenario: coordinated SI response from FCWT

A. "High Export" dispatching profile

For the *High Export* DP of the year 2030, the results of the sensitivity analysis are reported in Table 14 for interarea mode M1 and for the two local modes of the Priolo-Gargallo petrochemical complex, M2 and M3. The two intra-plant modes of the EGSP plant, M4 and M5, involving generation units within the same plant, are not affected whatsoever by the increase of IR support from wind farms and are not shown in the results. The two local modes do not experience stabilization improvements by the IR contribution, whether if coordinated or considering the two contributions separately. On the contrary, their damping factor decreases steadily with the increase of IR support, although maintaining a value above 7% and are thus considered sufficiently stable. On the other hand, interarea mode M1, which both by frequency and damping factor represents the main stability concern, experiences a relevant increase in damping factor by the contribution of either IR support schemes and a slight beneficial frequency increase. In particular, the DC-link IR support appears to contribute the most, peaking at a value of damping factor of 7.33% for a value of 20 of the gain K_{DC}. Increasing the values of the gains does not contribute indefinitely to the small-signal stability.

Table 14. Influence of coordinated IR support on the modes of the *High Export* dispatching profile of 2030.

SI Support	(K_{RKC}, K_{DC})	M1		M2		M3	
		f (Hz)	ζ (%)	f (Hz)	ζ (%)	f (Hz)	ζ (%)
Base Case	(0, 0)	0.73	1.48	1.30	7.47	0.89	8.04
DC-link	(0,10)	0.73	6.75	1.31	7.20	0.89	7.65
	(0,20)	0.75	7.33	1.31	7.14	0.89	7.39
	(0,30)	0.76	6.47	1.31	7.12	0.89	7.28
RKC	(10, 0)	0.74	5.24	1.31	7.24	0.89	7.71
	(20,0)	0.75	5.30	1.31	7.18	0.89	7.53
	(30,0)	0.76	5.15	1.31	7.15	0.89	7.43
Coordinated	(10,10)	0.75	6.21	1.31	7.17	0.89	7.47
	(20, 20)	0.77	5.56	1.31	7.13	0.89	7.31
	(30,30)	0.77	4.93	1.31	7.11	0.89	7.25

To excite the unstable inter-area mode M1 and comparing the frequency response of the network with and without the support of the coordinated IR scheme, the loss of one of the three tie-line connecting Sicily to continental Italy 2 is simulated at $t = 1s$, as shown in Figure 31. In both cases, the frequency deviation is minimal, lower than 4 mHz, but in the *Base Case* the frequency continues to oscillate indefinitely while with IR support from wind power plants, with both gains equal to 20, it settles back to its nominal value after a few seconds.

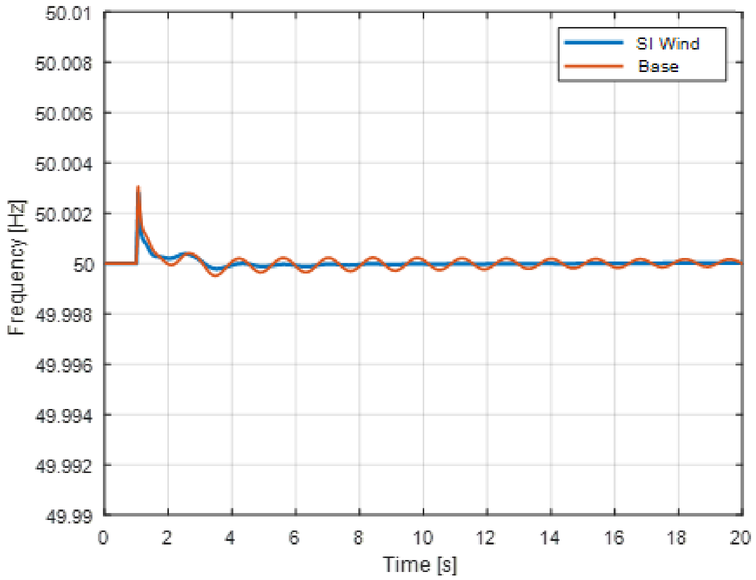

Figure 31. Outage of one of the three connections with continental Italy. Frequency profiles for the 2030 *High Export* DP.

Figure 32 shows the power exchanged through the three connections with continental Italy in the *Base Case*. The power exported by the lost connection, in red, is distributed to the two remaining connections, and in the *Base Case* keeps oscillating almost indefinitely. While with the IR support it stabilizes after a few seconds. In both cases, the currents remain below the rated value of 0.93 kA.

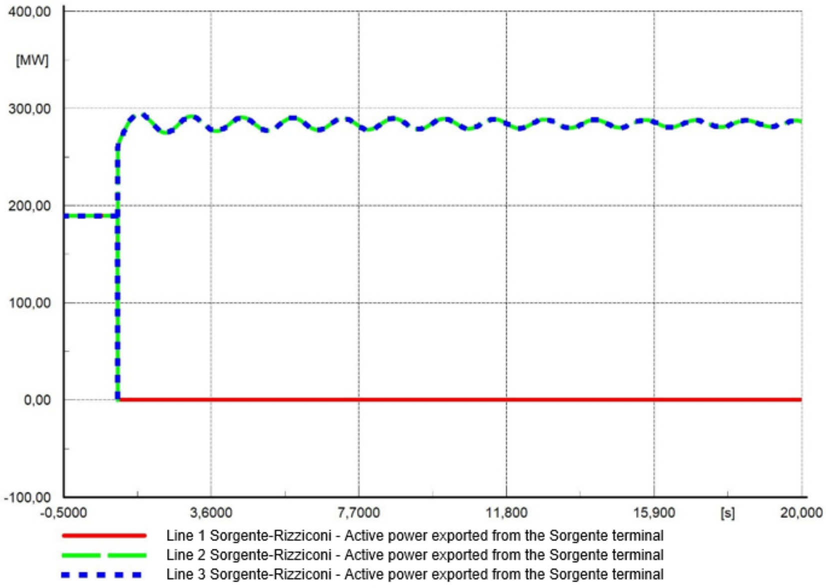

Figure 32. Outage of one of the three connections with continental Italy, base configuration. Power exported from the Sorgente terminal through the three connections with continental Italy. HE DP 2030.

The stabilizing effect of IR support is more clearly observable by simulating the loss of 2 of the 3 interconnections. This will be discussed, specifically for the HE DP in the next section, highlighting the different degree of contribution from DC-link, RKC and coordinated IR.

B. “High Import” dispatching profile

For the *High Import* DP of the year 2030, the results are reported in Table 15 for the two EM modes revealed in the base case, M1 and M3. Their behaviour is similar to the *High Export* DP, the local mode experiences a steady decrease in damping ratio with either IR support while maintaining the same frequency.

Table 15. Influence of coordinated IR support on the modes of the *High Import* dispatching profile of 2030.

SI Support	(K_{RKC}, K_{DC})	M1		M3	
		f (Hz)	ζ (%)	f (Hz)	ζ (%)
None	(0, 0)	0.68	7.69	0.89	8.98
DC-link	(0,10)	0.74	13.6	0.89	8.81
	(0,20)	0.74	13.6	0.89	8.62
	(0,30)	0.74	13.7	0.89	8.55
RKC	(10, 0)	0.74	13.6	0.89	8.83
	(20,0)	0.74	13.6	0.89	8.71
	(30,0)	0.74	13.6	0.89	8.64
Coordinated	(10,10)	0.74	13.6	0.89	8.67
	(20, 20)	0.74	13.6	0.89	8.56
	(30,30)	0.74	13.6	0.89	8.53

From a value of almost 9%, the damping factor decreases by about half a percent when the IR contribution peaks with either or both gains reaching the value of 30. On the contrary, thanks to IR support the frequency of interarea mode M1 goes from a value of 0.68 Hz to 0.74 Hz and its damping factor increases from an already sufficiently stable value of 7.69% to a most definitely stable value of 13.6%. The frequency deviation following the outage of one of the three interconnection line is shown in Figure 33, in these operating conditions the oscillations persevere for a shorter amount of time, with respect to the *High Export* DP, as the modal analysis suggests. The power exchange with continental Italy before and after the fault in the base configuration is shown in Figure 34, and it can be seen how the power oscillation perseveres for a much shorter amount of time with respect to the *High Export* DP. In accordance with the damping factor of the interarea mode being equal to 7.69% in one case and 1.48% in the other.

C. “Low Load” dispatching profile

Regarding the EM mode M6 in the *Low Load* DP, which involves a small hydropower unit without any PSS and a damping factor already close to the 10% threshold, the IR contribution does not affect by any means its eigenvalue. Conversely, regarding the *High Load*, *Low Load*, *Lines out of Service* and the *Island* dispatching profiles the same sensitivity analysis has been performed. With the various degrees of IR support no mode experiences a decrease in damping factor sufficient to taking it below the 10% stability threshold.

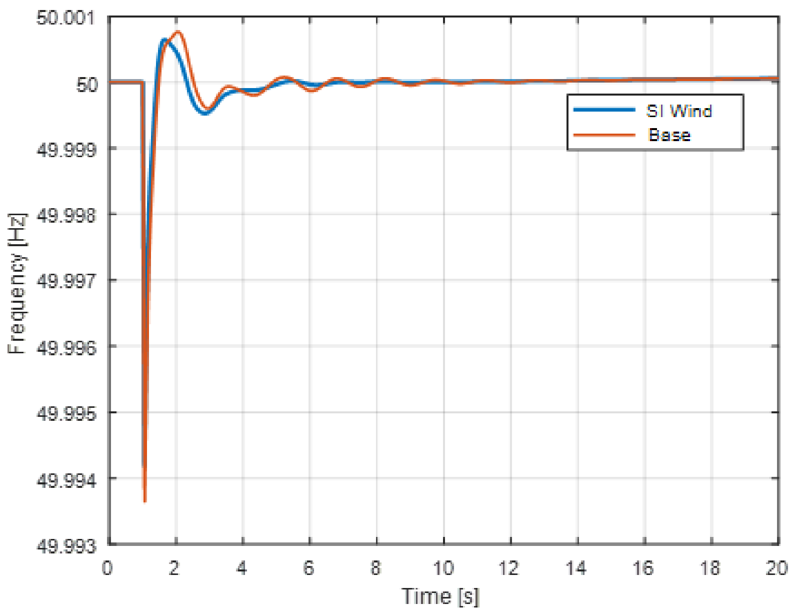

Figure 33. Outage of one of the three connections with continental Italy.
Frequency profiles for the 2030 *High Import* DP.

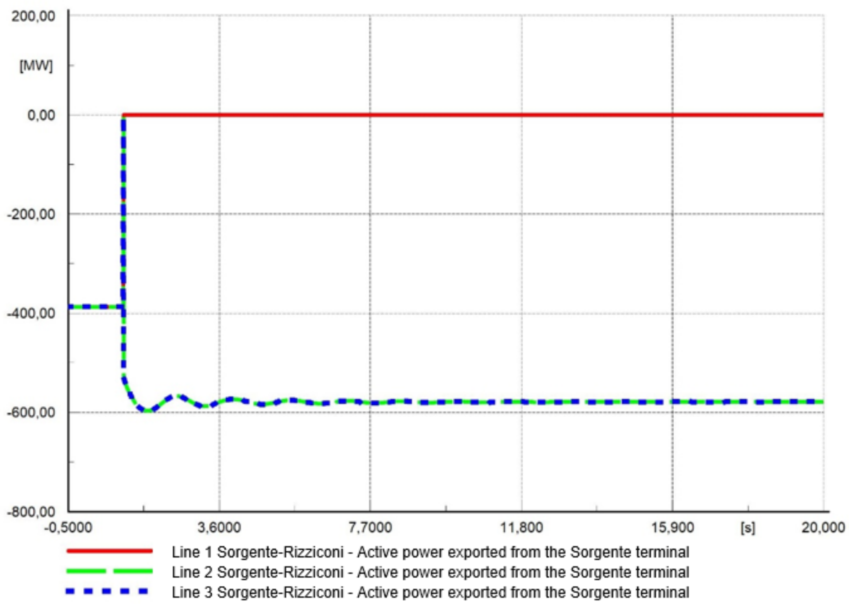

Figure 34. Outage of one of the three connections with continental Italy, base configuration. Power exported from the Sorgente terminal through the three connections with continental Italy. HI DP 2030.

5.4.2 *Outage of two interconnection lines in the 2030 "High Export" dispatching profile*

From an examination of the modal analysis results alone, one might infer that optimal damping in the 2030 *High Export* (HE) DP is achieved with the DC-link IR support alone, represented by the settings (K_{RKC}, K_{DC}) = (0,20). However, a comprehensive assessment of power system stability requires examining both frequency response and small-signal stability. As discussed in the previous chapter, the coordinated use of DC-link and RKC schemes enhances performance both in terms of maximum frequency deviation and initial RoCoF, compared to employing either scheme independently.

This section is dedicated to compare the dynamic performances of each IR scheme and their synergistic effects through time-domain simulations. For this, a non-linear dynamic simulation is conducted under the 2030 HE DP for Sicily. In this scenario, Sicily exports 574 MW to mainland Italy via three transmission lines. The simulation introduces a disturbance via the outage of two out of the three lines at 1 second, aimed at vigorously excite the inter-area mode M1. The analysis encompasses four scenarios: (a) without any IR support (K_{RKC}, K_{DC}) = (0, 0), (b) with only DC-link IR support (K_{RKC}, K_{DC}) = (0, 20), (c) with only RKC IR support (K_{RKC}, K_{DC}) = (20, 0), and (d) with coordinated IR support (K_{RKC}, K_{DC}) = (20, 20). Performance is gauged by the speed deviation of the generator with the highest participation factor in mode M1 and the power oscillations transmitted through the remaining interconnection.

In Figure 35 (a), the speed of the 'TIMPP 2' synchronous generator, in Termini Imerese, is depicted. The scenario without IR support shows the highest generator speed zenith, and the speed oscillations are not effectively damped. Introducing either IR scheme significantly improves damping of these oscillations and the best performance in terms of speed zenith is observed with coordinated control. Figure 35 (c) illustrates the active power output of the FCWT power plants. Without IR support, the wind farms maintain constant output during transients, not aiding in frequency stabilization. With IR schemes active, the WFs initially reduce output responding to the frequency increase in Sicily. This action helps damp the low-frequency oscillation of 'TIMPP 2', as the WFs adjust their output in contrast to the frequency variation in the Sicilian network. Figure 35 (d) and (e) display power flow through Lines 1 and 3 for each case. Following the disturbance, the power originally carried by the disconnected lines (Lines 1 and 2) is rerouted through Line 3. The consequent rise in generated power due to the disconnection momentarily increases Sicily's network frequency, which eventually returns to the nominal value, aided by the damping effects of the IR provisions.

In summary, coordinated control combining RKC and DC-link IR support is preferable to DC-link IR support alone. This approach yields superior frequency response outcomes while ensuring all EM modes' damping ratios remain above the 5% stability threshold.

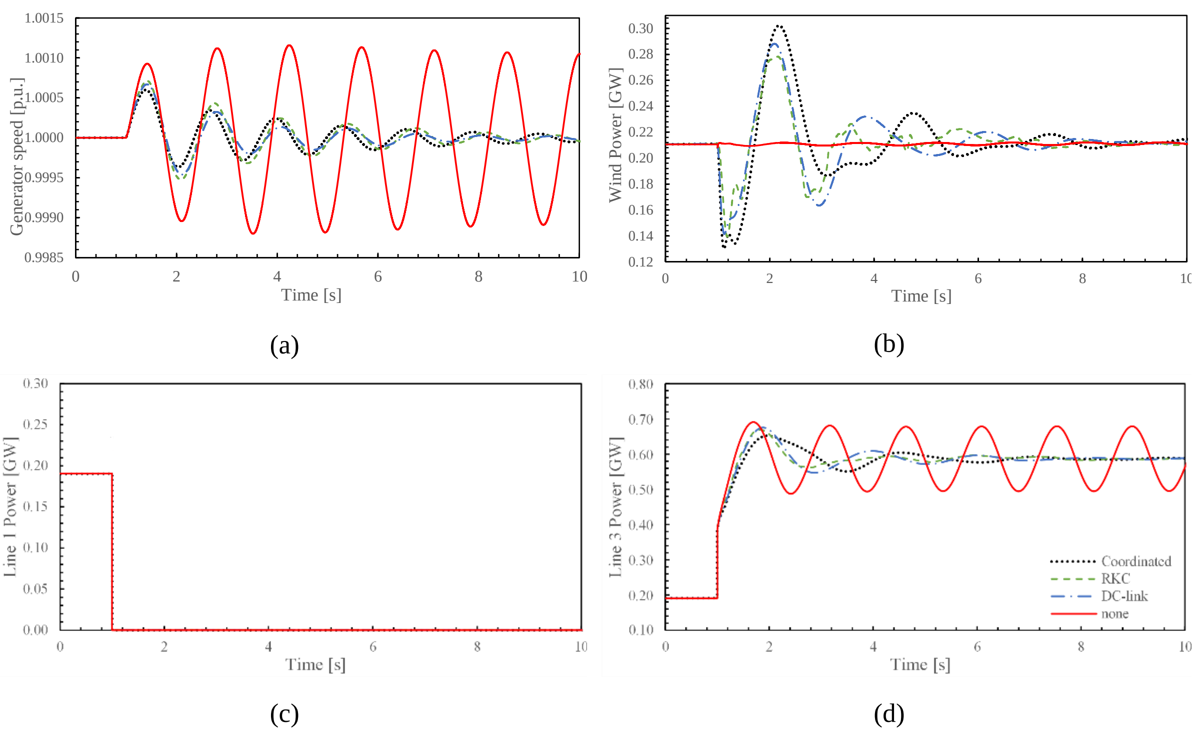

Figure 35. Outage of one of the three connections with mainland Italy at $t = 1s$ in the 2030 HE DP. (a) Rotor speed of the synchronous generator ‘TIMPP 2’, (b) total active power output from FCWT, (c) power transmitted through line 1 and (d) through line 3.

5.4.3 Year 2050 network: coordinated SI response from FCWT and BESS

In the 2050 scenario, both the individual and combined SI support from FCWTs and BESSs is examined. The modal analysis has been performed and repeated for different degrees of BESS SI support and FCWT SI support. That is, different combinations of the relevant gains, i.e., K_I, herein renamed K_{BESS} for clarity, and K_{RKC} and K_{DC}, are examined. For the 2050 HE, HL, and Island DPs, adjusting the gain values does not yield any mode with a damping ratio under 10%.

A. *"High Import" dispatching profile*

In the 2050 HI scenario, as outlined in Table 16, it can be noted that increasing the value of K_{DC} and/or K_{RKC} beyond zero positively affects the damping ratio of mode M1. However, modes M2 and M7 exhibit a slight decrease in their damping ratios with increased gains. Elevated K_{BESS} values have a marginal impact on M1, but significantly improve the damping ratios for M2 and M7, with M7 surpassing the 10% threshold. The aggregate effect of all SI gains markedly boosts the damping ratios for all EM modes.

Table 16. Influence of coordinated SI support on the modes of the *High Import* dispatching profile of 2050.

SI Support	(K_{BESS}, K_{RKC}, K_{DC})	M1		M2		M7	
		f (Hz)	ζ (%)	f (Hz)	ζ (%)	f (Hz)	ζ (%)
Base Case	(0, 0, 0)	0.77	5.66	1.30	7.22	1.66	9.89
DC-link	(0, 0,10)	0.77	8.21	1.31	7.04	1.67	9.62
	(0, 0, 20)	0.78	8.05	1.31	6.98	1.67	9.60
	(0, 0, 30)	0.78	7.97	1.31	6.96	1.67	9.59
RKC	(0, 10, 0)	0.77	7.48	1.31	7.05	1.66	9.43
	(0, 20, 0)	0.78	7.70	1.31	7.00	1.69	9.12
	(0, 30, 0)	0.78	7.61	1.31	6.98	1.69	9.00
BESS	(10, 0, 0)	0.77	6.42	1.30	7.88	1.66	10.2
	(20, 0, 0)	0.77	6.43	1.30	8.57	1.66	10.4
	(30, 0, 0)	0.77	6.44	1.30	9.27	1.67	10.7
Coordinated	(10, 10, 10)	0.78	7.97	1.30	7.66	1.67	9.89
	(20, 20, 20)	0.78	7.57	1.30	8.29	1.67	10.1
	(30, 30, 30)	0.79	7.19	1.30	8.98	1.67	10.3

B. *"Low Load" dispatching profile*

Regarding the 2050 LL scenario, as detailed in Table 17, the pattern is similar. increasing K_{DC} and/or K_{RKC} above zero raises the damping ratio of M1 above the 5% stability threshold, but the ratio lessens with higher gain settings. The damping ratio of M8 slightly decreases with increased gains. More substantial K_{BESS} values have a minor impact on M1's damping and no influence on M8 whatsoever. Overall, the combined SI contribution leads to a significant improvement on the damping ratio of M1.

Table 17. Influence of coordinated IR support on the modes of the *Low Load* dispatching profile of 2050.

SI Support	(K_{BESS}, K_{RKC}, K_{DC})	M1		M8	
		f (Hz)	ζ (%)	f (Hz)	ζ (%)
Base Case	(0, 0, 0)	0.79	3.88	1.73	7.38
DC-link	(0, 0,10)	0.79	5.77	1.73	7.26
	(0, 0, 20)	0.79	6.12	1.73	7.25
	(0, 0, 30)	0.80	6.11	1.73	7.24
RKC	(0, 10, 0)	0.79	5.35	1.73	7.32
	(0, 20, 0)	0.79	5.70	1.73	7.29
	(0, 30, 0)	0.80	5.76	1.73	7.27
BESS	(10, 0, 0)	0.79	4.66	1.73	7.38
	(20, 0, 0)	0.79	4.67	1.73	7.38
	(30, 0, 0)	0.79	4.67	1.73	7.38
Coordinated	(10, 10, 10)	0.79	5.97	1.73	7.25
	(20, 20, 20)	0.80	5.87	1.73	7.24
	(30, 30, 30)	0.80	5.64	1.73	7.24

C. “Lines out of Service” dispatching profile

For the 2050 LooS DP, presented in Table 18, increasing K_{DC} and K_{RKC} above zero significantly increases the initially small damping ratio of M1, pushing it over the 5% stability threshold. However, this ratio starts to reduce once the gains are high (for instance, with either the value of K_{RKC} or K_{DC} above 10. M8 experiences a small drop in damping ratio with higher gain values. Higher K_{BESS} values slightly bolster M1's damping but don't affect M7. The combined implementation of all SI contributions results in considerable enhancements in the damping ratio of M1.

Table 18. Influence of coordinated IR support on the modes of the *Lines out of Services* DP of 2050.

SI Support	(K_{BESS}, K_{RKC}, K_{DC})	M1		M8	
		f (Hz)	ζ (%)	f (Hz)	ζ (%)
Base Case	(0, 0, 0)	0.75	1.78	1.72	7.95
DC-link	(0, 0,10)	0.76	7.39	1.73	7.84
	(0, 0, 20)	0.79	6.09	1.73	7.83
	(0, 0, 30)	0.79	5.38	1.73	7.82
RKC	(0, 10, 0)	0.76	4.75	1.73	7.92
	(0, 20, 0)	0.78	5.34	1.73	7.88
	(0, 30, 0)	0.78	4.98	1.73	7.86
BESS	(10, 0, 0)	0.75	1.81	1.72	7.95
	(20, 0, 0)	0.75	1.83	1.72	7.95
	(30, 0, 0)	0.75	1.86	1.72	7.95
Coordinated	(10, 10, 10)	0.78	6.03	1.73	7.84
	(20, 20, 20)	0.79	5.22	1.73	7.83
	(30, 30, 30)	0.80	4.05	1.73	7.82

5.5 Conclusions

In this chapter, we examined the influence of wind power plants SI on the small-signal stability of the Sicilian power system, focusing on scenarios projected for 2030 and 2050. Our simulations on these models indicate that certain DPs exhibit significant stability issues in the absence of SI support. Specifically, the 2030 *High Export*, 2050 *Low Load,* and 2050 *Lines out of Service* DPs show an inadequately damped oscillatory mode under base conditions. This mode, which is inter-area and involves the equivalent generator in Calabria and a power plant near Termini Imerese, can be improved with SI support from WPPs. The 2030 High Import (HI) and 2050 HI DPs, in contrast, display EM modes with damping ratios between 5% and 10%, suggesting adequate damping. The other DPs analysed do not exhibit modes with damping ratios below 10%.

In general, we can observe that the most critical operating conditions happen when the island exchanges significant amount of power with the rest of the Italian peninsula, that is in the *High Export* or *High Import* dispatching profile. That is when the inter-area mode is strongly excited, and the interconnection it is the closest to transporting its rated power. This is when the SI support coming from wind power plants contributes the most to the power grid stability. The *Lines out of Service* profile represents a critical operating condition in which the network is severally weakened. The other operating conditions may present some local or intra-plant modes which are not strongly affected by SI support and are not of particular concern.

The SI support strategies studied include: (a) coordinated utilization of the DC-link SI control scheme and the RKC SI control scheme for the 2030 network; (b) a similar coordinated approach for the 2050 network, supplemented by SI provision from BESSs. While our focus is on full converter wind turbines, the approach can be adapted to any variable speed wind turbine. A sensitivity analysis regarding the SI gain and its impact on EM modes was conducted, demonstrating improved stability for poorly damped modes with SI contribution.

Key findings from the analysis include:

- The 2030 HE, 2050 LL, and 2050 LooS DPs show instability issues that can be mitigated with SI support, enhancing the network's small-signal stability.
- Unlike frequency response, where added inertia is typically beneficial, excessive inertia can negatively impact small-signal stability. While higher SI gains can enhance the damping of certain modes, they can also reduce the damping in others. For modes that benefit from SI support, overly high gain values can diminish their damping ratios. Thus, balancing frequency response and small-signal stability requires a careful selection of SI gains. The coordinated control of RKC, DC-link support schemes, and BESS SI can limit initial network frequency deviations and ensure all EM mode damping ratios meet the 5% threshold for small-signal stability.

In summary, the coordinated control approach proposed appears to effectively enhance generator speed damping following common network faults, striking a balance between initial frequency response and ongoing small-signal stability.

Chapter 6. Energy Management System of Renewable Energy Communities

This chapter delves into the essential aspects of energy communities and their Energy Management Systems (EMS), focusing on the insights gained from a pilot Renewable Energy Community (REC) established and monitored in the city of Bologna and enabled by the *IET climate-KIC* project Green Energy Community (GECO) [77]. Our aim is to present the key findings and validate the effectiveness of the proposed EMS.

This second part of the thesis examines the rigorous testing and validation of the EMS, a pivotal tool in enabling energy exchange among consumer and prosumers and fostering the development of versatile energy community. The approach includes a practical validation process, where the optimization models developed during the GECO project are put to the test. This is carried out both in a real-time digital simulation environment as well as in a Power Hardware-In-the-Loop (PHIL) configuration, where these models are compared against field data harvested from a distributed measurement systems installed at the Centro AgroAlimentare di Bologna (CAAB) as well as in the broader Pilastro-Roveri district of Bologna. This real-world application of our theoretical models is crucial in determining their effectiveness and applicability.

In the following sections, we will provide a comprehensive overview of this validation process. We will discuss the outcomes, challenges encountered, and the valuable insights gained through what could be considered as a proof of concept for future RECs. This is not only important from an academic standpoint but also in terms of its implications for the future of energy community models and their management systems.

The chapter is structured as follows: Section 6.1 outlines the 'Project GECO Framework', delving into the objectives of the Green Energy Community initiative in Bologna. Section 6.2, 'Distributed Measurement Systems using Smart Meters in Energy Communities', discusses the implementation of advanced metering infrastructure to monitor and manage energy usage. In Section 6.3, 'PV Generation and Load Demand Forecasts', the focus shifts to predicting solar power generation and energy consumption within the community. Section 6.4, 'EMS Algorithm for Optimal Scheduling of REC’s BESS', presents the strategies for efficiently scheduling the

Renewable Energy Community's Battery Energy Storage Systems using the Energy Management System algorithm. Finally, Section 6.5, 'Real-Time Test Bed for the Validation of the EMS', explores the practical application and testing of these energy management systems in a real-world environment.

6.1 Project GECO Framework

The GECO project in Bologna's Pilastro-Roveri district represents a crucial development in forming an energy community under Italy's adaptation of the EU Clean Energy Package (CEP). GECO's objective is to tackle social, technical, and economic challenges in creating a sustainable energy community. This includes goals like enhancing sustainability, addressing energy poverty, and promoting a low-carbon economy. The project plans to use a combination of renewable energy, storage systems, smart devices, optimization algorithms, and blockchain technology.

GECO is at the forefront of developing and testing advanced smart solutions aimed at increasing self-consumption of energy, enhancing energy storage, and making the best use of local resources. This includes setting up systems for real-time monitoring, predictive analytics, and automated controls to increase energy flexibility. The project is expected to provide valuable insights for integrating CEP principles into the Italian legal context.

The GECO project is a collaborative endeavor involving key players such as AESS, ENEA, UNIBO, CAAB/FICO, and the Pilastro Development Agency, with substantial support from regional and local entities like the Emilia Romagna Region, GSE, RSE, the City of Bologna, and various local groups, businesses, and residents. Financial support from EIT Climate-KIC underscores the project's importance and its potential to make a significant impact [78].

Figure 36. The Pilastro-Roveri district in the metropolitan area of bologna, site of the pilot project GECO.

6.2 Distributed Measurement Systems using Smart Meters in Energy Communities

In the area of RECs, the installation of smart meters (SMs) enables to monitor energy flows within the members of the REC and with the grid. By keeping a detailed track of generation and consumption patterns, smart meters facilitate a multitude of strategic advantages. This section describes the devices, the measurement campaign and how this distributed measurement systems contribute significantly to the operational efficiency and sustainability of RECs. Ultimately enabling the development of reliable load forecast methods which are instrumental for the EMS and can serve as a benchmark for future RECs that might not enjoy the advantages of a distributed measurement network.

The use of a network of smart meters to monitor the generation and consumption of the REC members allows the creation of a set of historical data which lead to several advantages such as:

1. **Consumer Awareness and Energy Optimization**: Smart meters provide consumers with real-time data on their energy usage. This awareness enables consumers to modify their consumption patterns, either by reducing overall energy usage or by shifting their consumption to periods when electricity prices are lower. Additionally, this can also encourage consumers to use energy when it contributes positively to the community's shared energy pool.
2. **Enhancing Prosumer Contribution:** For prosumers, smart meters are instrumental in optimizing the amount of self-consumed energy. By providing detailed insights into production and consumption, these meters enable prosumers to adjust their energy usage or production, maximizing their contribution to the REC.
3. **Asset Integration and Technical-Economic Assessment**: The integration of new assets like renewable energy plants and storage systems can be more effectively managed with the data from smart meters. These devices help in accurately estimating the impact of such integrations on shared energy and self-consumption, facilitating better technical-economic assessments.
4. **Load Forecasting for Scheduling Algorithms:** Smart meters play a crucial role in short-term load forecasting. This is essential for developing efficient scheduling

algorithms that can dynamically manage the energy flow within the community, ensuring optimal usage and distribution of energy resources.

It is worth stressing that the last point has been instrumental in developing a reliable load forecast method which ultimately enables the EMS to make reasonable prediction based on which it determines how the REC's BESS asset needs to be operated.

The main advantage in the use of smart meters which are smart in the sense that the measurements acquisition process is automatic, and no human intervention is needed. As we will see the devices are connected online and the measurements are uploaded in real-time onto a cloud database from which they can either be used right away or stored for future and further processing. In our study, two types of smart meter technologies have been deployed and analyzed:

1. **Non-Intrusive Load Monitoring (NILM):** This device allows for the disaggregation of total energy consumption data into appliance-specific usage without requiring individual appliance meters. NILM provides detailed insights into the consumption patterns of different appliances, enabling more targeted energy-saving strategies.
2. **User Device (UD):** These meters are directly associated with individual users or devices, providing granular data on specific consumption or generation points. This allows for a more personalized understanding and management of energy usage.

These smart meters have been installed in diverse settings to gauge and test their effectiveness:

1. **Centro AgroAlimentare di Bologna (CAAB):** At CAAB, smart meters have been installed across various offices and warehouses, including roof-top PV and specialized environments like cold rooms. This has enabled a comprehensive analysis of energy patterns in a commercial and industrial setting.
2. **Pilastro-Roveri District Residences:** In the residential context, these meters have been installed in several Households. This provides insights into household energy consumption and generation, offering a complementary perspective to the commercial settings at CAAB.

6.2.1 Non-Intrusive Load Monitoring devices

Non-Intrusive Load Monitoring (NILM) devices are designed to accurately measure both power consumption and production, along with the associated energy levels. Depending on the power capacity of the installation, two types of NILM meters have been employed:

1. **Passthrough Meters:** Ideal for smaller power applications, these meters are connected in series with the power cables, accommodating cable cross sections of up to 35 mm². They directly measure currents and voltages from the power cable, providing precise readings for lower power scenarios. Provided by Regalgrid this is shown in Figure 37a.
2. **Current Transformer (CT) Meters:** For larger cable cross sections, CT type meters are more appropriate. In this setup, currents are measured using amperometric clamps, the ends of which are connected to the meter. A critical aspect of using CT meters is setting the correct transformation ratio in the meter's settings, which corresponds to the clamps used. Clamps with varying ratios are available, allowing the same meter to accommodate different maximum currents. Additionally, these meters require voltage references to be provided for accurate measurements. Shown in Figure 37b.

It’s important to note that the NILM meters installed are specifically designed for low voltage electrical systems. Their strategic deployment in energy monitoring systems allows to track and manage energy usage in a detailed and non-intrusive manner.

a)

b)

Figure 37. a) Regalgrid NILM device, b) Passthrough current transformer meter

The NILM devices continuously monitor electrical parameters, but the data are transmitted over the LAN/Internet only at every predefined time-step Δt, which can be as frequent as every 5 seconds. This level of time resolution is highly effective in tracking rapid variations in load and production profiles, ensuring that changes are accurately captured and analysed in near real-time. In Figure 38 an example of active power measurements obtained by NILM devices is shown.

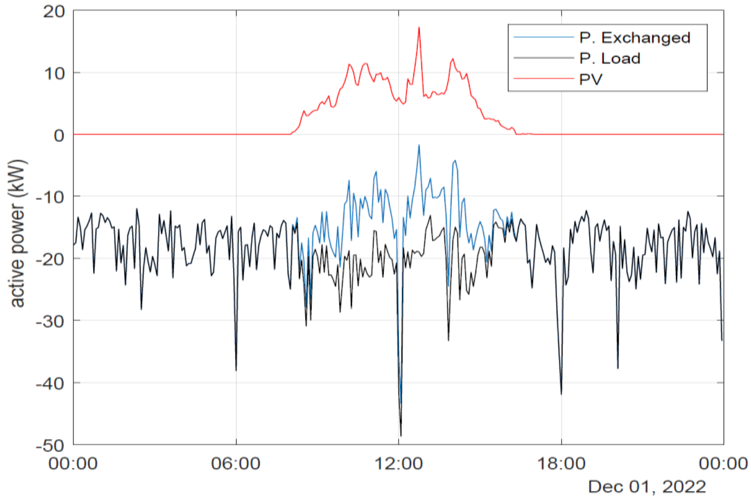

Figure 38. Example of a day of active power profiles measurements obtained via NILM devices.

In Table 19 the location, the type of loads and PV installation monitored via NILM at CAAB is reported.

Table 19. NILM-customers pairing installation.

Device ID	User	Description
348	Muda	Prosumer with a 94 kW PV plant.
335	Moden	Consumer, the main load is constituted by forklifts charging stations.
519	Deluca	Consumer with cold storage.
2080	Befer	Consumer with cold storage; contractual power: 82kW
2517	Agribologna	Consumer, the main loads are constituted by PCs, head pump/climatization, servers and instrumentation for fruit and vegetables quality analysis; contractual power: 50 kW.

6.2.2 User Device

A User Device (UD) is a monitoring instrument that communicates with the second-generation meters installed by Distribution System Operators (DSO) at users' premises. By the end of 2024, all DSO meters in Italy are expected to be upgraded to these new models. Unlike traditional meters, UD smart meters do not directly measure power or energy production and consumption. Instead, they acquire measurements from the DSO's fiscal meter through the Power Line Communication (PLC) Chain 2 interface, as shown in Figure 39.

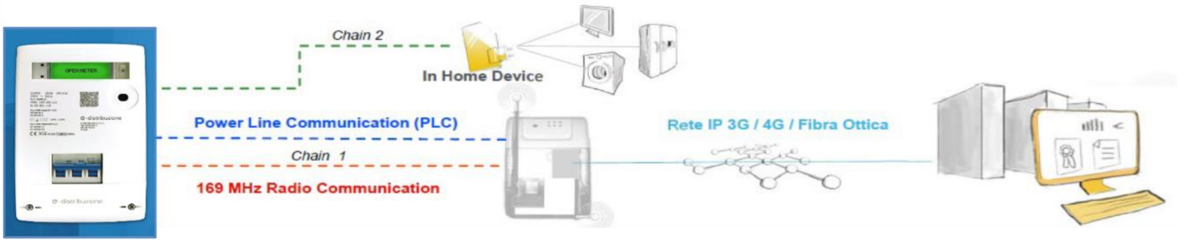

Figure 39. Second-generation DSO meter on the left, User device in the centre and cloud storage on the right (Adapted from [79]).

The PLC system operates by injecting a signal into the electrical network at a frequency within the C-band (125 kHz – 140 kHz), which is distinct from the standard 50 Hz power frequency. This setup establishes a communication link between the fiscal meter and the UD. To facilitate this interaction, smart meters require preliminary configuration by the manufacturer: a specific meter, identified by its serial number, is linked to a specific customer, identified by their POD (Point of Delivery), through the Distribution System Operator's (DSO) website designed for configuring PLC-chain2 communication.

The communication path from the fiscal meters to the UDs is inherently secure. This is because the two devices are paired using a secure set of cryptographic keys. Such a setup ensures that external entities with malicious intent cannot fabricate and inject messages into the UD. Furthermore, the communication link from the user device to the producer's gateway is safeguarded through encryption, using a public-private key pair. This means all messages are not only signed by the user device, verifying their origin, but can also only be decrypted and read by the intended recipient.

For effective communication, the UD must be connected to an electrical socket to receive data from the DSO's meters. However, this communication can experience interruptions or inconsistencies if the socket is located too far from the fiscal meter or if there are electrical disturbances in the system.

The time resolution of the measurements taken by the UD is limited by the information sent from the DSO’s meter via PLC. There are two types of data transmitted from the fiscal meter:

1. **Synchronous Data:** Sent every 15 minutes, detailing the energy consumed or produced during that period. This data can be used to calculate the average power over the 15-minute interval.
2. **Asynchronous Data:** Sent whenever there is a variation in power of ±10% relative to the contractual power, providing a measure of the instantaneous power value. Another

instance of asynchronous data it is sent when consumption exceeds the maximum threshold, indicating that the system may need to be disconnected.

One challenge encountered during the experimentation phase is the variability in data formats provided by different manufacturers. This necessitates the development of adaptive interfaces for each device type, which increases the risk of errors and confusion.

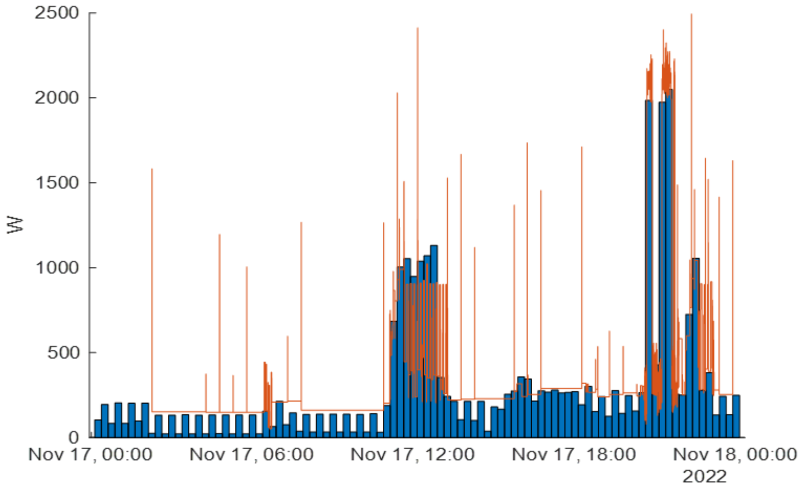

Figure 40. Example of active power measured by a UD and consumed during a day by a residential consumer. In blue, the synchronous data received every 15 minutes while in red the asynchronous data representing power spikes.

In Figure 40, the average power, obtained from the energy measurements received every 15 minutes, is represented by blue bars. In red, the power spikes of ±10% obtained as asynchronous data are fitted assuming that the power remains approximately constant to the last received value until a new measurement is received. It is noteworthy that the time resolution of these data varies: there are periods, sometimes extending several hours, where no data is received if the power profile remains relatively stable without significant variations. Conversely, data are more frequently received during periods of load peaks. A comparison between the average power profile and the interpolated instantaneous values reveals an interesting aspect: sporadic power peaks, which might be brief (lasting even less than a second), tend to be overlooked in the averaged data (blue). Consequently, these brief spikes do not significantly contribute to the overall energy consumption and the asynchronous data of UDs has been neglected.

Two types of UDs, supplied by two different providers, Tera and Urmet have been installed. Tera's UDs have been used for commercial installations at CAAB while Urmet's UDs have been installed at households in the Pilastro-Roveri district. For obvious privacy reasons the device IDs are renamed, and the apartments have been anonymized considering part of the device ID as an identifier of the apartment itself. In Table 20 the pairing between Tera and Urmet's UDs and monitored user is shown.

Table 20. Tera and Urmet UD pairing.

UD Provider	Device ID	User	Description
Tera	1115	CAAB	Prosumer with a 96 kW PV plant; the relevant loads are constituted by the PCs, Information Technology (IT) apparatus and motorized entrance bar
Tera	1098	Agribologna	Consumer, the main loads are constituted by PCs, head pump/climatization, servers and instrumentation for fruit and vegetables quality analysis; contractual power: 50 kW.
Tera	1058	Cenerini	Consumer, the relevant loads are the cold storage; also, office apparatus are present i.e. PCs, heat pump/climatization
Urmet	0001	Household 1	Residential
Urmet	0003	Household 3	Residential
Urmet	0004	Household 4	Residential
Urmet	0005	Household 5	Residential
Urmet	0006	Household 6	Residential
Urmet	0007	Household 7	Residential
Urmet	0009	Household 9	Residential
Urmet	000B	Household B	Residential

6.2.3 Online database platform

One of the main aspects to be considered for the successful implementation of an automatic EMS is the set of historical power and energy data necessary to generate load forecasts in the optimization algorithms. The set of historical data has been built and it is continuously updated using the measurements performed by the smart meters which have been installed in the GECO area. To efficiently manage this continuous stream of data, an online database has been set up. This database, designed for remote access, serves as a central repository for all the power and energy measurements, ensuring that the data is both securely stored and readily available for analysis and use in the EMS.

For the implementation of our database, we utilized Emoncms, an open-source web application designed for logging, processing, and visualization of energy data. Emoncms offers two usage options: it can either be downloaded and installed on a local device, such as a computer, or accessed via a subscription to its online version. The subscription cost varies based on the number of inputs stored [80]. Compatible with various operating systems including Linux Debian/Ubuntu, Windows, and Raspberry Pi, we opted for the downloadable version to gain full control over administration settings. The installation was carried out on a Virtual Machine (VM) running Ubuntu 20.04 LTS, hosted within a Virtual Private Network (VPN) on the University of Bologna's servers.

Several components are required for Emoncms to function effectively within the VM:

1. PHP, as a hypertext preprocessor,
2. MySQL or MariaDB, serving as the Relational Database Management System,
3. Apache, as the HTTP server,
4. Redis, to minimize disk write operations.

To protect the VM and the stored data, access to the VPN is secured through an OpenVPN certificate, assigning a specific Internet Protocol (IP) address to each device [81]. Each device connecting to the VPN requires a unique certificate, as simultaneous connections from multiple devices using the same certificate are not permitted. Each certificate is allocated to an individual responsible for its usage.

Access to Emoncms' Graphical User Interface (GUI) is achieved via the database's URL (in our case, the IP address of the VM within the VPN) in a web browser. Login credentials enable the administrator to manage the set of inputs from the community. The system's design allows for the registration of multiple administrators, facilitating the management and storage of data from various communities using the same hardware infrastructure.

Data in the database can be accessed or updated through an Application Programming Interface (API). The database is structured into two primary sections for data logging: "inputs" and "feeds":

- **Inputs Tab:** This section lists all the nodes within the database and their respective inputs. A node, identified either by an integer or a word, represents a set of inputs (e.g., measurements related to a meter or a consumer/prosumer). Each node has multiple associated inputs, such as power consumption, power production, voltage, current from loads and PV, as well as the power and State of Charge (SOC) of the BES. The inputs panel displays the most recent value received for each input alongside the time elapsed since the last update. It is important to note that the inputs tab does not store data; it only maintains the latest received value. To store data long-term, a feed must be created.

- **Feeds Tab:** This section displays a list of all created feeds within the database. Users can create new feeds or modify existing ones from this tab. Feeds are crucial for logging data, as well as for conducting mathematical and conditional operations on the inputs. Multiple feeds can be created for each input. For example, for a "power" input, one might be interested in storing both its instantaneous value and its cumulative total (energy). Therefore, one would create a logging feed for the power measurements and a power-to-kWh feed for the energy data. Each feed's entry shows the amount of memory used, the last value recorded, and the time elapsed since the last update.

In addition to the standard feeds, "virtual feeds" can also be created. These allow for mathematical or logical operations using data from one or more conventional feeds. The key advantage of virtual feeds is that they do not consume storage memory, as they utilize existing data from traditional feeds.

The NILM and UD smart meters installed, sourced from various manufacturers, are designed to facilitate data collection through API requests. However, each manufacturer's smart meter employs a unique HTTP request structure, which differs from the format used by the database. To address this challenge, scripts have been developed to streamline the data integration process. These scripts execute HTTP requests to the meters, reformat the data into a structure compatible with the database, and then initiate another HTTP request to log the measurements in the database.

To allow the efficient collection of data from the smart meters to the database, the NILM and UD installed, supplied by different manufacturers, are designed to facilitate this process through API requests. Each manufacturer's smart meter, however, employs a unique HTTP request structure, which differs from the format used by the database. To effectively manage this discrepancy, scripts have been developed to bridge the gap between the meters and the database. These scripts execute HTTP requests to the meters, reformat the data into a structure compatible with the database, and then initiate another HTTP request to log the measurements in the database.

The measurement campaign, started in 2022, has collected a significant historical dataset. This rich data pool has proved instrumental in the simulation of real-world scenarios, the implementation of load forecast methods and in the energy optimization usage within this community.

6.3 PV Generation and Load Demand Forecasts

In RECs, forecasting encompasses two key aspects: accurately predicting consumer’s load demand as well as assessing prosumer PV generation. While distinct, these forecasting tasks are essential inputs for the EMS. Although not the sole determinant of success, short-term forecasting (spanning a few days to a week) holds paramount importance in fine-tuning the REC's power management for optimal performance.

The significance of these forecasts lies in their role as inputs for the EMS. Without accurate load and PV generation forecasts, the EMS lacks the essential information needed to calculate and optimize battery power set-points effectively. This not only influences the stability and reliability of the energy supply within the REC but also directly impacts the economic and environmental benefits derived from the community's energy management. In essence, these forecasts aren't just pieces of information; they are integral elements that empower the REC's EMS to make informed decisions, ensuring the efficient utilization of the BESS and overall enhancement of the community's economic and energy sustainability.

6.3.1 PV generation forecast

Ideally, forecasting PV production solely based on historical data, whether sourced from historical datasets of a certain region or from the PV system's past production itself, would be optimal. To do so, without the need to resort to an online API service a simplified clear sky irradiation model has been implemented. However, the inherent randomness of cloudiness in weather patterns complicates this task, especially for short-term forecasting. The inherent unpredictability of weather conditions makes it nearly unavoidable to rely on advanced real-time online tools, such as satellite-enhanced weather forecasting services. Relying on real-time and comprehensive weather data becomes crucial to supplement historical information and enhance the accuracy of short-term PV production forecasts, ensuring a more reliable basis for the EMS decision making process within the REC.

In exploring solutions for accurate solar forecasting, various online tools have been evaluated, each offering basic functionalities at no cost and enhanced capabilities through paid subscriptions. One of these is ForecastSolar, which provides an API tailored for PV installations and integrates historical irradiation data from PVGIS with past weather data and forecasts from sources like Dark Sky, Wunderground, and OpenWeatherMap [82]. The free version of ForecastSolar offers solar production and weather forecast data with an hourly resolution for a 7-day period, focusing on the immediate day and the next. However, this basic service is limited in the number of API calls per hour and the depth of the time horizon forecast, unlike its subscription counterpart.

Users can utilize ForecastSolar to calculate estimated solar production for specific locations, determined by latitude and longitude, and particular plane orientations, specified by declination and azimuth, factoring in the installed power. ForecastSolar updates its forecast profiles every 15 minutes. For practical application, the API is accessed at a frequency of $T_{forecast}$ to align with real-time needs. In Figure 41, an example the evolution of the PV production forecast, updated every $T_{forecast}$, starting from midnight onwards compared with the real PV production measured at the end of the day is shown. At the beginning of the day, it appears that the day would be cloudy and production low, as the hours pass by the production forecast increases until reaching a good approximation of what it will be measured at the end of the day. It is worth noting that the rapid fluctuations of the PV production, whether caused by varying cloud coverage or measurement error, cannot be captured by the forecast service.

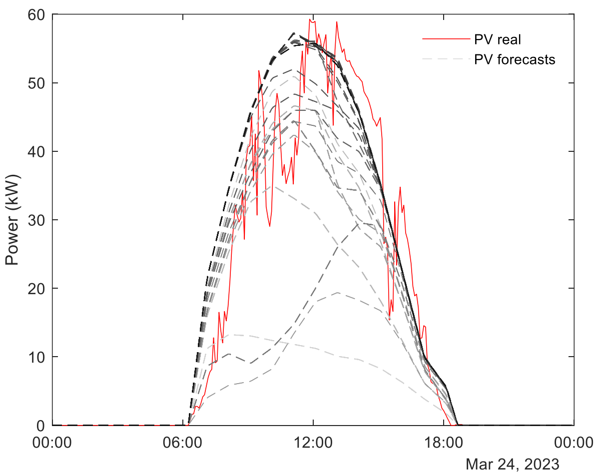

Figure 41. Evolution of the PV production forecast, updated every hour, starting from midnight onwards compared with the real PV production measured at the end of the day. March 24th, 2023, MUDA PV plant, NILM ID 348.

While historical information remains valuable for a comprehensive analysis of community behavior, it is essential to highlight the role of short-term forecasting and live weather data. In this context, the uncertainty of forecasts increases as the time window horizon increases. For more detailed historical analysis, Solcast steps in as a complementary tool, offering a spectrum of data, including forecast, live, and historical solar irradiance, PV power, and weather data [83]. Leveraging satellite and numerical weather models, Solcast extends its services from the current moment up to 14 days ahead. The crucial aspect lies in recognizing the importance of live weather data in achieving accurate short-term solar forecasting. In Figure 42 a graphical example of historic and forecast given by Solcast for the location of GECO in December 2022. It can be noted how a day with a relative clear sky, December 12th, lies in between two heavily cloudy days whit significantly lower PV production marking the importance of live weather forecast and the unfeasibility of relying only on historical datasets.

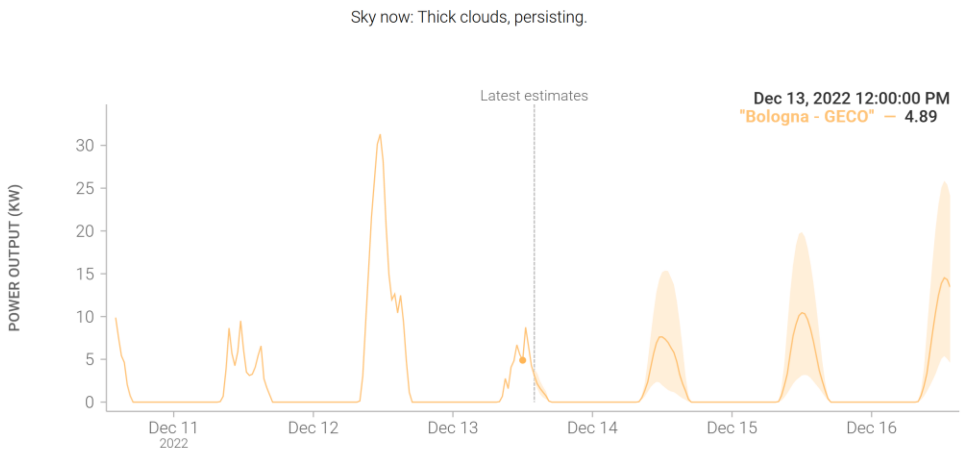

Figure 42. Graphical example of historic and forecast data obtained from Solcast (Adapted from [83]).

6.3.2 Load demand forecast

As important as PV production forecast, accurate load prediction stands as a significant challenge within the EMS of RECs. Thus, the adoption of a precise load forecasting method becomes essential for optimizing power management within the REC, leading to economic benefits for community members [84]. Short-term load forecasting in the REC proves more intricate compared to larger-scale power grids. Load consumption forecasting at grid-scale is considered more manageable compared to the REC scale due to several factors. First, the sheer number of consumers within the grid provides a larger dataset, allowing for more reliable statistical averaging and modelling. This abundance of data helps smooth out individual variations, making the overall load prediction more stable.

In contrast, at the REC scale, the number of consumers is typically smaller, leading to a less extensive dataset. This reduced data volume makes load forecasting more susceptible to the specific behaviors of individual residents within the community. Variability in energy consumption patterns among a smaller group can introduce more unpredictability, adding complexity to the forecasting process. Therefore, forecasting load consumption within a REC context requires a more nuanced approach that considers the unique characteristics and behaviors of the community members.

Through an examination of the historical data collected during the year and stored in the online database, it is observed that energy consumption by monitored customers remains consistent during working days, Monday to Friday. In contrast, both holidays (Sunday) and pre-holidays (Saturday) exhibit distinctive consumption patterns, setting them apart from each other and from typical working days. In Figure 43 and Figure 44, three weeks of energy consumption (in kWh) are shown respectively for a cold room, used to keep large amounts of vegetable refrigerated, and a standard office with indoor lighting, computers, printers and so on. The first day of the bar plot, May 14th, is a Saturday, the second day a Sunday and days from the 15th to the 20th are working days. Then the pattern repeats, and it is easy to identify cluster of working days, Saturday, and Sundays. An anomaly appears the 2nd of June, a Thursday, the load consumption is significantly smaller than the previous and following working day and comparable to a Sunday. This is because June the 2nd is Day of the Republic in Italy, a national holiday.

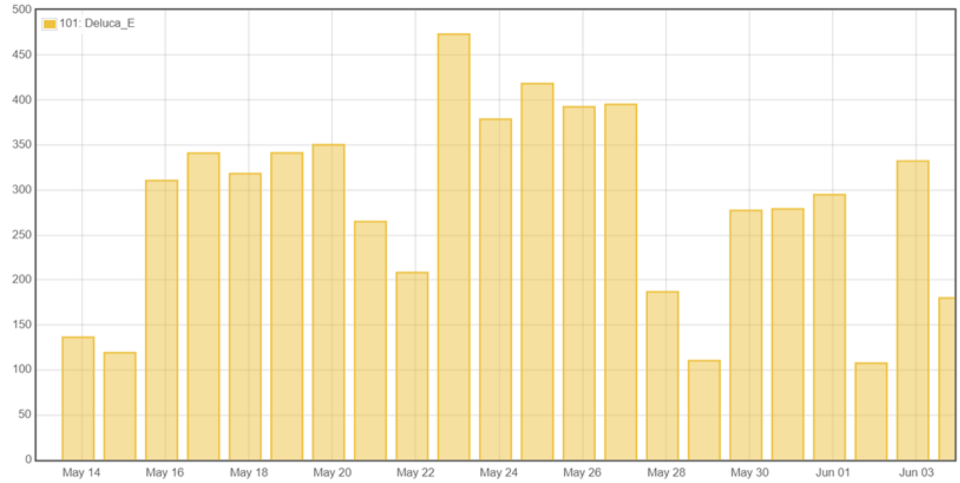

Figure 43. Daily consumption in kWh of a cold storage, NILM 519.

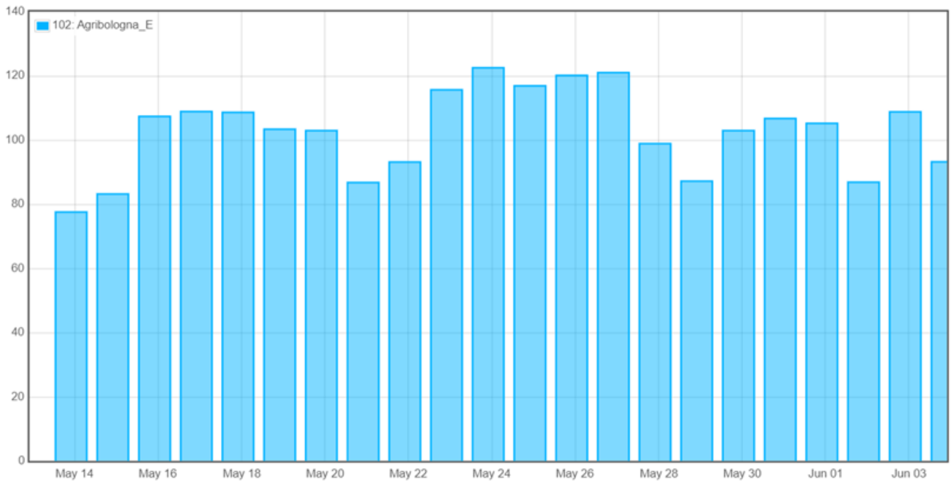

Figure 44. Daily consumption in kWh of an office, NILM 2517.

Based on the previous analysis, it is advantageous for load forecasting purposes to categorize weekdays into three types of days:

1. **Working days** (from Monday to Friday),
2. **Pre-holiday** (Saturday),
3. **Holiday** (Sunday).

Three distinct Load Forecast (LF) approaches have been proposed and tested. In approach (a), no adjustments are applied during the intra-day optimization to the day-ahead forecast, which is an average of a specific number of days within the same category. Method (b) involves modifying the anticipated load profile for the remaining day by scaling it to align with the total energy consumed the previous day. On the other hand, method (c) scales the residual load profile to ensure that, for the remaining day, it exhibits the same energy variation in relation to the day-ahead forecast as observed in the preceding part.

A. *Method a*

The first method assumes that the load consumption profile of a certain day is equal to the average of the consumption profiles of a specific number of days falling within the same category and no adjustments are made by the EMS during the intra-day optimization. The number of days upon which the profile is averaged can vary and can be equal to a 7, 5 or as low as 3 for example. As will become clearer in the explanation of the next two methods, it can be stated that the scaling factor of method (a) is equal to 1 at every time step i.

$$k_{a,i} = 1 \tag{6.1}$$

B. *Method b*

Method (b) performs an intraday adjustment over method (a). This method assumes that the total energy consumed throughout the current day is anticipated to be equivalent, at the end of the day, to what is forecasted by the load profile of method (a). At every time step i, the forecasted profile is subsequently scaled multiplying it by a factor calculated as follows,

$$k_{b,i} = \frac{E_{f,tot} - E_{t,i}}{E_{f,tot} - E_{f,i}} \tag{6.2}$$

where:

- $E_{f,tot}$ is the total amount of energy (kWh) which is anticipated to be consumed by the forecasted load power profile during the current day,
- $E_{f,i}$ is the amount of energy below the forecasted power profile consume from the beginning of the day (midnight) up until the current time step i,
- $E_{t,i}$ is the amount of energy consumed during the current day as measured by the smart meter up until the current time step i.

To mitigate substantial deviations from the forecast profile, a constraint is introduced on the scaling factor k_b, limiting its range between 0.8 and 1.2. This signifies that the profile can be adjusted within ±20% of the original forecast profile.

C. *Method c*

The third method operates on the assumption that the energy consumption for the remainder of the current day continues the trend observed up until the current time step. The forecasted profile is consequently adjusted scaling it by a factor calculated as follows,

$$k_{c,i} = \frac{E_{t,i}}{E_{f,i}} \tag{6.3}$$

where the variables are the same as introduced in method (a). Similarly, to the previous method, a constraint is applied to the factor $k_{c,i}$, limiting its range between 0.8 and 1.2. This ensures that the reshaping of the forecasted profile remains within ±20% of the original forecast.

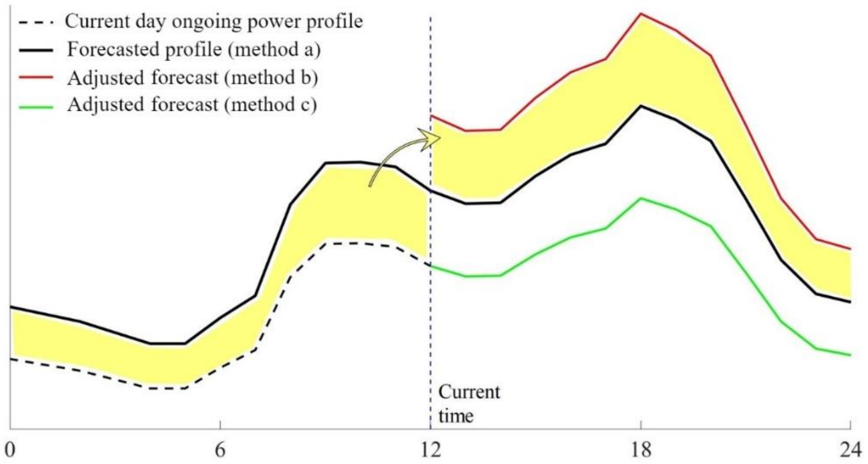

Figure 45. Load consumption power profile (W) and how the three methods adjust the profile forecast.

The three methods and how they reshape the load power profile is schematically shown in Figure 45. In the example shown the energy consumed up until the current time step, corresponding to midday, is lower than the forecasted one. In method (a), represented as a solid black line, no adjustment to the forecast is made. The yellow area represents the difference in energy that was forecasted to be consumed, up until the current time step, and the energy actually consumed as measured by the smart meter. That is the quantity $E_{f,i} - E_{t,i}$, which, in method (b), is expected to be consumed by the end of the day and it is equal to $(k_{b,i} - 1) \cdot (E_{f,tot} - E_{f,i})$. In method (c) the diminished consumption measured up until the current time step is expected to persist trough the rest of the day. In the following study cases a comparison of the results obtained with the three LF methods will be discussed.

6.4 EMS Algorithm for Optimal Scheduling of REC's BESS

The optimization function of the EMS is designed to simultaneously minimize the energy procurement costs for prosumers and maximize the incentives relative to the energy shared within the community. These incentives are formulated in alignment with the existing Italian Regulation [85].

$$OF = \sum_{t \in T, j \in J} (\pi_{t,j}^{-} P_{t,j}^{-} - \pi_{t,j}^{+} P_{t,j}^{+}) \, \Delta t - \sum_{t \in T_1} I_E E_S^t \tag{6.4}$$

Where:

- J is the set of REC's members, indexed by j
- T is set of time steps t, each of duration Δt, into which the time window is divided

- T_1 is the subset of T including just the time periods of the whole ongoing day
- $\pi_{t,j}^{+}$ and $\pi_{t,j}^{-}$ are the selling and buying energy price at time step t for the j-th member
- $P_{t,j}^{+}$ and $P_{t,j}^{-}$ are the power injection and absorption measured by the exchange meter M1 at time step t for the j-th member of the community
- E_S^t is the energy shared within the community for the current day
- I_E is the incentive per unit of energy shared

Currently, the Italian legislation provides an incentive for energy communities, known as the shared energy incentive I_E, set at €110 per MWh. In this framework, the shared energy is calculated on an hourly basis as the lesser of two values, as shown in Figure 46. In every time period t the shared energy E_S^t is equal to the minimum between the total energy consumed by all members of the community $\sum_{t\in T_1}^{j\in J} P_{t,j}^{-}$ and the renewable energy generated by the REC's prosumers, that is $\sum_{t\in T_1}^{j\in J} P_{t,j}^{+}$. This ensures that the incentive is applied only to the actual amount of renewable energy utilized within the community.

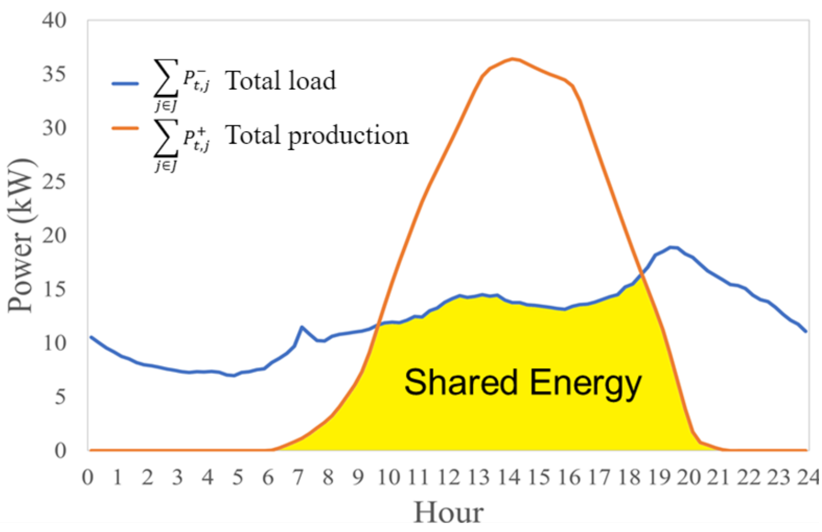

Figure 46. Graphical visualization of the energy shared within the REC.

In calculating the energy shared hourly within the REC, the load of the prosumers themselves is excluded. This is because their own consumption already results in bill savings and does not qualify for additional incentives. Therefore, the shared energy is determined based on the data from the exchange meters, that is M1, as illustrated in Figure 47 [86]. Additionally, the production meter M2, encompasses both the BESS and the PV system and must be therefore bi-directional. This design is crucial to accurately measure not only the energy generated by the PV system but also any grid charging activities of the BESS.

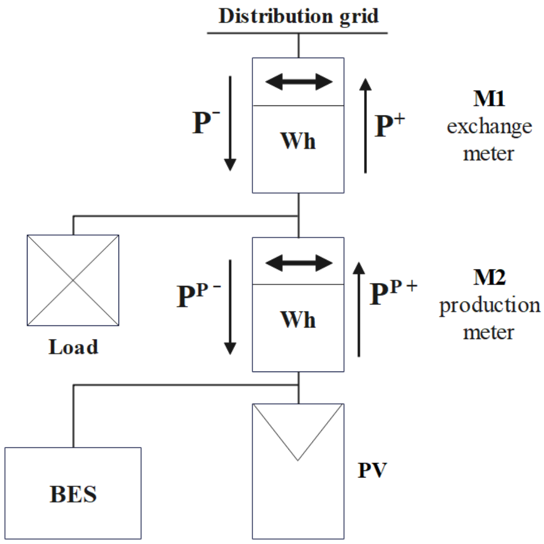

Figure 47. Metering scheme of a prosumer of the REC [87].

The power balance for the two meters is given by:

$$P_{t,j}^{+} - P_{t,j}^{-} = P_{t,j}^{P+} + P_{t,j}^{P-} - L_{t,j}^{S} \qquad \forall\, t, j \tag{6.5}$$

$$P_{t,j}^{P+} - P_{t,j}^{P-} = P_{t,j}^{PV} + P_{t,j}^{BES+} - P_{t,j}^{BES-} \qquad \forall\, t, j \tag{6.6}$$

Where:

- $P_{t,j}^{P+}$ and $P_{t,j}^{P-}$ are the power injection and absorption measured by the production meter M2 at time step t for the j-th member of the community
- $L_{t,j}^{S}$ is the prosumer's own load consumption
- $P_{t,j}^{BES+}$ and $P_{t,j}^{BES-}$ are respectively the discharge and recharge power of the BES system
- $P_{t,j}^{PV}$ is the power produced by the PV system

Variables $P_{t,j}^{+}$ and $P_{t,j}^{-}$ cannot be simultaneously different from zero. Therefore, they are defined as non-negative and through the implementation of binary variables, are constrained so that they cannot both be non-null within the same time interval. Similar constraints apply to the variables $P_{t,j}^{P+}$ and $P_{t,j}^{P-}$ as well as $P_{t,j}^{BES+}$ and $P_{t,j}^{BES-}$.

The incentive I_E rewarded for the energy share, is calculated solely upon the energy generated from renewable sources, it is therefore important to exclude energy arbitrage from this calculation. In this setup, BESS can be charged from the grid. This can be exploited for leveraging favorable price fluctuation during the course of the day. However, when this energy is reinjected into the REC, it becomes necessary to adjust the shared energy by a factor that estimates the recharge rate of the BES from the grid. This is typically calculated on a monthly basis, as referenced in [88]. A similar factor, denoted as $(1 - R_j)$, is herein adopted and is calculated over a shorter period equal to 48 hours. Where:

$$0 \leq R_j \leq 1 \qquad \forall j \tag{6.7}$$

and

$$R_j \sum_{t \in T} P_{t,j}^{P+} = \sum_{t \in T} P_{t,j}^{P-} \qquad \forall\, t, j \tag{6.8}$$

Basically R_j represents the ratio between the energy absorbed and released by the by the $j\text{-}th$ BES-PV system. If no energy arbitrage has been performed it is equal to zero and if energy arbitrage has been performed, its complementary to 1, takes track of the amount of renewable energy injected by the BES-PV system that was produced by the PV. This adjustment is crucial to ensure that the incentive accurately reflects the proportion of energy generated from renewable sources, considering the potential grid charging of the BESS. Consequently, the definition of shared energy within the community is delineated by the following constraints. It's noteworthy that these constraints are more stringent compared to the definition presented in [86], as they are evaluated for each forecast period t. This increased level of detail and scrutiny ensures a more precise determination of shared energy, aligning with the dynamic nature of each forecast period.

$$E_S^t \leq \sum_{j \in J} P_{t,j}^{+} \left(1 - R_j\right) \Delta t \qquad \forall\, t, j \tag{6.9}$$

$$E_S^t \leq \sum_{t \in T} P_{t,j}^{-} \, \Delta t \qquad \forall\, t, j \tag{6.10}$$

Regarding the energy balance of the BESS, the following constraints have been introduced:

$$E_{t,j}^{BES} = E_{t,j}^{BES,0} + \left(\sum_{t=1}^{t} P_{t,j}^{BES-} \eta_j - \sum_{t=1}^{t} P_{t,j}^{BES+} / \eta_j \right) \Delta t \qquad \forall\, t, j \tag{6.11}$$

Where:

- $E_{t,j}^{BES}$ is the energy stored in BESS $j\text{-}th$ at time step t
- $E_{t,j}^{BES,0}$ is the energy stored in BESS $j\text{-}th$ at the beginning of the time window
- η_j are the charging and discharging efficiency of BESS $j\text{-}th$

The initial value of the SOC of each BESS, thus the energy initial stored in each of them $E_{t,j}^{BES,0}$, is a value acquired by the EMS from the measurement database. Additionally, each BESS as a certain power limit and their SOC must remain within certain limits, that is,

$$0 \leq P_{t,j}^{BES+} \leq P_j^{BES,max} \qquad \forall\, t, j \tag{6.12}$$

$$0 \le P_{t,j}^{BES-} \le P_j^{BES,max} \qquad \forall\, t,j \tag{6.13}$$

$$E_j^{BES,min} \le E_{t,j}^{BES} \le E_j^{BES,max} \qquad \forall\, t,j \tag{6.14}$$

Equations (6.4) - (6.13) describe a mixed-integer linear problem that has been implemented in Matlab and solved utilizing Gurobi 10.0.

The optimization problem is solved at regular time intervals, following a rolling-horizon approach [16], as depicted in Figure 48. This approach enables leveraging updated forecasts for both PV generation and load demand, allowing precise adjustments to the BESS power setpoints based on the current operational conditions of the REC. In particular, forecasts are updated at every iteration t which have a duration equal to Δt which is set equal to 15 minutes. The time window horizon $T_{horizon}$, although being adjustable, is set to 48 hours as the accuracy of the PV generation forecasts deteriorates as $T_{horizon}$ increases. Finally, since the energy shared must be calculated on an hourly basis as per Italian regulation the time window rolls on an hourly basis every 4 iterations. Past measurements within that hour that are necessary to compute R_j and maximize E_S^t are read from the database at each iteration. The loads and PV power profiles are given a time resolution of 1 minute, that is, the measurement database is enquired every minute, and the BESS active power profiles are determined with a time resolution of 5 minutes.

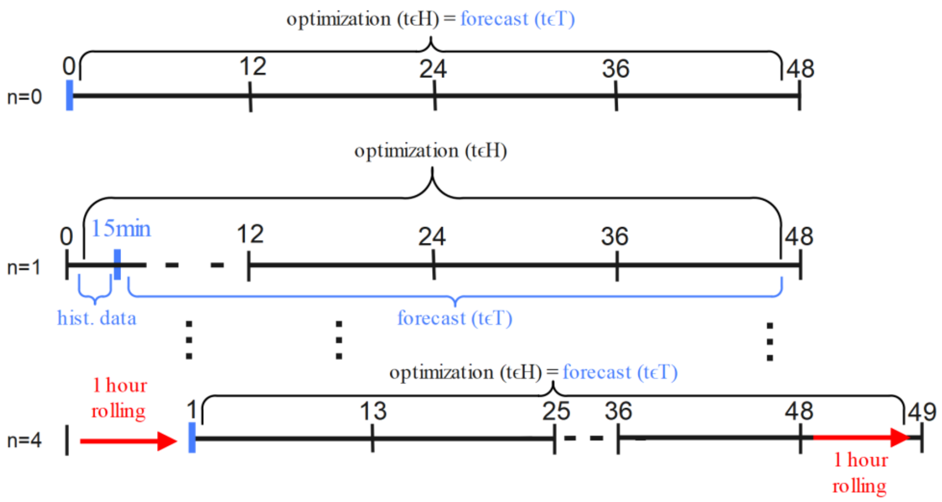

Figure 48. Rolling horizon approach adopted.

6.5 Real-Time Test Bed for the Validation of the EMS

In this section the real-time computer implementation of the test bed that allows to validate the EMS, including the distributed measurement system and the database, the PV and load forecasts, and the optimization algorithm that calculates the BESS active power setpoints is presented.

Digital real-time simulation facilitates closed loop testing and validation of new algorithms, providing essential support for developing equipment and strategies in a secure manner. This approach combines accuracy and flexibility, allowing to recreate various scenarios to evaluate the response of the system under test — whether in normal operating conditions, emergency situations, or rarely encountered operating conditions.

To ensure the simulation achieves and maintains real-time operation and response, substantial computing resources are essential. Consequently, specialized parallel processing architecture has been developed and employed in the implementation of real-time digital simulators [89].

Various approaches are available based on experimentation needs. The Software-In-The-Loop (SIL) approach is utilized for testing different version of the algorithm and forecasting methods developed for managing the REC. Essentially, SIL serves as a simulation-based software evaluation. In this application, the algorithm under test is compiled and employed to replicate specific behavior by running it alongside the real-time target.

6.5.1 Real-time software-in-the-loop simulation test bed

The real-time simulation test bed, schematically represented in Figure 49, encompasses the online database (DB), which retrieves measurements from the REC’s distributed measurement system, the PV forecast service, the EMS (ran on a pc at LISEP) and the REC’s network and BESs, simulated on an OPAL-RT.

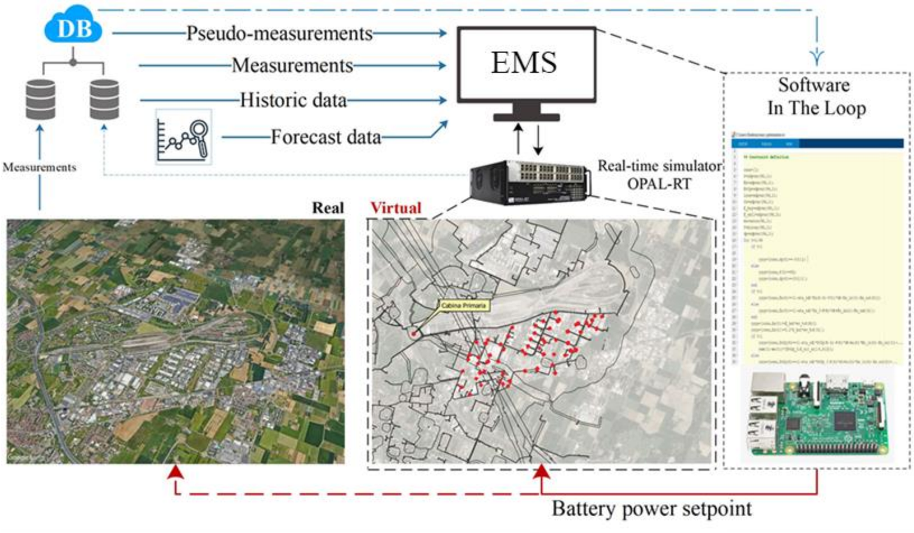

Figure 49. Real-time implementation of the EMS including the REC's distributed measurement system and the real-time simulator emulating REC's network and BESs.

The DB is populated in real-time with field measurements coming from the actual REC's network. Meanwhile, the virtual network is simulated on the real-time target (Real-time simulator OPAL-RT), serving as either an exact representation of the real network (digital twin) or a simplified/modified version, based on testing requirements.

The optimization algorithm resides within the EMS and undergoes testing using a SIL approach. The EMS retrieves real-measurements as well as historical data from the online DB, PV generation forecasts from the ForecastSolar service, and the NSP (National Selling Price) profile from the day-ahead Italian electricity market website (GSE), calculates the load demand forecast using one of the three methods previously discussed and feeds everything to the REC's representation on the OPAL-RT. Pseudo-measurements can also be generated from the DB to feed them to RECs networks, simulated on the real-time target, different from the real one.

The real-time target simulates the network, incorporating load and generation profiles, power flows along the lines, and more, based on real-time information from the database. Data pertaining to the BESs, such as active power and state-of-charge, are relayed from the real-time target to the database. The optimizer operates concurrently, maintaining constant communication with the real-time target. Optimization occurs periodically, with a cycle period equal to t equal to the frequency forecast update. At each optimization cycle, considering the most recent load and PV forecasts, the optimizer provides the power setpoints of the BESs. In the implemented test bed, this setpoint is transmitted to the virtual system in the real-time target. Moreover, the data related to the BES units, including their active power output and SOC, are transmitted from the real-time simulation target back to the DB as synthetic measurements, completing the loop. This integration allows these parameters to be factored into the REC exchanges, ensuring a comprehensive and accurate representation of the energy flows and storage within the REC. Another visual representation, encompassing just the EMS (in green) and the real-time target (in red), is shown in Figure 50. The upcoming chapters will demonstrate how, to experimentally validate a proof of concept of the EMS, the active power setpoints and measurements can also be transmitted to a Power Hardware-In-The-Loop (PHIL) test bed configuration.

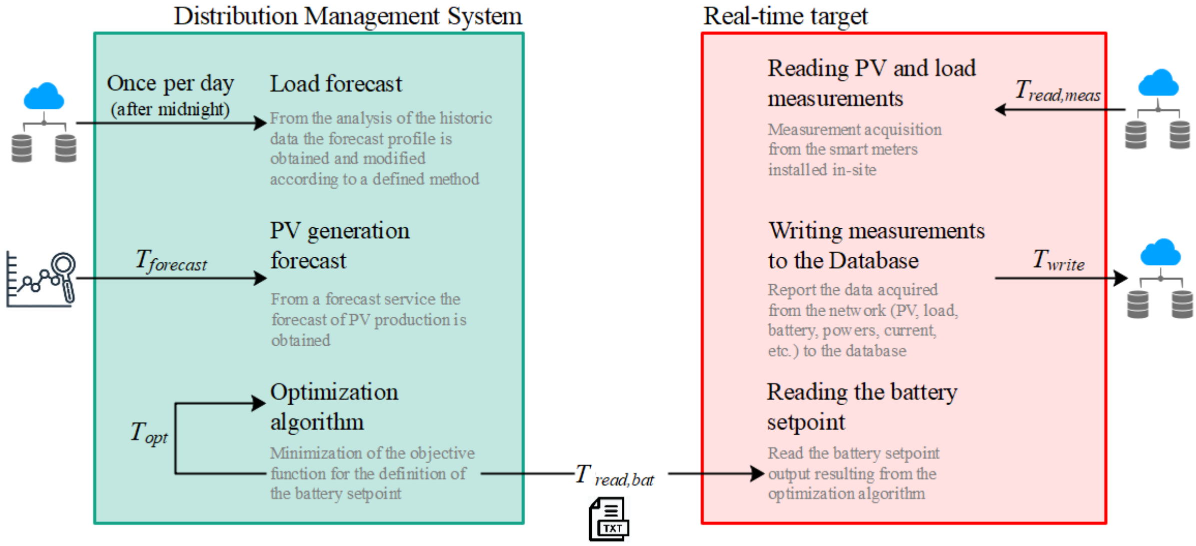

Figure 50. Relationship and operations carried out by the EMS (in green) and the real-time target (in red).

6.5.2 OPAL real-time target

The real-time simulator OPAL-RT encompasses three types of subsystems: the master subsystem, the slave subsystems, and the console subsystem. The master subsystem, a fundamental component in any real-time implementation, houses the computational elements of the model (e.g., the power system). While slave subsystems also include computational elements, they are exclusively used when the process is distributed across multiple cores running in parallel. In the presented implementation, no slave subsystem is necessary. Finally, the console subsystem operates on the command station, which can be the same pc where the EMS is ran, facilitating real-time interaction with the system. It includes switches, blocks related to data acquisition and visualization and runs asynchronously in comparison to the master [90].

The top layer of the real-time Simulink model, showcasing both the master and console subsystem, is depicted in Figure 51. The master runs in the real-time target, it contains the Simulink model of the REC's network, which will be presented in the next section, is not accessible to the user while running in real-time and transmits data to be visualized to the console. The console can run on the user's pc and contains blocks acquiring measurements, PV and loads forecast, as well as BESs setpoints produced by the optimizer and sends them to the master. In the console, plots, displays, as well as switches and selectors to interact asynchronously with the master are implemented.

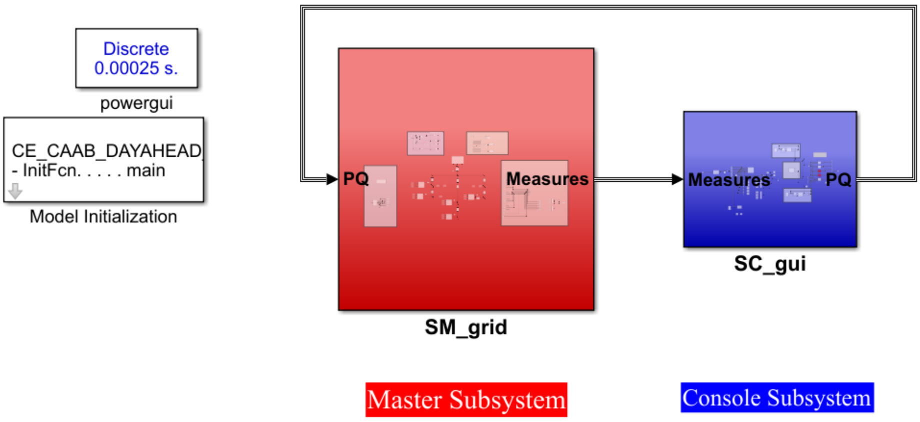

Figure 51. Top layer of the Simulink model on the real-time target, showcasing both the master and console subsystem.

In real-time simulations, closely monitoring the number of overruns is crucial. Overruns occur when the computations required within a given time step exceed the available time, suggesting that the simulation system is unable to process data quickly enough. Ideally, the number of overruns should be zero or very close to it at the end of the simulation. A high number of overruns can negatively affect the simulation's performance. The primary aim of real-time simulations is to resolve the equations of the power system model and execute relevant control and protection actions within a real-world time-step [91]. Therefore, unlike typical simulations where the goal is to minimize total simulation time, the objective in real-time simulations is to minimize the maximum time-step required [92].

For the EMS SIL test bed, the time-step is set at 250 microseconds (μs), which is deemed sufficiently small. For a typical run, the maximum execution cycle time recorded is around 80 μs, well below the set time-step. CPU usage for the master system, handling all real-time calculations, is approximately 31%, indicating that the system is not overloaded. A good amount of total idle time indicates that there is available margin for more complex computations. This suggests that the system's performance is stable and efficient under the current testing conditions and that the tested system could handle more complexity or operate with a reduced step-time if needed.

6.5.3 REC configurable model

In the OPAL's master, the Simulink model of the REC can be found. The model is constructed in such a way to be highly reconfigurable so to be able to simulate a large variety of RECs' networks. In Figure 52, a possible REC configuration is depicted. It contains 5 prosumers connected to the distribution network and between themselves by 3 lines branches. Two of the prosumers have been disabled and each of them can act just as a consumer by setting its PV generation to zero. In the case of GECO's network, to be thoroughly discussed in the next chapter, it comprises two consumers, representing an office load and an industrial load, and one prosumer.

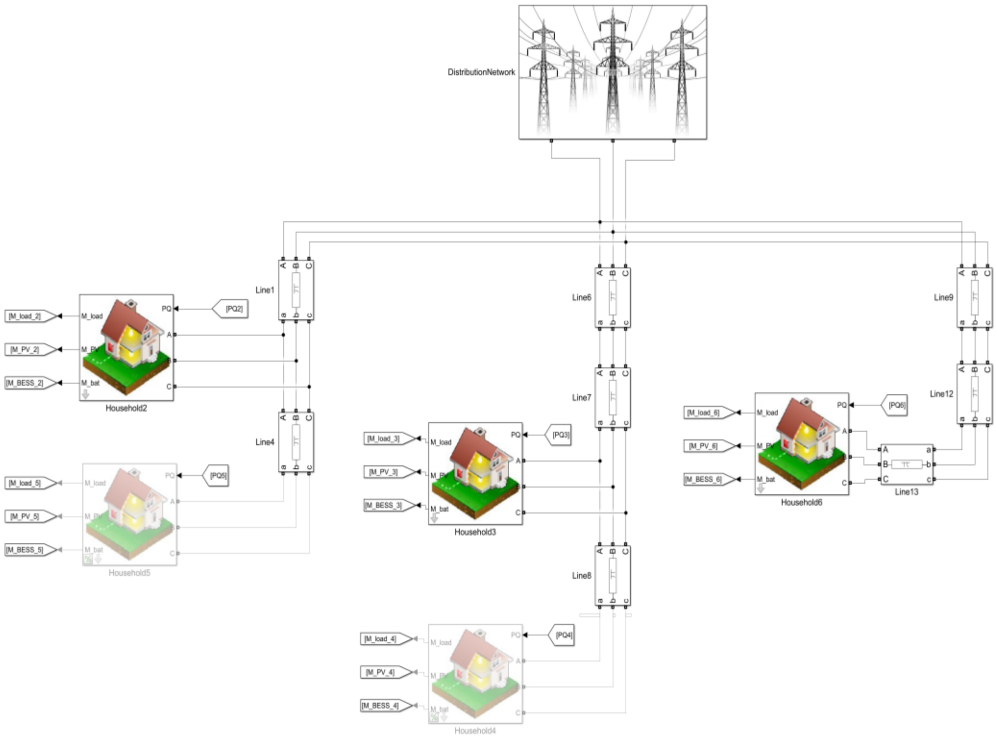

Figure 52. Configurable REC model with 5 modular prosumers.

The components of each household are illustrated in Figure 53, consisting of a load, a PV installation, and a BES. Both load and PV generation follow their respective consumption or generation profiles transmitted by the console and acquired from the database. Similarly, the BES follows the power profile generated by the optimization algorithm. Each element has its own measurement block and can be activated or deactivated based on the specific characteristics of the prosumer. Active and reactive power are measured, as well as phase voltages and currents. Additionally, regarding the BES, the SOC is measured.

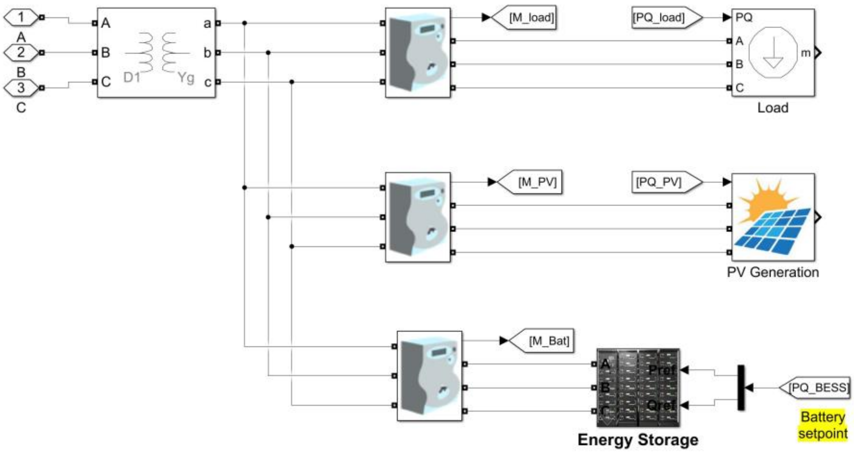

Figure 53. Simulink model of each of the prosumers in the REC.

6.5.4 BES model

The steady-state model of the BES primarily consists of a controller, highlighted in red in Figure 54. The controller's role is to restrict the battery output. An overcharge limit is implemented to prevent the battery from charging when the SOC reaches its maximum limit (SOC_{max}). Conversely, an undercharge limit prevents the battery from discharging when the SOC is at its minimum (SOC_{min}).

The stored energy calculation block, in green, is responsible for computing the SOC:

If charging
$$SOC_{t+T_s} = SOC_t + \frac{\sqrt{P^2 + Q^2} \cdot \eta \cdot T_s}{E_{BES}} \cdot 100 \tag{6.15}$$

If discharging
$$SOC_{t+T_s} = SOC_t - \frac{\sqrt{P^2 + Q^2} \cdot T_s}{\eta \cdot E_t^{BES}} \cdot 100 \tag{6.16}$$

The calculation of the SOC at each subsequent iteration involves the effective active and reactive power outputs of the BES, the charging and discharging efficiency η as well as the simulation time step duration T_s, typically between 50 and 250 μs. The overall battery energy capacity is denoted as E_{BES}. It's important to note that herein the REC's model neglects the dynamic effects and time delays introduced by the inverter.

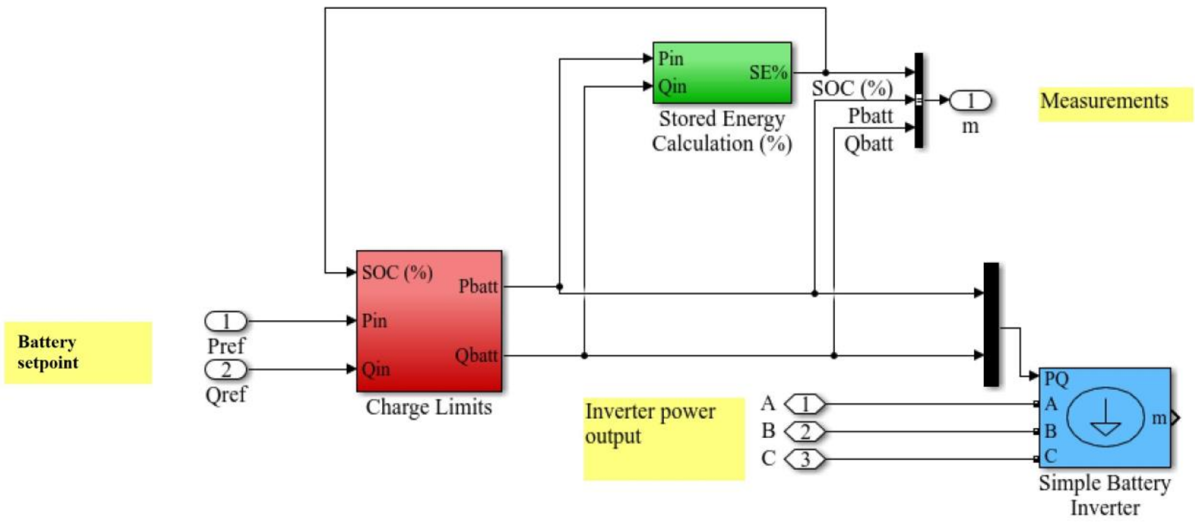

Figure 54. BES model implementation.

The REC model presented as well as the test bed setup will be leveraged in the following chapter to discuss two relevant case studies and validate the proposed EMS.

Chapter 7. Real-Time Software-in-the-Loop Testing and Validation of the EMS

In this chapter, leveraging the test bed setup in the LISEP facilities, the real-time SIL testing and validation of the EMS is performed. To do so, two distinct case studies, formulated within the framework of the GECO project, are presented and analyzed.

The first case study represents the pilot REC comprising of the five customers in the CAAB premises metered by NILM devices and described in Subsection 6.2.1. Among these members, one is a prosumer, equipped with a 94kW PV plant and a 30kW/60kWh BESS that is not currently installed and has been simulated in the digital environment of the OPAL-RT.

The second case study delves into a hypothetical REC scenario, created leveraging aggregated load demand data of two primary substations in the Pilastro-Roveri district, provided by the main Italian DSO, as well as metered PV generation. This REC is connected to the MV distribution grid, where the energy demand is significantly higher compared to the first case study. This REC includes two simulated prosumers, both equipped with PV plants and BES. Specifically, Prosumer 1 has a 300kW PV plant and a 100kW/500kWh BES, while Prosumer 2 possesses a 250kW PV plant and a 100kW/350kWh BES.

7.1 Simulation Parameters

For both case studies, the simulation is conducted over the course of two consecutive days, specifically March 23rd and 24th, 2023. During this simulation, three Load Forecasting (LF) methods, as detailed in Section 6.3.2, are compared and evaluated for their effectiveness in the RECs under consideration. This comparison aims to assess the performance and accuracy of the different LF methods within the context of the specific RECs, providing insights into the most suitable forecasting approach for each community's unique energy dynamics and characteristics.

In both scenarios being considered, the BESs begin the simulation with an initial SOC equal to 40%. They have a minimum allowable SOC of 10%, ensuring the batteries are not excessively discharged. Additionally, the BESs are characterized by an efficiency equal to 95% for both charging and discharging processes.

Regarding the financial aspects, the energy purchase price is set as the hourly Italian National Single Price (NSP), also known as PUN (Prezzo Unico Nazionale), plus a spread dependent on the energy provider. Conversely, the selling price is pegged to the NSP. The algorithm updates daily, acquiring the NSP for the next day from the Italian electricity market website [93] after its publication at 1 p.m. This updated NSP value is then incorporated into the optimization problem for the forthcoming day as soon as it's available. If the new NSP is not yet accessible, the pricing profile from the current day is used instead. This approach ensures that the optimization calculations always reflect the most current pricing information available.

Three price scenarios have been analyzed:

- **Scenario (i):** The energy selling price is pegged to the NSP for the 23rd and 24th of March 2023, an additional price spread of 15 c€/kWh is added to the buying price.
- **Scenario (ii):** The NSP for the same dates, 23rd and 24th of March 2023, is considered, but with a higher price spread of 22 c€/kWh.
- **Scenario (iii):** In this scenario, the NSP from an earlier period, specifically 5th and 6th of December 2022, is applied. However, this pricing is used in conjunction with the load and PV data from the 23rd and 24th of March 2023. The price spread in this case is set to 15 €/MWh.

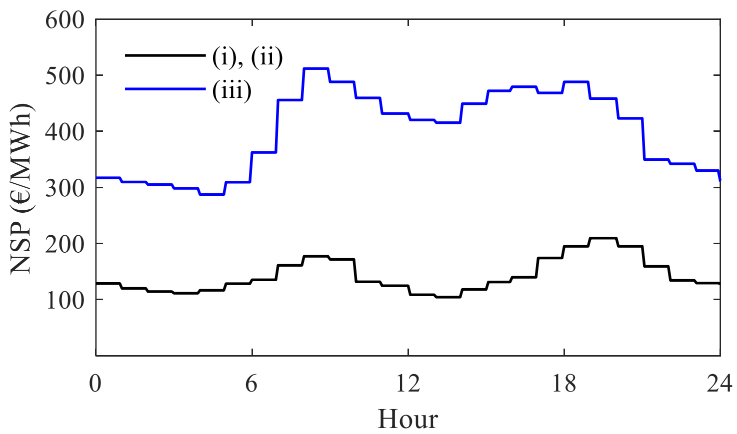

Figure 55. NSP of the 23rd of March 2023, in black, used for price scenarios (i) and (ii). In blue the NSP of the 5th of December 2022, used for price scenario (iii).

In Figure 55, the hourly trend of the NSP used in the three scenario is shown. In black, the NSP of the 23rd of March 2023, used for price scenarios (i) and (ii). In blue the NSP of the 5th of December 2022, used for price scenario (iii).

In Table 21 the relevant parameters regarding the optimization algorithm time frames, the BES system and the energy prices considered in the following simulations are presented. The two case studies differ for number and size of the BESs and for the price scenarios applied. Concerning CAAB's REC, just the first price scenario has been considered. While for the Pilastro-Roveri REC, its behavior under all three price scenarios has been analyzed.

Table 21. Relevant parameters regarding the optimization algorithm time frames, the BES system and the energy prices.

Parameter description	**Symbol**	**Value**
	Relevant Time Periods	
Optimization Period	T_{opt}	15 min
PV generation Forecast	$T_{forecast}$	15 min
Load and PV resolution	T_{load}	1 min
BESS resolution	T_{bess}	5 min
Rolling period	T_{roll}	1 h
NSP update	T_{NSP}	24 h
Rolling Horizon	$T_{horizon}$	48 h
	Battery Energy System	
Rated capacity	E_{BES}	60 kWh
Rated power	P_{BES}	30 kW
Efficiency	η	0.95
Initial SOC	SOC_{ini}	40 %
Maximum SOC	SOC_{max}	100 %
Minimum SOC	SOC_{min}	10 %
	Energy prices and incentives	
Purchase price	p_{buy}	NSP + spread
Sales price	p_{sell}	NSP
Incentive to shared energy	I_E	110 €/MWh

7.2 CAAB's REC case study

Regarding the first case study, the test bed setup, described in Section 0, is configured as shown in Figure 56. The distributed measurement system installed in the CAAB premises in the framework of the GECO project and described in Section 6.2, has been leveraged. In particular, the load and PV profiles measured by the NILM devices, detailed in Subsection 6.2.1, and representing 4 consumer and 1 prosumer in the CAAB area are used. The measurements, as well as the historical data and the PV forecast are processed by the EMS to compute the BES power setpoint which is then sent to the OPAL-RT simulator.

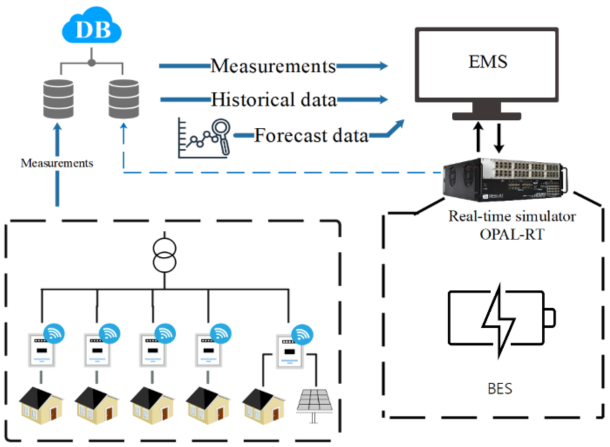

Figure 56. Test bed configuration for the case of GECO's REC. The EMS uses real-time measurements from 5 NILM devices, encompassing 4 consumers and 1 prosumer. The real-time target emulates the REC's network including the BES.

The first day of the simulation, March 23rd, 2023, was a Friday. The load demand forecast is made over a 48-hour time window. The load profile of each member of the REC is forecasted as its average power profile of the three former days of the same type (i.e., working day, pre-holiday or holiday). This is the starting profile for the Load Forecast (LF) adjustments discussed in Subsection 6.3.2. In Figure 57, as an example, this is shown for NILM device ID 519, corresponding to a consumer whose main load is constituted by cold room storage, as also evidenced by its frequently intermittent nature.

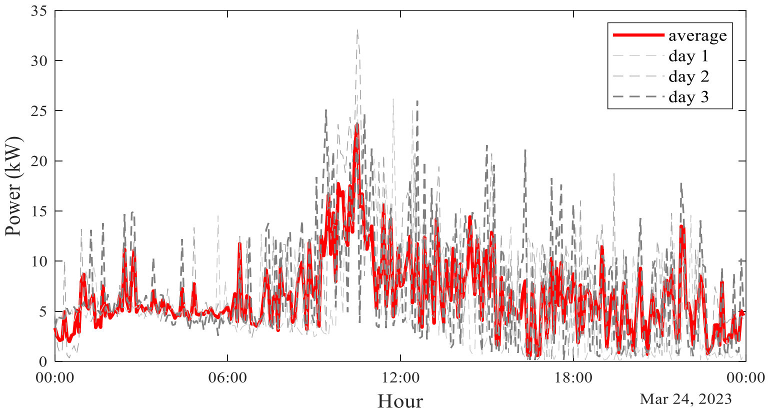

Figure 57. Load profile of the three previous Saturdays, in dashed grey, and forecast at the beginning of the day for the consumer metered by NILM device ID 519.

At the beginning of the time window the EMS basically performs a day-ahead optimization. Figure 58 illustrates the aggregated loads of the four passive consumers in the REC, as a thin black line labelled as "REC load", alongside the load of the prosumer, thick black line indicated as "Load." This figure presents the outcomes derived using LF method (a). It displays the BES forecasted power profile, in green, as well as the load and PV forecast used by the optimizer, in red. This forecast is based on the optimization step conducted at midnight on March 23rd. However, for clarity, only the first 24 hours are shown, despite the optimizer utilizing a 48-hour time window.

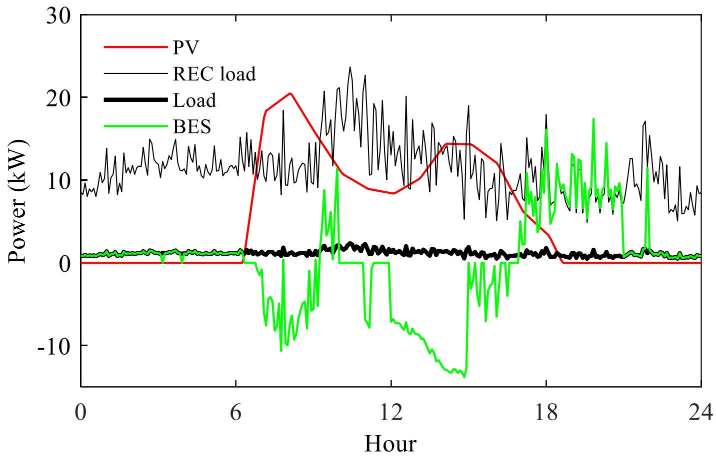

Figure 58. First 24 hours of the optimization performed at the beginning of the time window, using LF method (a) and NSP price scenario (i).

According to the BES power profile calculated at the beginning of the time window, the optimizer predicts selling energy during periods when the NSP is higher, such as at around 10 am and from around 5 pm to 9 pm. It also anticipates charging the BES either when PV generation exceeds the REC load or when the hourly NSP is lower, particularly around and after noon. The pricing scenario considered here is (i), which has a buying price equal to the NSP plus a 15 cents per kWh spread and a selling price equal to the NSP, see Figure 46.

Figure 59, on the other hand, shows the power profiles resulting from the rolling-horizon optimization as actually measured at the end of the time window. The BES alongside the measured PV production and load consumption are shown. The rolling-horizon approach involves continuously updating forecasts, leading to a significantly different BES behaviour compared to the initial forecast. The main difference resides in the fact that, at the beginning of the time window, the day was forecasted to be cloudy with a peak PV production at around 10 am of about 20 kW. The PV production ended up peaking above 60 kW at around noon. This illustrates the dynamic nature of the system and the importance of a rolling-horizon approach, continuously updating the PV forecast, in managing energy resources efficiently.

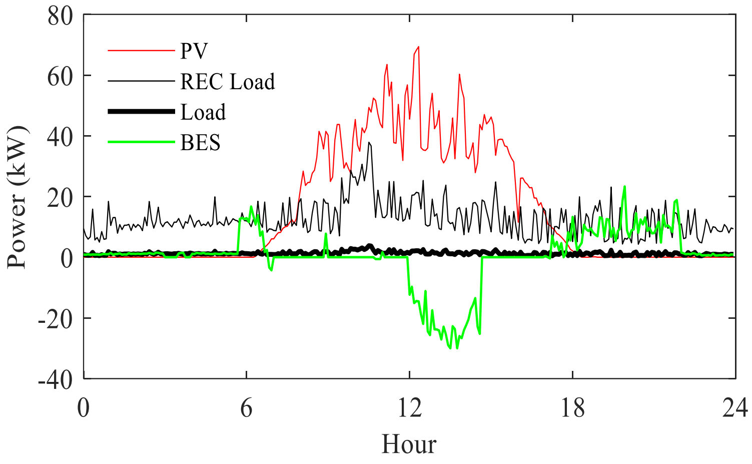

Figure 59. First 24 hours of the rolling optimization as actually happened at the end of the time window, using LF method (a) and NSP price scenario (i).

For comparison, Figure 60 shows how the prosumer would act with no optimization at all and basically no REC. The BES is charged when PV exceeds the prosumer own load and discharged when the prosumer's load exceeds the current PV generation (such as during cloudy periods, at night, or during high demand periods).

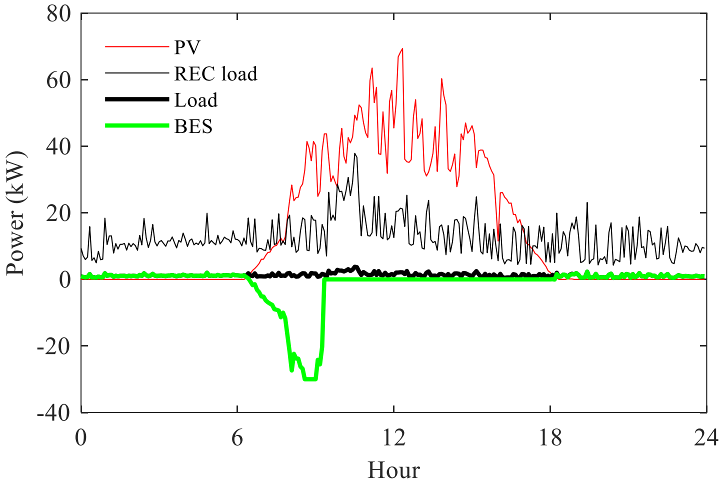

Figure 60. First 24 hours with no optimization at all.

Table 22 displays the key energy and economic outcomes from the day-ahead and rolling optimization algorithms over the two-day simulation period. The total revenue is determined by subtracting the cost of energy purchased by the prosumer from the income generated from energy sales, with an added incentive calculated on the energy shared E_s, which should be distributed among REC's members. It's important to note that the energy costs for passive REC consumers are not included in this table as these costs remain constant across all scenarios and are not influenced by the optimization algorithm.

Table 22. GECO's REC energy and economic results

	Energy (kWh)				**Cost/Revenue (€)**			
Opt.	***Day-ahead***	***Rolling***			***Day-ahead***	***Rolling***		
		a	***b***	***c***		***a***	***b***	***c***
Buy	4.10	3.68	2.80	2.60	- 1.15	- 1.00	- 0.76	- 0.73
Sell	700	698.90	696.50	697.40	92.50	93.44	92.70	93.19
E_s	335	345.10	345.40	344.00	36.90	37.96	37.99	37.84
				Total revenue:	128.25	130.40	129.93	130.30

In this specific scenario, the advantage of employing a rolling optimization strategy for managing the BES is somewhat minimal when compared to the day-ahead approach. This limited benefit is attributed to the REC's sole prosumer having a relatively small load and a BES that, while adequate for self-consumption needs, is modest in comparison to the size of the PV installation. The financial gains observed range from 1.68€, for LF method (b), to 2.15€, for LF method (a), over the course of the two days. Percentage wise, with respect to the day-ahead optimization, the rolling optimization approach using LF method (a) displays a 1.7% revenue increase. Fairly similarly, LF method (c) lead to a 1.6% revenue improvement, while this figure is equal to 1.3% for LF method (b). Furthermore, the final SOC of the BES shows values of 20.0%, 20.6%, 22.9%, and 21.3% for the day-ahead and the three rolling scenarios (a, b, and c) respectively.

In summary, while rolling optimization is a more flexible and potentially more efficient approach, its advantages depend heavily on the specific characteristics of the REC, including the size of the load, the capacity of the BES, and the predictability of PV generation. Nevertheless, the test bed setup comprising the distributed measurement system, the online database, the EMS and the real-time target performed nominally.

7.3 Pilastro-Roveri REC case study

The proposed real-time digital simulation platform can be utilized for analyzing and planning various configurations of a REC. As anticipated, in the case of the Pilastro-Roveri REC, load demand data comes from aggregated measurements of the feeders of a primary substation, following the test bed configuration outlined in Figure 61. This scenario involves several aggregated passive consumers, based on historical data provided by the DSO, and two simulated prosumers. Both prosumers are equipped with PV plant and BES. Specifically, Prosumer 1 has a 300kW PV plant coupled with a 100kW/500kWh BES, and Prosumer 2 is equipped with a 250kW PV plant and a 100kW/350kWh BES. The PV production for the simulation is modeled by appropriately scaling the output of the existing 94 kW PV of CAAB’s REC, monitored by the NILM device corresponding to ID 348. This method allows for the realistic simulation of PV production based on actual, measured data, ensuring that the simulations are grounded in real-world PV performance metrics. In addition to price Scenario (i), for the Pilastro-Roveri REC, its behavior following price scenarios (ii) and (iii) has been analyzed.

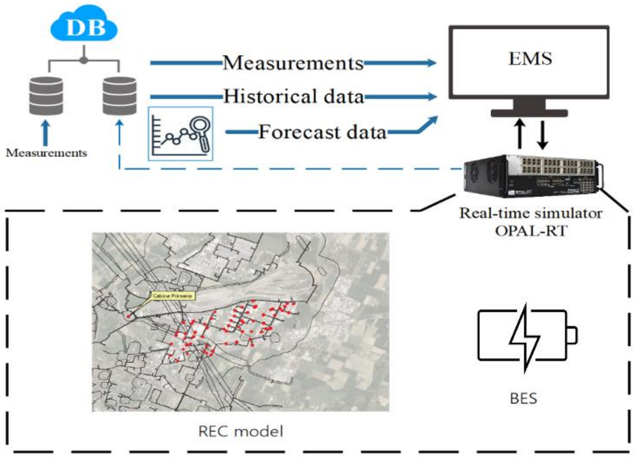

Figure 61. Testbed configuration for the MV REC study case. The EMS uses aggregated measurements of several consumers. The real-time target emulates the REC's network including the BES.

The first 24 hours of the simulation are displayed in Figure 62. The measured PV generation and load of Prosumer 1 own load, in thick black, as well as the aggregated load of the entire REC, thin black line, are shown. Compared to the previous case study both loads are more sizable with respect to PV generation.

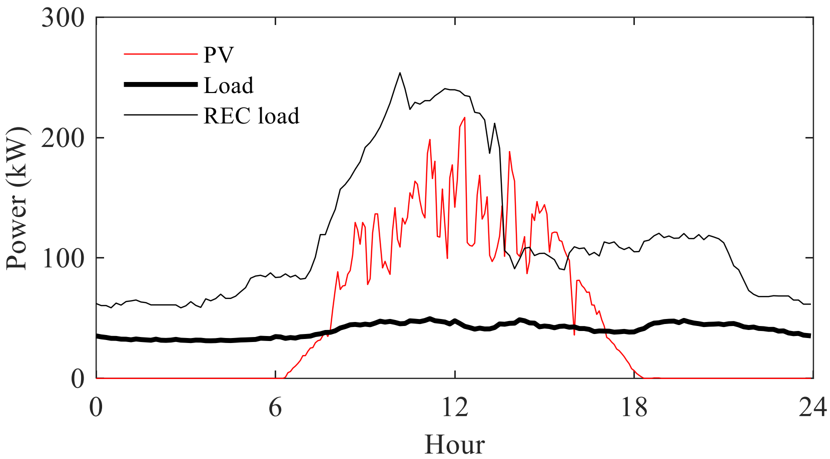

Figure 62. First 24 hours of PV generation and own load of Prosumer 1 as well as REC's aggregated load.

The power profiles of the BES, under the three different price scenarios with LF method (a), are shown in Figure 63. Each pricing scenario influences the management of the BES in distinct ways. In price Scenario (i), represented as a solid light grey line, the BES power profile follows that of price Scenario (ii) until 18 p.m.

In Scenario (ii), represented as a dark grey dashed line, priority is given to self-consumption by the prosumer, particularly after 7 p.m., favoring the use of stored energy over participating in energy sharing. This is because, Scenario (ii) follows the same NSP profile of Scenario (i) but with a 50% greater price spread. Meaning that the energy selling price is the same, but the buying price is higher, making it more convenient on some occasions for the prosumer to satisfy its own load instead of injecting power into the grid or sharing it within the community.

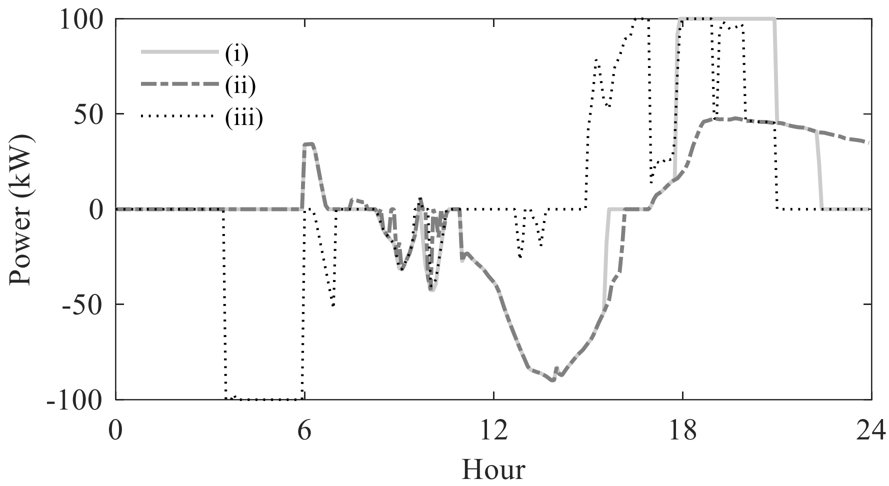

Figure 63. BES power profile calculated with the rolling horizon approach, with LF method (a), following price scenarios (i), (ii) and (iii). First 24 hours.

In Scenario (iii), represented as a dotted line, which features an entirely different NSP profile, the BES is charged from the grid during the early morning hours (approximately 4 a.m. to 6 a.m.). This is done to take advantage of lower energy prices during these hours, engaging in a strategy known as energy arbitrage. This approach is advantageous in maximizing economic benefits by buying energy when it's cheaper and using or selling it when prices are higher. With reference to Figure 55, this strategy is adopted as the NSP price of Scenario (iii) displays larger price fluctuations, up to ±200 €/MWh during the day, with respect to the first two scenarios as well as an average price of about 400 €/MWh which is much higher than the shared energy incentive I_E of 110 €/MWh. This highlights the impact of the NSP on the BES management by the EMS. Given that the economic incentive as well as the price spread are fixed values,

These results may be more easily understood by looking at the SOC of the BES, shown in Figure 64. In the first two scenarios, the behavior of the BES differs after 6 p.m. when the BES discharges more slowly meeting its own load demand until the end of the day. In the third price scenario, given higher price fluctuations during the day, the BES does not wait excess PV production to charge but leverages low energy prices in the early morning to increase its SOC. At the end of day one the SOC in Scenario (i) is equal to 42.8%, in Scenario (ii) is just below

20% and in price Scenario (iii) reached its minimum allowable value of 10% having discharged all its capacity to take advantage of favorable energy prices.

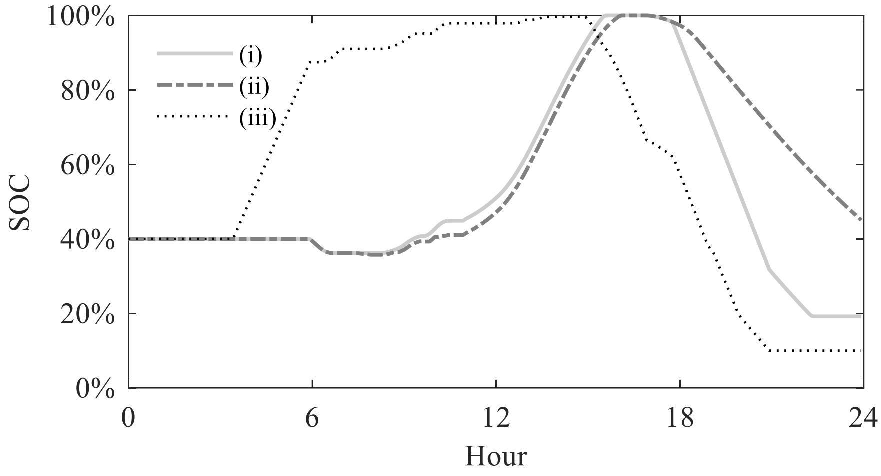

Figure 64. First 24 hours of the SOC power profile following price scenarios (i), (ii) and (iii).

The simulation has been repeated via rolling window optimization and for LF methods (a), (b) and (c) as well as day-ahead optimization for each of the 3 price scenarios. The energy and economic results at the end of time window for price Scenario (i), (ii) and (iii) are reported in Table 23, Table 24 and Table 25 respectively. With respect to the day-ahead optimization the rolling horizon approach performs better, either in terms of revenue increase or cost reduction, regardless of the LF method used and of the price scenario. It's important to consider also the SOC value of the BESs at the end of the simulation, as some strategies might have discharged more energy into the grid than others, keeping in mind that the initial SOC was set to 40% in all the simulations. As reported in [87], the final SOC for the BES of prosumer is equal to 27.6%, 34.6%, 39.9% and 34.2% for the day-ahead and rolling LF methods a, b and c, respectively. For prosumer 2, the final SOC is equal to 23.9%, 28.2%, 24.4% and 32.1% respectively. It can be noted how, in the day-ahead optimization, the final SOC is lower than in any of all the other cases. Pointing at how, the rolling optimization approach was able to obtain better economic results while simultaneously managing the storage asset in a more efficient way and preserving a higher level of charge for the days to come.

Table 23. Pilastro-Roveri REC energy and economic results for price scenario (i).

		Energy (kWh)				Cost/Revenue (€)			
Opt. method		***Day-ahead***	***Rolling***			***Day-ahead***	***Rolling***		
			a	***b***	***c***		***a***	***b***	***c***
Pros. 1	***Buy***	517	519	533	551	- 142.72	- 142.53	- 145.91	- 151.16
	Sell	933	891	879	925	128.89	131.15	127.70	136.74
Pros. 2	***Buy***	713	730	715	725	- 200.10	- 203.51	- 204.67	- 202.06
	Sell	742	747	765	728	104.60	112.04	114.13	109.39
	$\boldsymbol{E_s}$	1646	1636	1634	1652	180.00	179.90	179.78	179.78
Total revenue:						70.66	77.06	71.02	72.69

Table 24 details the outcomes of price scenario (ii), characterized by a larger difference between the buying and selling energy prices compared to scenario (i). These results indicate a strategic preference in this scenario for conserving stored energy to prioritize self-consumption by the prosumers, minimizing energy transactions (buying, selling, and sharing) within the REC, a response driven by the higher price spread in scenario (ii). Notably, the rolling optimization method results in decreased costs for the REC when compared with the day-ahead strategy.

The final SOC for the BES of prosumer is equal to 44.3%, 44.8%, 39.9% and 46.2% for the day-ahead and rolling LF methods a, b and c, respectively. For prosumer 2, the final SOC is equal to 47.4%, 43.4%, 36.5% and 48.4% respectively.

Table 24. Pilastro-Roveri REC energy and economic results for price scenario (ii).

		Energy (kWh)				Cost/Revenue (€)			
Opt. method		***Day-ahead***	***Rolling***			***Day-ahead***	***Rolling***		
			a	***b***	***c***		***a***	***b***	***c***
Pros. 1	***Buy***	517	349	369	375	- 178.87	- 120.13	- 126.37	- 129.43
	Sell	859	673	715	691	110.86	88.09	94.64	91.05
Pros. 2	***Buy***	751	613	623	604	- 268.11	- 219.07	- 221.64	- 215.47
	Sell	717	578	610	550	93.14	81.54	86.18	76.26
	$\boldsymbol{E_s}$	1520	1250	1325	1240	167.35	137.51	145.73	145.73
Total revenue:						-75.64	-32.06	-21.45	-31.86

In the first two price scenarios, the coefficient R, which tracks the amount of renewable energy shared by the prosumers actually produced by the PV system, on which the incentive must be calculated, is equal to 0 for both prosumers. Indicating that no energy arbitrage has been performed. However, in price Scenario (iii), as presented in Table 25, the situation changes. Here, driven by stronger NSP fluctuations, the algorithm engages in energy arbitrage, which leads to values of R greater than 0. For Prosumer 1, R is 0.04 in the day-ahead scenario and 0.20 in all the rolling scenarios (a, b, and c). For Prosumer 2, R values are slightly different, with 0.02 in the day-ahead scenario, and 0.20, 0.21, and 0.21 in the rolling scenarios (a), (b), and (c), respectively. In this third scenario, the final SOC reaches the minimum value of 10% in all rolling scenarios. In contrast, the day-ahead approach results in a final SOC of 27.4% for Prosumer 1 and 17% for Prosumer 2. This shows how, in the rolling optimization approaches, the EMS was able to leverage the BES to increase the amount of energy drawn from the grid, reselling it at favorable energy prices, and obtain a revenue increase of 9.3%, 8.0% and 7.1% for LF method a, b and c respectively.

Table 25. Pilastro-Roveri REC energy and economic results for price scenario (iii).

		Energy (kWh)				Cost/Revenue (€)			
Opt. method		***Day-ahead***	***Rolling***			***Day-ahead***	***Rolling***		
			a	***b***	***c***		***a***	***b***	***c***
Pros. 1	***Buy***	912	1306	1265	1319	- 442.62	- 603.93	- 583.32	- 610.70
	Sell	1385	1793	1750	1816	614.55	787.06	768.20	793.44
Pros. 2	***Buy***	916	1273	1235	1285	452.45	- 594.90	- 574.92	- 601.38
	Sell	999	1350	1308	1364	443.53	582.66	563.37	588.39
	E_s	2114	2379	2309	2393	232.65	261.73	254.00	254.00
Total revenue:						395.65	432.62	427.33	423.74

These two case studies allowed us to test and validate the proposed EMS as well as to prove the functionalities of the test bed simulation set-up. The EMS is tailored to the REC's Italian regulatory context, taking into account the varying costs of buying and selling electricity, as well as incentives for energy sharing among REC members. It employs a rolling horizon strategy, focused on reducing energy procurement costs for the REC through effective control of the prosumers' BES systems. This approach leverages both historical data and real-time smart meter readings, coupled with continually updated forecasts for load and PV generation.

Additionally, the EMS is integrated with a real-time simulator to validate its communication infrastructure and the real-time functionality of the optimization process. The simulator encompasses the model of the REC’s network, complete with its meters and BES units, enabling the assessment of the EMS's performance using both actual field data and simulated prosumer power profiles.

The effectiveness of the EMS was evaluated in two distinct REC setups, employing three different methods for load forecasting and three varying energy price scenarios. These were then benchmarked against a traditional day-ahead approach. The results indicate that the EMS can either enhance the overall revenue of the REC or lower the total cost of energy procurement, demonstrating its superiority over the day-ahead strategy.

In terms of evaluating the load forecasting methods, the current findings are not definitive, indicating the necessity for more in-depth research. Presently, it appears that method (a), which involves averaging a few preceding days within the same category without making intraday adjustments, is sufficiently effective. Surprisingly, methods (b) and (c), despite incorporating what seem to be reasonable intraday adjustments, do not exhibit significant improvements. This outcome suggests that the additional complexity of methods (b) and (c) may not yield correspondingly enhanced forecasting accuracy, underlining the need for further investigation to understand these dynamics better.

Chapter 8. Real-Time Power Hardware-in-the-Loop Experimental Validation

In this chapter, the EMS capabilities were evaluated in a Power Hardware-in-the-Loop (PHIL) setup at the Smart Grid and Electric Vehicle Lab (SGEVL) at the INESC TEC facilities in Porto. The reasons behind this approach stemmed from the constraints encountered at the CAAB's REC of the GECO project. Due to financial and bureaucratic challenges, it was not feasible to install the BESs at the prosumer sites within the REC.

The BES model used in the SIL validation, while effective in certain respects, fell short in fully capturing the dynamics and harmonic content of real inverters. Moreover, it could not adequately simulate the complexities that may emerge when establishing regular communication between the EMS and the physical BESSs. Thus, the PHIL testing at SGEVL was not just a technical exercise but an important proof of concept.

Envisioning the BESS installed at the REC's CAAB, this experiment raised a pivotal question: Could we, from the LISEP's workstations, remotely control the BESS via the proposed EMS? This scenario was instrumental in demonstrating the practical viability and adaptability of the EMS in real-world settings. This initiative aimed to bridge the gap between conceptual models and tangible applications, ensuring that the EMS could meet the dynamic requirements of an operational REC.

The initial phase of the project involved integrating the OPAL-RT simulator, the power amplifier, and the battery systems to assess whether the EMS would perform as anticipated. This verification was conducted by running simulations using historical data, allowing for a controlled test of the system's capabilities.

Once the PHIL setup was established and a robust communication protocol between the various components was put in place, the project progressed to the next stage: conducting real-time simulations using real-time field data. This step was vital for testing the BES response in dynamic conditions, mirroring real-world scenarios where setpoints and system conditions change continuously. The real-time simulations were designed to challenge the EMS, verifying its ability to respond accurately and efficiently to live data inputs and demonstrating its potential for practical application in managing energy systems.

8.1 Real-Time PHIL Experimental Setup

The Low Voltage (LV) microgrid at the SGEVL facilities at INESC TEC is characterized by its versatility and the variety of test bed configurations it offers. This microgrid is essentially composed of two three-phase LV microgrids that can operate in parallel, managed and controlled by a SCADA (Supervisory Control and Data Acquisition) system. Each microgrid is equipped with a range of appliances, including domestic and controllable loads, three-phase induction motors, EV charging stations, a LV cable simulator, two BESs and a three-phase power amplifier.

The power amplifier interfaces with the real-time digital simulator to seamlessly integrate physical power hardware with the simulated virtual network. This setup allows for testing and experimentation with a variety of configurations, providing a realistic environment for the study and development of both software and hardware solutions. A schematic representation of the infrastructure enabling PHIL simulations is shown in Figure 65 while the user interface of the microgrid control system is shown in Figure 66.

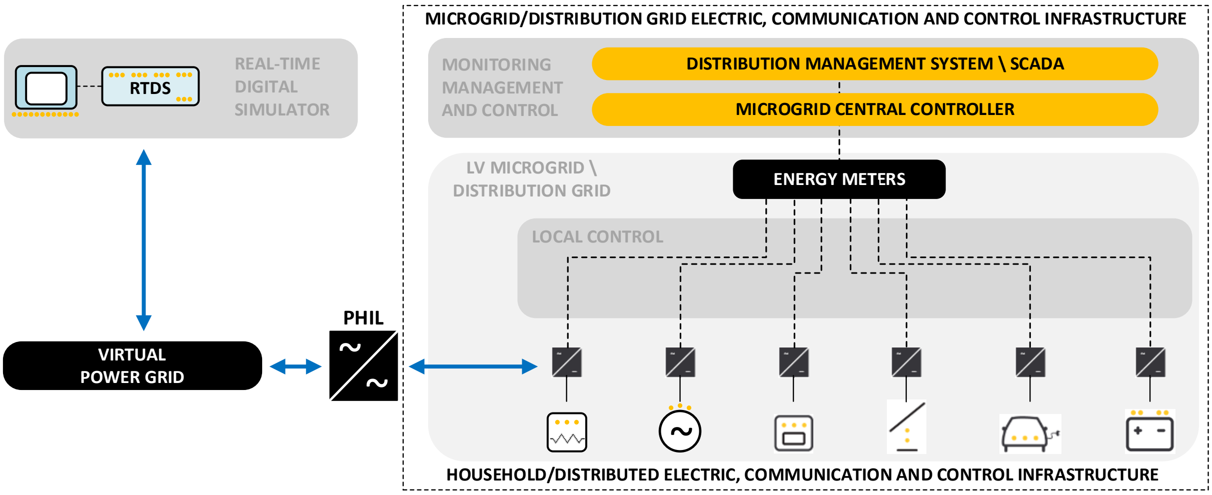

Figure 65. Schematic diagram of the microgrid infrastructure, its control system and how it can be interfaced to the digital environment to perform PHIL simulations.

The configuration that suited our requirements included the real-time simulator, specifically an OPAL-RT 5600, interfaced with a 100 kVA three-phase power amplifier, the EGSTON CSU 100, connected to the microgrid. Additionally, two AddVolt lithium-ion batteries, each with a capacity of 19 kW/34.6 kWh were utilized as well as a variable resistive load, identified as CL1, capable of drawing up to 4.6 kW. This load was employed as a snubber, an important component for stabilizing and protecting a system in which multiple power converters are interfaced.

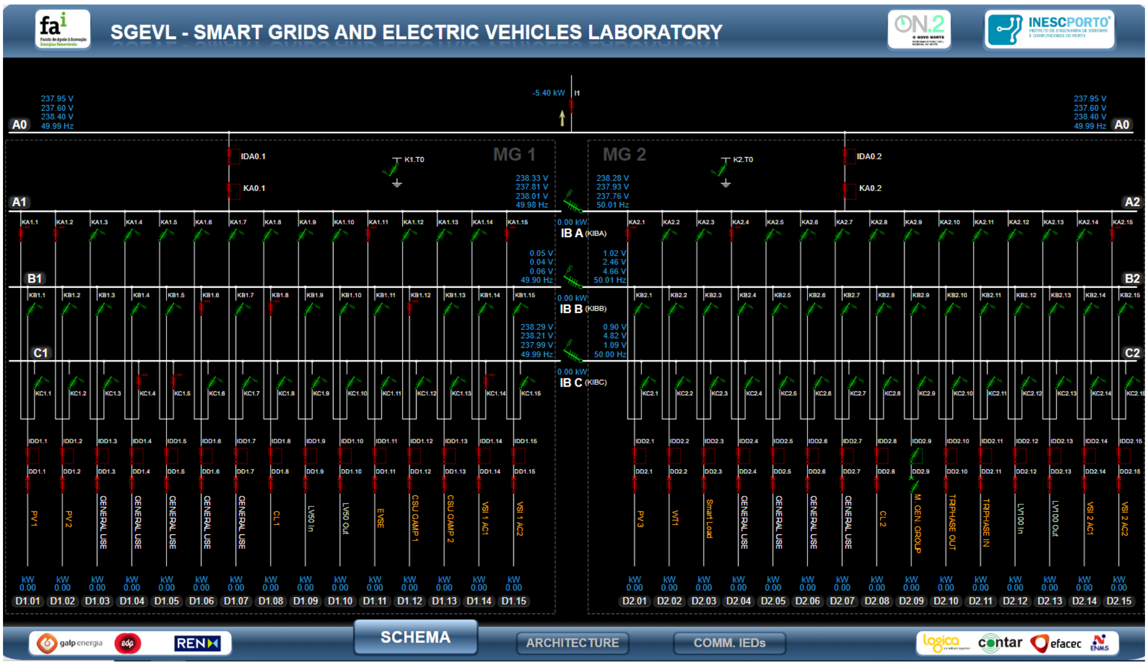

Figure 66. Graphic interface that allows to operate the various switches and connections of the two microgrids.

The conceptual diagram illustrating the test bed setup, enabling the validation of the EMS with BESs in a PHIL configuration, is depicted in Figure 67. The REC network is emulated within the RT-LAB software environment and operated by the EMS, representing the software under test. The EMS controls the BESs that are connected to the microgrid and the snubber. The EMS, OPAL-RT and BESs maintain asynchronous communication through Ethernet, ensuring continuous data flow and control signals. Simultaneously, the power amplifier synchronizes the physical behaviour of the BESs with the virtual network model in real-time, effectively closing the loop between hardware and software simulation. The Lab Device Manager allows to control the power amplifier connections and configuration, it reports any malfunctions and allows to start and stop the simulations.

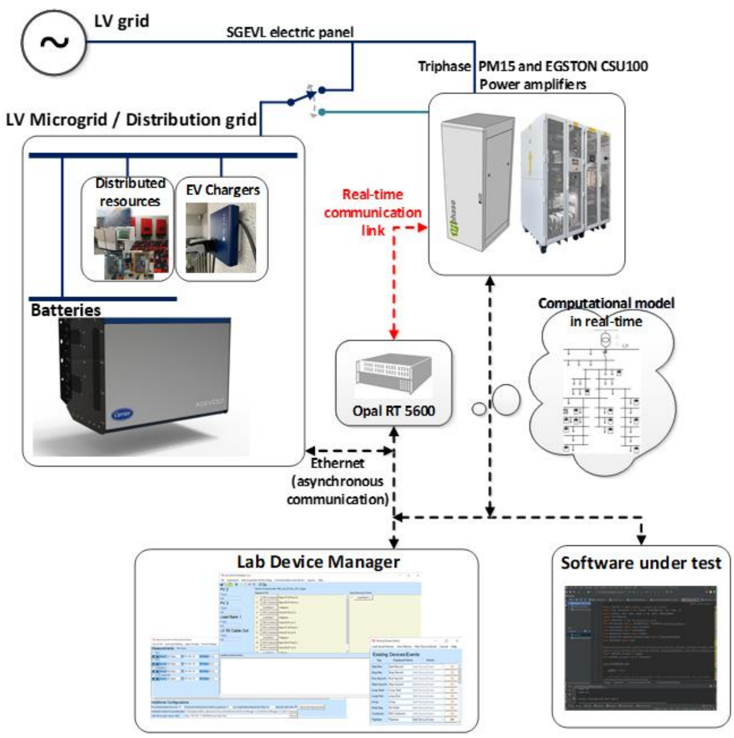

Figure 67. PHIL test bed configuration adopted.

The digital simulator used has an 8 core Intel Xeon CPU running at 3.2 GHz encased in a OP5600 chassis, depicted in Figure 68. The real-time simulation software RT-LAB integrates with the MATLAB/Simulink environment, allowing users to develop and deploy models in real-time. The RT-LAB toolbox in Simulink allows to access the I/O interfaces, interconnecting the digital model with the PHIL testing environment. In particular, two TCP/UDP (Transmission Control Protocol/ User Datagram Protocol) boards have been configured for the transmission and reception of the power setpoints to the BESSs.

Figure 68. OPAL-RT 5600.

As power amplifier, the EGSTON CSU 100-1GAMP4 in the three-phase plus neutral operation mode was used. A picture of it is shown Figure 69. The manufacturer provides a Simulink model of it, which, integrated in the REC model allows to interface it with the microgrid.

Figure 69. EGSTON CSU 100-1GAMP4 power amplifier.

Two AddVolt lithium-ion battery pack were available in the lab, these use a Nickel Manganese Cobalt (NMC) chemistry, have a power rating of 19 kVA, an energy capacity of 34.6 kWh and a weight just shy of 400 kg. A picture of one of them is shown in Figure 70. These battery packs are originally designed to power refrigerated trucks for food chain logistic and are being repurposed for smart cities applications such as that of the POCITYF project. AddVolt batteries are connected to the Ethernet and can be managed either via an online dashboard or through an API.

Figure 70. AddVolt lithium-ion battery pack. Power rating of 19 kVA, energy capacity of 34.6 kWh. Pallet for scale.

The API uses a token authentication system, where the token must be included as a query parameter in all performed requests. Two types of requests are possible through the API, either “get” or “post”, that allow to manage “deals” with the BESS. Through “get” requests is possible to obtain certain battery identifiers, such as ID and GPS position, as well as important system data such as the battery SOC. Through “post” requests is possible to execute certain OTA (Over The Air) tasks, such as turning on and off the battery’s inverter and setting active and reactive power setpoints.

```python
def authenticate1():
    global authenticated1
    # Authentication URL with token
    auth_url1 = 'https://api.addvolt.com/api/v1/deal/903?token=ota-                                    '
    try:
        response = requests.get(auth_url1)
        if response.status_code == 200:
            # Authentication successful
            authenticated1 = True
            print('BESS battery: Authentication successful')
        else:
            print('BESS battery: Authentication failed')
    except requests.exceptions.RequestException as e:
        print('Error:', e)


def send_to_api1(data1):
    # Check if authentication is done
    if not authenticated1:
        # Authenticate using the authentication URL
        authenticate1()

    # Continue with the original send_to_api logic
    # API endpoint URL
    api_url1 = 'https://api.addvolt.com/api/v1/deal/903/task?token=ota-                                    '

    # JSON payload
    payload1 = {
        "task_definition": {
            "name": "set-parameter",
            "parameter": "active-power",
            "value": data1
        }
    }
```

Figure 71. Functions of the phyton script that establish a communication with the BES and send the active power setpoint, namely “data1”, to AddVolt battery pack “903”.

A Python script was developed to manage the communication between the OPAL-RT TCP ports and the batteries’ API. This script is always listening to the TCP ports, as soon as it receives a power setpoint, it initiates a connection with the BES using an authentication function. Following a successful connection, it proceeds to execute a “deal” transaction, sending a command to "set-parameter" for "active-power" to a specified value, referred to as "data1". Whether or not the instruction has been successfully received, it is promptly communicated in the command window. This process exemplifies the script's capability to effectively communicate and dynamically control the BESS power output. In Figure 71, the functions responsible for setting the power setpoint of AddVolt battery pack “903” are shown. For security and privacy reasons the authentication token has been redacted.

When the real-time simulation is successfully running the Python script command window would print, every minute, a message like the following:

Server listening on 162.198.1.187:23000 and 162.198.1.187:23001
BESS setpoint: 2985 W
BESS battery: Authentication successful
BESS setpoint successfully sent to AddVolt API
BESS setpoint updated

Where 162.198.1.187 is a fictitious IP of the workstation and 23000 and 23001 are the TCP ports of the OPAL RT.

8.2 PHIL simulations results

As anticipated, the initial phase of the PHIL testing campaign focused on integrating the OPAL-RT simulator, the power amplifier, and the battery systems. The objective was to verify that the experimental setup, including the communication protocol and the EMS, would function as expected.

To achieve this, the simulation of historical data was performed, providing a realistic and controlled environment to assess the system’s performance. The use of historical data served as a benchmark, allowing the team to evaluate the performance of the system against known outcomes. Moreover, this phase was crucial for testing the communication flow between the system's hardware and software components.

The REC’s network tested is a simplified version of the CAAB’s REC discussed in Section 7.2, it includes 3 of the 5 members of the community, two of the consumers and the prosumer. The two consumers emulate the load demand of the cold room storage and the office space, metered by device ID 2080 and 2517 reported in Table 19, respectively. The prosumer pegs the load consumption and PV production of the NILM 348 as well as the behavior of the envisioned BESS as controlled by the EMS. In the PHIL representing the prosumer of the REC, beyond the BESS, also the PV production and load consumption have been emulated, aggregating them, by a battery pack.

The model diagram of the REC, as implemented in Simulink, is shown in Figure 72. The ideal source on the left represents the distribution grid, the top branch represents the prosumer and it integrates the model of the power amplifier which interfaces with the BES and the microgrid, ultimately enabling the PHIL configuration. The two bottom branches represent the model of the consumers and emulate their load consumption. When PV production is null and the load draws power, the battery pack recharges from the microgrid. When the sum of PV production and load consumption is positive, the battery pack discharges into the microgrid.

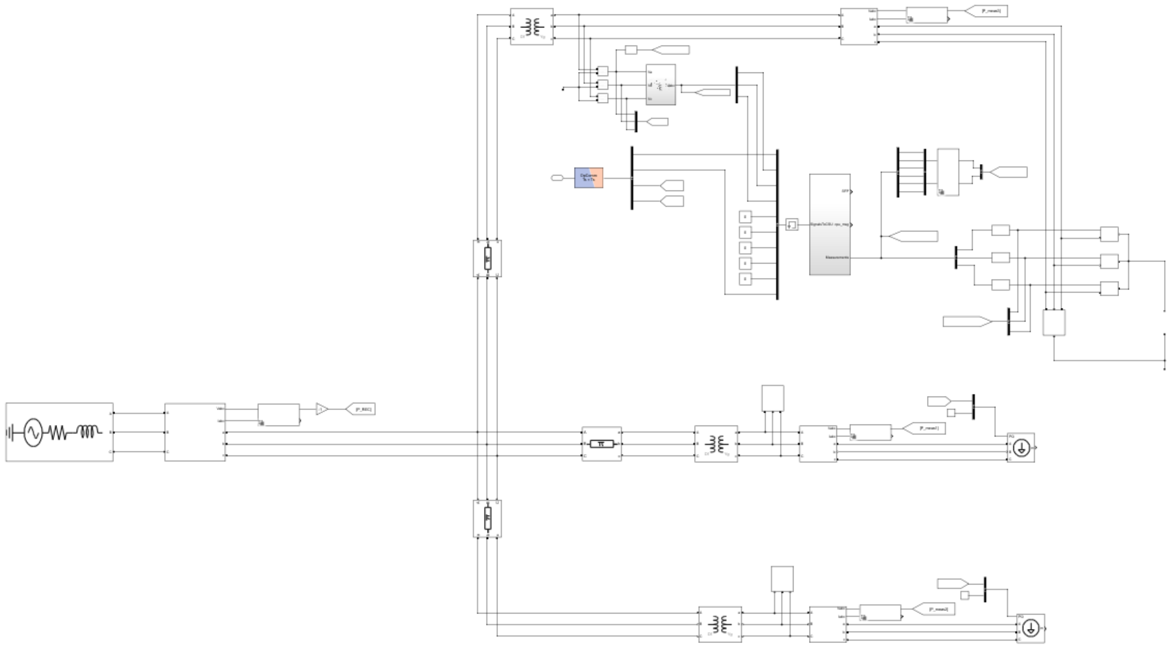

Figure 72. Simulink model of a reduced version of CAAB's REC, the top branch represents the PHIL integrating AddVolt's battery pack.

To accommodate power consumption constrains and ensure a safety margin, since AddVolt's battery would at times unexpectedly trip if the power setpoint is set higher than 8 kW, the power profiles have been all scaled down by a factor of 10. This precautionary measure was essential to avoid overloading the battery pack and to ensure safe and prolonged operation during the real-time testing phases. The input profiles, as recorded the 27th of March 2023, are shown in Figure 73. Power drawn from the grid is shown as negative while power injected into it is shown as positive. The load consumption of the two consumers is aggregated into "Office plus Cold Room", in blue. The prosumer own load is indicated as "Shared Load", in red, the PV production is depicted in yellow and the BESS profile in green. Even though the simulated data was recorded a few months in advance, the simulation was performed in real-time, meaning that it was not accelerated and 1 minute of simulation corresponded to 1 minute of data. For this reason, 50 minutes of real-time data were simulated, from 17:30 to 18:20, when the simulation had to be stopped because of a "dew point" alert shown by the power amplifier, basically too much condensation accumulated over time in the cooling system of the amplifier. The simulated time window is framed in the graph by two black dashed lines. This time frame has been selected because in it the PV production gradually fades out and the BES begins to power the community.

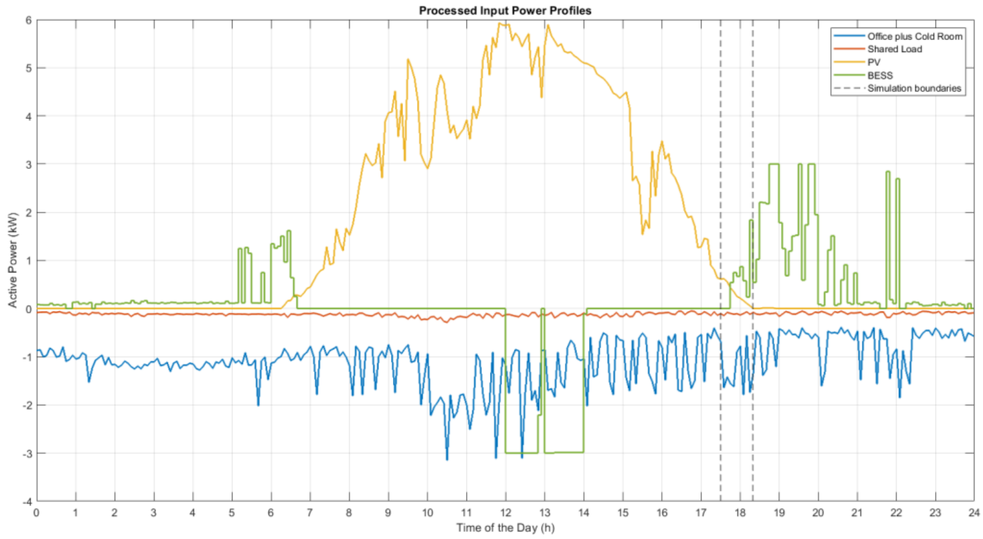

Figure 73. Scaled down data recorded the 27th of March 2023 and used to tune the PHIL setup.

The resulting power profile of the prosumer and thus that of the PHIL branch, obtained by aggregating PV power profile, shared load, and BESS is shown in Figure 74. A zoomed in version of it is reported in Figure 75.

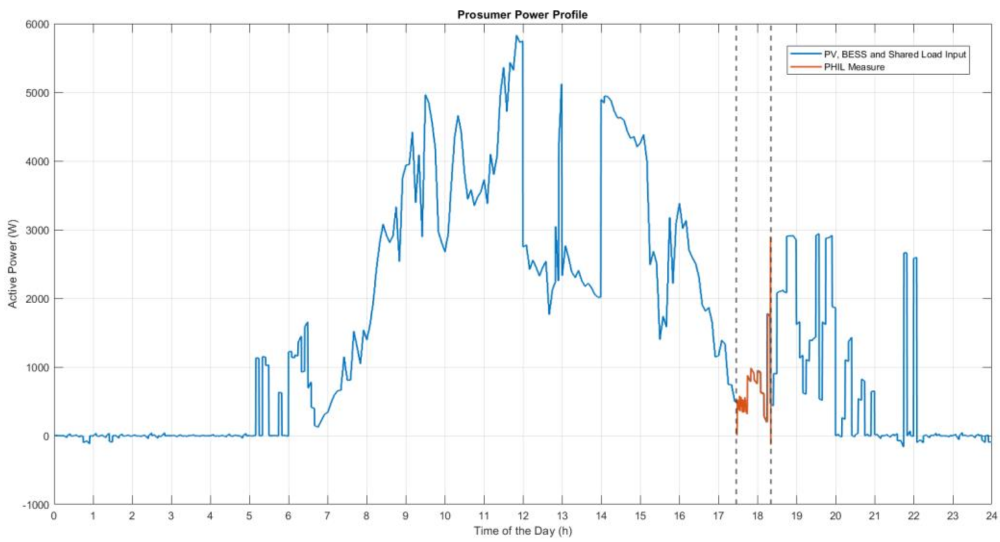

Figure 74. Prosumer aggregated active power profile, in blue, and active power measured in the PHIL branch, in red.

It can be noted how the power injected into the microgrid by the PHIL, shown in red, closely matches that of the expected power profile, shown in blue. It must be noted that to interface the power amplifier and the battery packs a snubber load must always be present. This resistive load, connected to microgrid 1 and named CL1, has been set to draw approximately 3000 W at the nominal voltage and damps excessive voltage surges in a system where an elevated inductance and multiple switching components coexist. The snubber is fed by the battery pack emulating the BES and its power consumption has been accounted for in all the following plots.

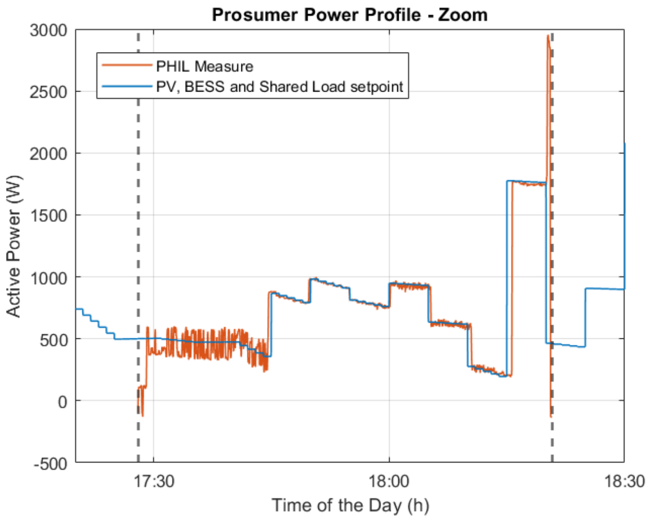

Figure 75. Prosumer aggregated active power profile, in blue, and active power measured in the PHIL branch, in red. Zoomed in version.

For this reason, even when the BES appears to be injecting no power it is actually feeding the snubber. That is why the first part of the measured active power of the PHIL is noisier, the PV and BES batteries inverters are resonating with each other and then at around 17:40 the PV fades out.

Furthermore, in Figure 75 the different time resolution of the two power profiles is notable, on the left, before of the start of the PHIL simulation, the PV power curve is updated every minute. On the right, the BESS setpoint, calculated by the EMS, has a time resolution of 5 minutes. The load consumption profiles of the consumers, as emulated by the REC's Simulink model, are not reported as they perfectly match the input data.

In Figure 76, the BES active power setpoint and its actual value during the simulation, disaggregated by the rest of the prosumer, are shown. Besides the initial noise and the final switching off transient, the two closely match. These aspects could not be appreciated in the

SIL simulation of Chapter 7, where all the power setpoints were ideally matched by the BES, and it is one of the nuanced considerations that the PHIL allows to appreciate.

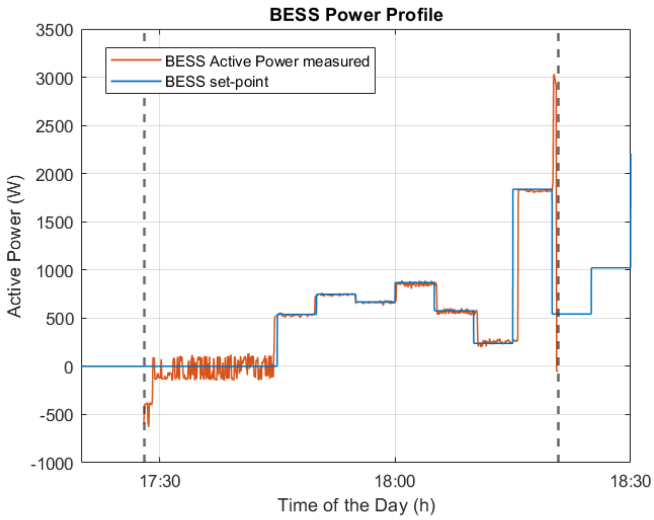

Figure 76. BES active power profile, in blue, and active power measured in the PHIL branch, in red. Zoomed in version.

Another aspect that the SIL was not able to capture was that regarding the reacting power. As of right now the proposed EMS does not envision reactive power compensation and its setpoint is set to zero. In Figure 77, the reactive power measured along the PHIL branch is reported, due to presence of inductive filters its value is just above 200 Var.

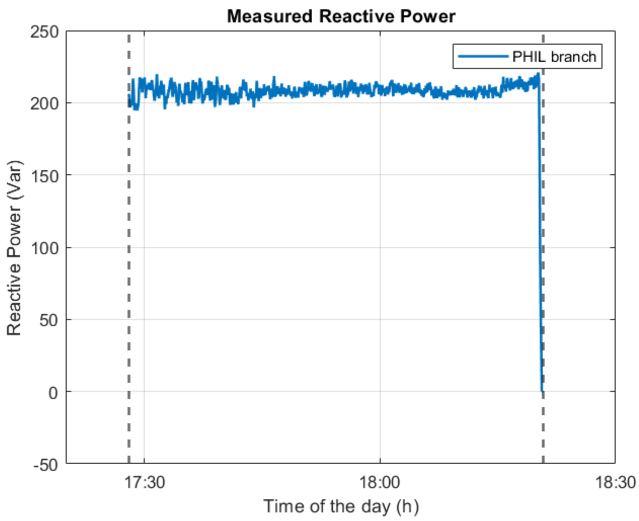

Figure 77. Reactive power measured along the PHIL branch.

8.2.1 *Real-time PHIL simulations results*

The simulation using historical data was instrumental in tuning the PHIL setup and ensuring that the API communication protocol with the AddVolt batteries ran smoothly. Transitioning to the real-time simulation, the REC's model of Figure 72, besides some measurement probes, is kept unchanged, the difference resides in the data sourcing. In Bologna, the NILM devices need to consistently upload in real-time their measurements to the online database, which sometimes proves to be challenging. These measurements are then accessed by the EMS through the OVPN, the data is downloaded, and the optimization algorithm calculates and updates the BES setpoint every $T_{forecast}$. Once processed, this data is scaled appropriately and sent to both the AddVolt batteries, simulating the prosumer within the REC, and to the REC's model in the OPAL-RT, simulating the consumers. This process can introduce, in the case of the battery power packs, some time-delays, typically no longer than 30 seconds. Which, considering that the BES setpoint has a time resolution of 5 minutes can be regarded as acceptable. In Figure 78, a scheme showing the elements of the simulation and how are they interfaced is shown.

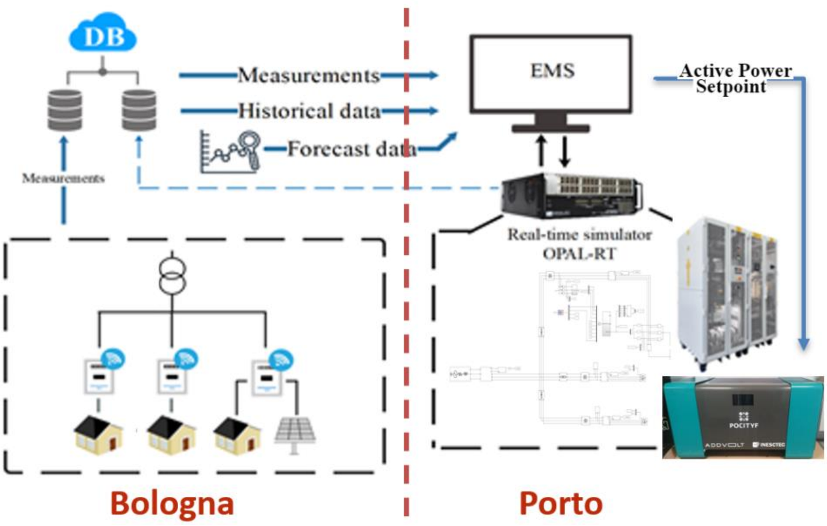

Figure 78. Conceptual diagram of the PHIL real-time simulation.

Due to stringent time constrains and some technical difficulties, a successful run was achieved on the 28th of July 2023 and approximately 90 minutes of data have been recorded between 15:50 and 17:20, Italian time. The measurements uploaded by NILM devices to the emoncms database, scaled by a factor of 10, are shown in Figure 79 from midday to 6 pm. As in the simulation of the historical data, the load consumption of office and cold room have been aggregated, the load of the prosumer is named “Shared Load” and the power production of NILM’s 348 PV plant is shown in yellow as “PV”.

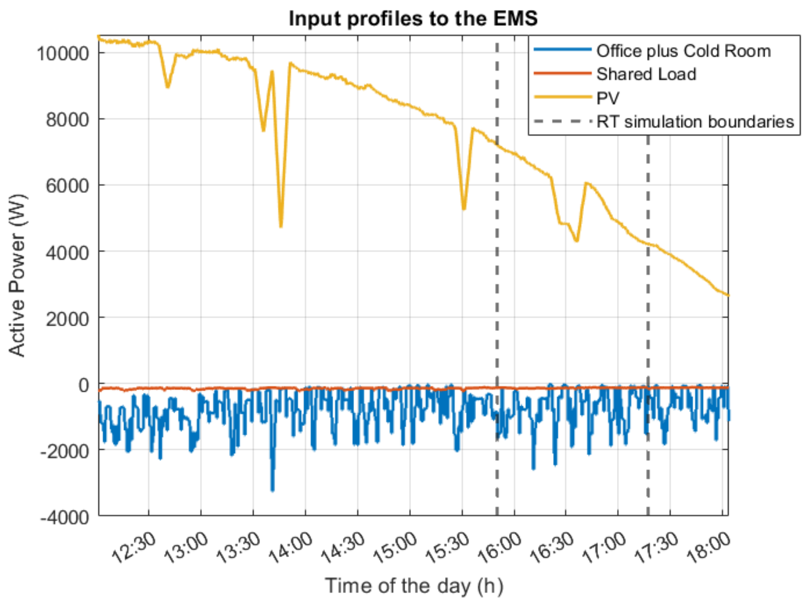

Figure 79. NILM’s measures as uploaded to the online database on the 28th of July 2023.

In Figure 80, the active power setpoints of the PV and the BES of the prosumer, as sent to battery packs, as well as their measurement along the PHIL branch, are shown. A zoomed in version of the BES setpoint is reported in Figure 81.

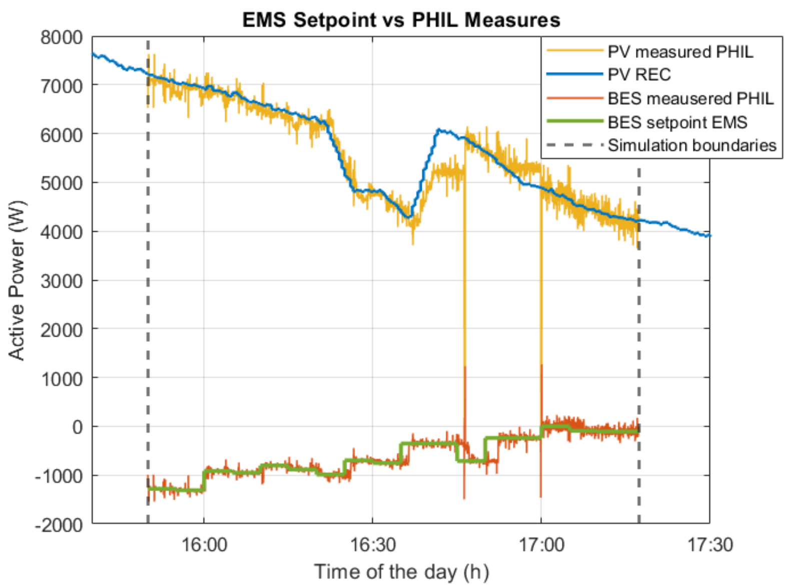

Figure 80. PV and BESS setpoint as sent to the battery packs and as measured along the PHIL branch, run of the 28th of July 2023.

As multiple switching components are interfaced the measurements are quite distorted, however the overall shape follows quite closely the setpoint. As anticipated, the setpoint sent through the API is sometimes received with some delay, and at around 16:40 and 16:50 the API failed to communicate the new setpoint to the battery packs which remained stuck at the previous value. Besides these minor issues we can deem this run quite successful.

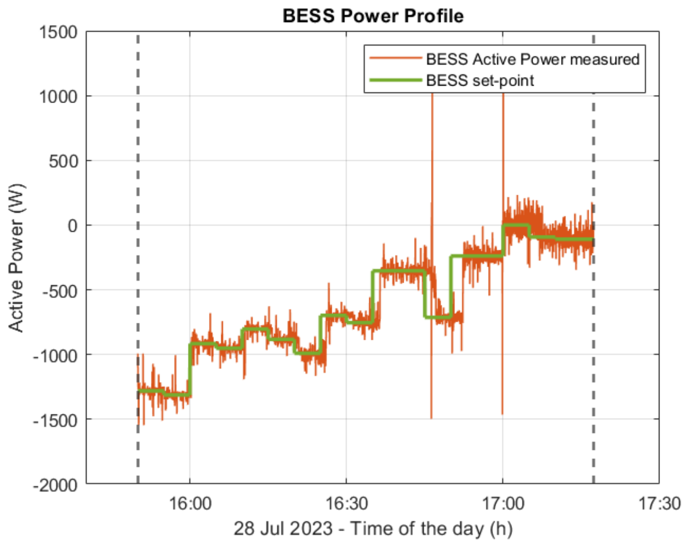

Figure 81. BESS setpoint as determined by the EMS and as measured along the PHIL branch, run of the 28th of July 2023.

Due to the voltage-dependent nature of the power absorbed by the resistive snubber, i.e., $P = V^2/R$, which was accounted for in all the previous graphs, the voltage along the PHIL branch has been monitored to ensure that any changes in load absorption would not pass unnoticed. Its value is shown in p.u. in Figure 81, on average it is constant and just a few thousandths of a percent above its nominal value. The snubber load consumption is than considered constant and measured at a value of around 2950 W.

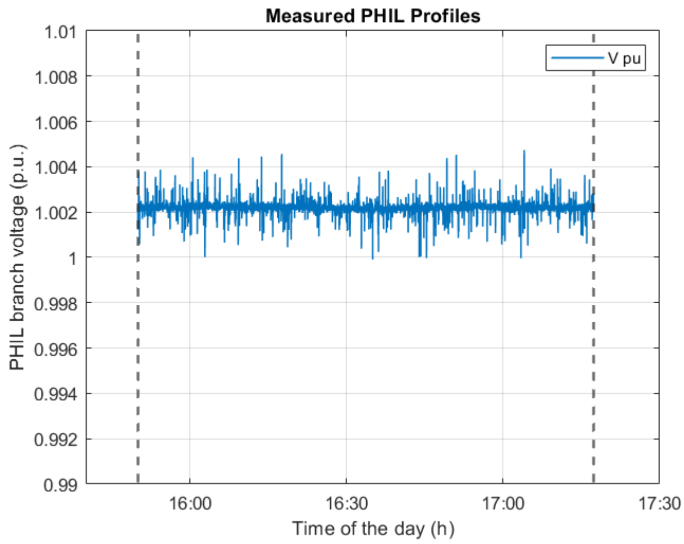

Figure 82. Voltage in p.u. of the PHIL branch, run of the 28th of July 2023.

Following the footsteps of the historical data simulation, in Figure 83, the reactive power measured along the PHIL branch is reported and, similarly to the case of the historical data simulation, its average value it is found to be at approximately 200 Var.

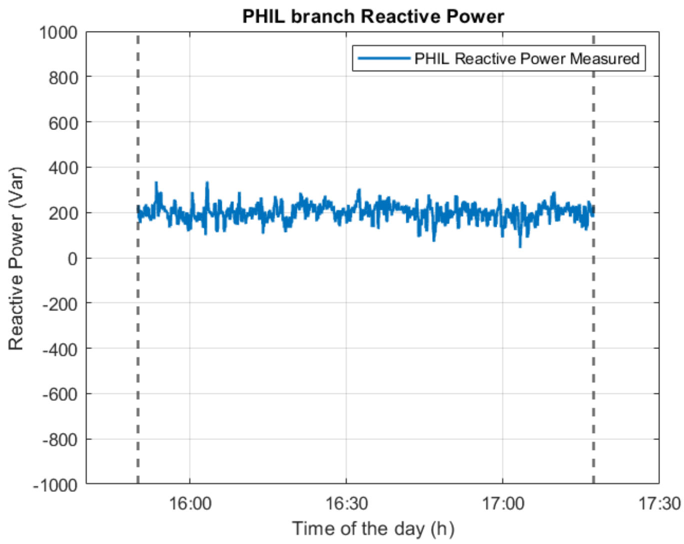

Figure 83. Reactive power as measured along the PHIL branch, run of the 28th of July 2023.

In conclusion, the PHIL testing at the SGEVL at INESC TEC successfully demonstrated the practical applicability and robustness of the EMS within a real-world context. The PHIL test bed helped us move from theoretical models and simulations to a tangible, operational framework with all its technical difficulties. It addressed key challenges, especially in the real-time data transfer and synchronization and validated the EMS's capacity to adapt to and manage the complexities of an, albeit simplified, real-world REC.

The testing proved that the EMS could effectively interface with a physical BESS, navigating the challenges of real-time communication and control. This was showcased by a few hours-long runs integrating OPAL-RT simulator, power amplifier, and battery systems under both historical data simulation and real-time field data conditions.

A key aspect of the AddVolt battery pack employed in the PHIL validation is its ability to be remotely managed through an API. This feature significantly enhances the flexibility and scalability of the EMS. The physical location of the BESS becomes irrelevant for operational purposes, as long as there is a reliable communication link.

In our test, the BESS were located at the SGEVL for monitoring and validation purposes. This was necessary to ensure a secure operation and allow for a close monitoring of the communication protocol and of the BESS's performance in a controlled environment. However, once the system's functionality and the communication protocol were validated, the BESS could theoretically be deployed at any location, such as the CAAB's REC of the GECO project.

This capability to remotely control the BESS via an API is a significant advantage. It means that the BESS can be installed directly at the REC or at any other suitable location, without the need for physical proximity to the EMS.

However, expanding on the robustness of the distributed management system, particularly focusing on its continuous updating of the online measurement database, it's important to recognize that this aspect represents one of the weak links of the system's architecture. The continuous update process is crucial for real-time decision-making and efficient operation of the EMS, but it also introduces several challenges and vulnerabilities. For real-world applications, it is crucial that the EMS operates continuously, ideally leveraging an offline measurement system. This approach mitigates reliance on internet connectivity, which, as evidenced in our tests, can sometimes be intermittent and unreliable. Implementing the EMS on a microcontroller installed onsite within the REC would provide a more robust and reliable solution and it is within the scope of future developments.

Chapter 9. Conclusions

This thesis develops and examines two distinct yet interconnected aspects of modern power systems and their integration of renewable energy sources. The first part, centered around the frequency stability at the production and transmission side of the electric power system, introduces a control architecture enabling wind power plants and grid-scale battery energy storage systems to provide synthetic inertial response. The second part advances the operational management of Renewable Energy Communities (RECs), proposing and rigorously testing an Energy Management System (EMS) through both Software-in-the-Loop (SIL) and Power Hardware-in-the-Loop (PHIL) configurations, leveraging real-time field data.

The initial part of the thesis is centered around the production and transmission side of the electric power system, with a specific focus on wind farms and grid-scale battery energy storage systems. This includes both stand-alone storage and integrated systems designed to mitigate the variability and intermittency of RES. A coordinated control scheme is presented, enabling wind turbines to emulate the inertial response exhibited by traditional synchronous generators. This emulation control scheme provides simultaneous access to both the kinetic energy of wind turbines and the electrostatic energy stored in their back-to-back converters' DC-links. By strategically controlling these energy reserves in response to fluctuations in network frequency, wind farms can support the power grid with inertial response. The coordinated control scheme is firstly tested on a modified version, which incorporates a model of a wind farm, of the two-areas four-generators benchmark test network, firstly presented by Kundur. The simulations highlight the contribution to both the small-signal stability and the transient stability of the coordinated control scheme. Secondly, the frequency support control is tested on a larger, real, transmission grid: the Sicilian network. This is done on a wide range of operating conditions of two forecasted scenarios. These forecasts, one for the year 2030 and one for the year 2050, encompass considerations for both the configuration of the network and the variety and quantity of generation capacity installed. This is accomplished once again via a sensibility analysis that evaluates the dampening of the main oscillation modes and large transient phenomena. The findings emphasize the need for flexibility options in power systems with a high penetration of converter-interfaced resources, especially to damp low frequency inter-area modes, with the proposed control scheme standing out as a viable solution.

The second part of the thesis shifts its focus to the consumption and distribution side of the grid, specifically to RECs. These communities, comprised of prosumers and consumers, collaborate to share renewable energy, minimizing dependence on the Distribution System Operator (DSO). An EMS is introduced to control the BES assets within the REC. Operating in Real-Time (RT), the EMS considers forecasted energy production from PV systems, historical and forecasted load consumption, and the hourly day-ahead energy prices set by the national energy market. The objective function of the EMS minimizes the energy procurement costs for the REC by maximizing the renewable energy shared within its members. It does that by considering a rolling time window of a few days in which it determines the optimal BESs active power set-points. This optimization algorithm has been tested using both SIL and PHIL techniques.

The validation process incorporated two RECs case studies, revolving around the *Climate-KIC* pilot project named GECO, and utilizing real-world metered data. These studies showcased the EMS's performance and reliability, displaying its applicability in managing and optimizing energy resources within REC. The EMS's effectiveness is further evidenced in the real-time simulation test bed set up at the Smart Grid and Electric Vehicle Lab (SGEVL), which played a pivotal role in its validation. Providing valuable insights into the real-world practical applications of the EMS.

The EMS's design is versatile, allowing it to operate effectively with both historical and live measurement data, which underscores the significance of the online distributed measurement system and the communication protocol with the BES as potential points of vulnerability. The PHIL simulations were instrumental in testing the real-time controllability of the BES. In contrast, the real-time SIL simulations played a critical role in strengthening the communication protocols for the online database, which stores real-time load and PV measurements.

One of the challenges highlighted through these tests is the establishment of a robust and reliable online metering network that operates continuously. The dependency on accurate forecast data becomes critical when part of the distributed measurement network is offline. In practical applications, a more resilient solution would involve integrated measurement devices for each system component, coupled with an offline communication network. This network would ensure the continuous feed of data to the EMS hub and effectively redistribute the BES power set-points across the various prosumers within the REC.

The core algorithm of the EMS, along with its forecast accuracy, is being continuously refined and adapted to align with the evolving regulatory landscape in Italy and other European countries. This adaptability is crucial in responding to legislative changes and ensuring the EMS's relevance and effectiveness across different regions. A scaled-down version of the PHIL test bed setup is planned for replication at LISEP, which will facilitate further research and development. This includes incorporating load control features and addressing additional technical aspects, such as stability constraints

Overall, the extensive testing and validation of the EMS, encompassing both SIL and PHIL approaches, not only affirm its effectiveness in real-world scenarios but also highlight areas for further development, particularly in enhancing the resilience and reliability of the metering and communication infrastructure.

Chapter 10. Bibliography

[1] US National Academy of Engineering's, Top 20 Engineering Achievements (retrieved the 6th of June 2023 on www.greatachievements.org)

[2] Gielen, D., Gorini, R., Leme, R., Prakash, G., Wagner, N., Janeiro, L., ... & Saygin, D. (2021). World energy transitions outlook: 1.5° c pathway.

[3] Guerra, K., Haro, P., Gutiérrez, R. E., & Gómez-Barea, A. (2022). Facing the high share of variable renewable energy in the power system: Flexibility and stability requirements. Applied Energy, 310, 118561.

[4] Mehigan, L., Al Kez, D., Collins, S., Foley, A., Ó'Gallachóir, B., & Deane, P. (2020). Renewables in the European power system and the impact on system rotational inertia. Energy, 203, 117776.

[5] Tielens, P., & Van Hertem, D. (2016). The relevance of inertia in power systems. Renewable and sustainable energy reviews, 55, 999-1009.

[6] Morren, J., De Haan, S. W., Kling, W. L., & Ferreira, J. A. (2006). Wind turbines emulating inertia and supporting primary frequency control. IEEE Transactions on power systems, 21(1), 433-434.

[7] Kushwaha, P., Prakash, V., Bhakar, R., & Yaragatti, U. R. (2022). Synthetic inertia and frequency support assessment from renewable plants in low carbon grids. Electric Power Systems Research, 209, 107977.

[8] Machowski, J., Lubosny, Z., Bialek, J. W., & Bumby, J. R. (2020). Power system dynamics: stability and control. John Wiley & Sons.

[9] Meeus, L., & Nouicer, A. (2018). The EU clean energy package.

[10] European Union, "Directive UE 2018/2001 on the promotion of the use of energy from renewable sources," 2018.

[11] "Comunità energetiche rinnovabili": sistemi realizzati da clienti finali ai sensi dell'articolo 31 del decreto legislativo n.199 del 2021; (Available online at www.normattiva.it/uri-res/N2Ls?urn:nir:stato:decreto.legislativo:2021;199~art31. Retrieved the 29th of January 2024)

[12] Cunha, F. B. F., Carani, C., Nucci, C. A., Castro, C., Silva, M. S., & Torres, E. A. (2021). Transitioning to a low carbon society through energy communities: Lessons learned from Brazil and Italy. Energy Research & Social Science, 75, 101994.

[13] Lowitzsch, J., Hoicka, C. E., & van Tulder, F. J. (2020). Renewable energy communities under the 2019 European Clean Energy Package–Governance model for the energy clusters of the future?. Renewable and Sustainable Energy Reviews, 122, 109489.

[14] S. Lilla, C. Orozco, A. Borghetti, F. Napolitano, and F. Tossani, "Day-Ahead Scheduling of a Local Energy Community: An Alternating Direction Method of Multipliers Approach," *IEEE Trans. Power Syst.*, vol. 35, no. 2, pp. 1132–1142, 2020.

[15] M. Tostado-Véliz, A. Rezaee Jordehi, D. Icaza, S. A. Mansouri, and F. Jurado, "Optimal participation of prosumers in energy communities through a novel stochastic-robust day-ahead scheduling model," *Int. J. Electr. Power Energy Syst.*, vol. 147, May 2023.

[16] C. Orozco, A. Borghetti, F. Napolitano, and F. Tossani, "Multistage day-ahead scheduling of the distributed energy sources in a local energy community," in *2020 IEEE International Conference on Environment and Electrical Engineering and 2020 IEEE Industrial and Commercial Power Systems Europe, EEEIC / I&CPS Europe 2020*, 2020.

[17] C. Orozco, A. Borghetti, B. De Schutter, F. Napolitano, G. Pulazza, and F. Tossani, "Intra-day scheduling of a local energy community coordinated with day-ahead multistage decisions," *Sustain. Energy, Grids Networks*, vol. 29, 2022.

[18] Y. Zhou, Z. Wei, G. Sun, K. W. Cheung, H. Zang, and S. Chen, "A robust optimization approach for integrated community energy system in energy and ancillary service markets," *Energy*, vol. 148, pp. 1–15, 2018.

[19] M. J. Rana, F. Zaman, T. Ray, and R. Sarker, "Real-time scheduling of community microgrid," *J. Clean. Prod.*, vol. 286, 2021.

[20] N. Liu, Q. Tang, J. Zhang, W. Fan, and J. Liu, "A hybrid forecasting model with parameter optimization for short-term load forecasting of micro-grids," *Appl. Energy*, vol. 129, pp. 336–345, Sep. 2014.

[21] H. S. Hippert, C. E. Pedreira, and R. C. Souza, "Neural Networks for Short-Term Load Forecasting: A Review and Evaluation," *IEEE Trans. Power Syst.*, vol. 16, no. 1, 2001.

[22] Hatziargyriou, N., Milanovic, J., Rahmann, C., Ajjarapu, V., Canizares, C., Erlich, I., ... & Vournas, C. (2020). Definition and classification of power system stability–revisited & extended. IEEE Transactions on Power Systems, 36(4), 3271-3281.

[23] P. Kundur, *Power System Stability and Control*. New York: McGraw-Hill, 1994.

[24] Gonzalez-Longatt, F., & Torres, J. L. R. (Eds.). (2018). Advanced smart grid functionalities based on powerfactory (p. 371). Cham, Switzerland: Springer International Publishing.

[25] Anaya-Lara, O., Jenkins, N., Ekanayake, J. B., Cartwright, P., & Hughes, M. (2011). Wind energy generation: modelling and control. John Wiley & Sons.

[26] Kazachkov, Y. A., Feltes, J. W., & Zavadil, R. (2003, July). Modeling wind farms for power system stability studies. In 2003 IEEE Power Engineering Society General Meeting (IEEE Cat. No. 03CH37491) (Vol. 3, pp. 1526-1533). IEEE.

[27] De Oliveira, R. V., Zamadei, J. A., Cardoso, M. A., & Zamodzki, R. (2012, July). Control of wind generation units based on doubly-fed induction generator for small-

signal stability enhancement. In 2012 IEEE Power and Energy Society General Meeting (pp. 1-8). IEEE.

[28] J. F. Medina Padrón and A. E. Feijóo Lorenzo, “Calculating steady-state operating conditions for doubly-fed induction generator wind turbines,” IEEE Trans. Power Syst., vol. 25, no. 2, pp. 922–928, 2010.

[29] Manwell, J. F., McGowan, J. G., & Rogers, A. L. (2010). Wind energy explained: theory, design and application. John Wiley & Sons.

[30] H. Wang and F. Blaabjerg, “Reliability of capacitors for DC-link applications in power electronic converters - An overview,” IEEE Trans. Ind. Appl., vol. 50, no. 5, pp. 3569–3578, 2014

[31] B. Singh, B. N. Singh, A. Chandra, K. Al-Haddad, A. Pandey, and D. P. Kothari, “A review of three-phase improved power quality ac-dc converters,” IEEE Trans. Ind. Electron., vol. 51, no. 3, pp. 641–660, 2004

[32] E. Rakhshani and P. Rodriguez, “Inertia Emulation in AC / DC Interconnected Power,” Ieee Trans. Power Syst., vol. 32, no. 5, pp. 3338–3351, 2017.

[33] A. Bolzoni and R. Perini, “Feedback Couplings Evaluation on Synthetic Inertia Provision for Grid Frequency Support,” IEEE Trans. Energy Convers., vol. 8969, no. c, pp. 1–1, 2020.

[34] S. Wang, J. Hu, X. Yuan, and L. Sun, “On Inertial Dynamics of Virtual-Synchronous-Controlled DFIG-Based Wind Turbines,” IEEE Trans. Energy Convers., vol. 30, no. 4, pp. 1691–1702, 2015.

[35] Merai, M., Naouar, M. W., Slama-Belkhodja, I., & Monmasson, E. (2019). Grid connected converters as reactive power ancillary service providers: Technical analysis for minimum required DC-link voltage. Mathematics and Computers in Simulation, 158, 344-354.

[36] Y. Wang, Y. Wang, S. Z. Chen, G. Zhang, and Y. Zhang, “A simplified minimum DC-link voltage control strategy for shunt active power filters,” Energies, vol. 11, no. 9, p. 2407, Sep. 2018.

[37] Y. Tang, Y. F. Chen, Y. M. Chen, and Y. R. Chang, “DC-Link Voltage Control Strategy for Three-Phase Back-to-Back Active Power Conditioners,” IEEE Trans. Ind. Electron., vol. 62, no. 10, pp. 6306–6316, 2015

[38] Z. Wu, W. Gao, T. Gao, W. Yan, H. Zhang, S. Yan, and X. Wang, “State-of-the-art review on frequency response of wind power plants in power systems,” J. Mod. Power Syst. Clean Energy, vol. 6, no. 1, pp. 1–16, Jan. 2018.

[39] Y. Li, Z. Xu, and K. P. Wong, “Advanced Control Strategies of PMSG-Based Wind Turbines for System Inertia Support,” IEEE Trans. Power Syst., vol. 32, no. 4, pp. 3027–3037, 2017

[40] S. I. Abouzeid, Y. Guo, and H. C. Zhang, “Dynamic control strategy for the participation of variable speed wind turbine generators in primary frequency regulation,” J. Renew. Sustain. Energy, vol. 11, no. 1, 2019.

[41] Y. Fu, Y. Wang, and X. Zhang, “Integrated wind turbine controller with virtual inertia and primary frequency responses for grid dynamic frequency support,” IET Renewable Power Generation, vol. 11, no. 8. pp. 1129–1137, 2017.

[42] J. M. Mauricio, A. Marano, A. Gómez-Expósito, and J. L. M. Ramos, “Frequency regulation contribution through variable-speed wind energy conversion systems,” IEEE Trans. Power Syst., vol. 24, no. 1, pp. 173–180, 2009.

[43] X. Zhang, X. Zha, S. Yue, and Y. Chen, “A Frequency Regulation Strategy for Wind Power Based on Limited Over-Speed De-Loading Curve Partitioning,” IEEE Access, vol. 6, pp. 22938–22951, 2018.

[44] Mahrouch, A., Ouassaid, M., Cabrane, Z., & Lee, S. H. (2022). De-Loaded Technique Enhanced by Fuzzy Logic Controller to Improve the Resilience of Microgrids Based on Wind Energy and Energy Storage Systems. Energies, 16(1), 291.Díaz-González, F., Sumper, A., & Gomis-Bellmunt, O. (2016). Energy storage in power systems. John Wiley & Sons.

[45] Xu, X., Bishop, M., Oikarinen, D. G., & Hao, C. (2016). Application and modeling of battery energy storage in power systems. CSEE journal of power and energy systems, 2(3), 82-90.

[46] Mostafa, M. H., Aleem, S. H. A., Ali, S. G., Ali, Z. M., & Abdelaziz, A. Y. (2020). Techno-economic assessment of energy storage systems using annualized life cycle cost of storage (LCCOS) and levelized cost of energy (LCOE) metrics. Journal of Energy Storage, 29, 101345.

[47] Kristoff, M. M. (2021). A Grid Dominated by Wind and Solar Is Possible. South Australia: A Window into the Future.

[48] Operator A.E.M. (2018). Initial operation of the Hornsdale power reserve battery energy storage system. Report, April.

[49] G. Mandic, A. Nasiri, E. Ghotbi, and E. Muljadi, “Lithium-ion capacitor energy storage integrated with variable speed wind turbines for power smoothing,” IEEE J. Emerg. Sel. Top. Power Electron., vol. 1, no. 4, pp. 287–295, 2013.

[50] M. F. M. Arani and E. F. El-Saadany, “Implementing virtual inertia in DFIG-based wind power generation,” IEEE Trans. Power Syst., vol. 28, no. 2, pp. 1373–1384, 2013.

[51] Y. Ma, Z. Lin, R. Yu, and S. Zhao, “Research on improved VSG control algorithm based on capacity-limited energy storage system,” Energies, vol. 11, no. 3, 2018.

[52] Dantas, N. K., Souza, A. C., Vasconcelos, A. S., Junior, W. D. A., Rissi, G., Dall’Orto, C., ... & Rosas, P. (2022). Impact analysis of a battery energy storage system connected in parallel to a wind farm. Energies, 15(13), 4586.

[53] Khajehoddin, S. A., Karimi-Ghartemani, M., & Ebrahimi, M. (2018). Grid-supporting inverters with improved dynamics. IEEE Transactions on Industrial Electronics, 66(5), 3655-3667.

[54] Musca, R., Vasile, A., & Zizzo, G. (2022). Grid-forming converters. A critical review of pilot projects and demonstrators. Renewable and Sustainable Energy Reviews, 165, 112551.

[55] Klein, M., Rogers, G. J., & Kundur, P. (1991). A fundamental study of inter-area oscillations in power systems. IEEE Transactions on power systems, 6(3), 914-921.

[56] Canizares, C., Fernandes, T., Geraldi, E., Gerin-Lajoie, L., Gibbard, M., Hiskens, I., ... & Vowles, D. (2016). Benchmark models for the analysis and control of small-signal oscillatory dynamics in power systems. IEEE Transactions on Power Systems, 32(1), 715-722.

[57] A. Berizzi, A. Bolzoni, A. Bosisio, V. Ilea, D. Marchesini, R. Perini, and A. Vicario, "Synthetic Inertia from Wind Turbines for Large System Stability," in Proceedings - 2020 IEEE International Conference on Environment and Electrical Engineering and 2020 IEEE Industrial and Commercial Power Systems Europe, EEEIC / I and CPS Europe 2020, 2020

[58] J. Zhu, J. Hu, W. Hung, C. Wang, X. Zhang, S. Bu, Q. Li, H. Urdal, and C. D. Booth, "Synthetic Inertia Control Strategy for Doubly Fed Induction Generator Wind Turbine Generators Using Lithium-Ion Supercapacitors," IEEE Trans. Energy Convers., vol. 33, no. 2, pp. 773–783, 2018

[59] J. A. Adu, J. D. Rios Penaloza, F. Napolitano, and F. Tossani, "Virtual Inertia in a Microgrid with Renewable Generation and a Battery Energy Storage System in Islanding Transition," in SyNERGY MED 2019 - 1st International Conference on Energy Transition in the Mediterranean Area, 2019.

[60] Y. Wang, J. Meng, X. Zhang, and L. Xu, "Control of PMSG-Based Wind Turbines for System Inertial Response and Power Oscillation Damping," IEEE Trans. Sustain. Energy, vol. 6, no. 2, pp. 565–574, 2015.

[61] J. Van De Vyver, J. D. M. De Kooning, B. Meersman, L. Vandevelde, and T. L. Vandoorn, "Droop Control as an Alternative Inertial Response Strategy for the Synthetic Inertia on Wind Turbines," IEEE Trans. Power Syst., vol. 31, no. 2, pp. 1129–1138, 2016.

[62] Y. K. Wu, W. H. Yang, Y. L. Hu, and P. Q. Dzung, "Frequency regulation at a wind farm using time-varying inertia and droop controls," IEEE Trans. Ind. Appl., vol. 55, no. 1, pp. 213–224, 2019.

[63] X. Zeng, T. Liu, S. Wang, Y. Dong, and Z. Chen, "Comprehensive Coordinated Control Strategy of PMSG-Based Wind Turbine for Providing Frequency Regulation Services," IEEE Access, vol. 7, pp. 63944–63953, 2019.

[64] Y. Li, Z. Xu, and K. P. Wong, “Advanced Control Strategies of PMSG-Based Wind Turbines for System Inertia Support,” IEEE Trans. Power Syst., vol. 32, no. 4, pp. 3027–3037, 2017.

[65] C. Pradhan, C. N. Bhende, and A. K. Samanta, “Adaptive virtual inertia-based frequency regulation in wind power systems,” Renew. Energy, vol. 115, pp. 558–574, Jan. 2018.

[66] Adu, J. A., Napolitano, F., Penaloza, J. D. R., Pontecorvo, T., & Tossani, F. (2020, June). Influence of Fast Frequency Response Services in DFIG-Based Wind Power Plants on Power Grids Stability. In 2020 IEEE International Conference on Environment and Electrical Engineering and 2020 IEEE Industrial and Commercial Power Systems Europe (EEEIC/I&CPS Europe) (pp. 1-6). IEEE.

[67] J. Ma, Y. Qiu, Y. Li, W. Zhang, Z. Song, and J. S. Thorp, “Research on the impact of DFIG virtual inertia control on power system small-signal stability considering the phase-locked loop,” IEEE Trans. Power Syst., vol. 32, no. 3, pp. 2094–2105, May 2017.

[68] E. Lucas, D. Campos-Gaona, and O. Anaya-Lara, “Assessing the impact of DFIG synthetic inertia provision on power system small-signal stability,” Energies, vol. 12, no. 18, 2019.

[69] W. Du, Q. Fu, and H. F. Wang, “Power System Small-Signal Angular Stability Affected by Virtual Synchronous Generators,” IEEE Trans. Power Syst., vol. 34, no. 4, pp. 3209–3219, 2019.

[70] J. Liu, Z. Yang, J. Yu, J. Huang, and W. Li, “Coordinated control parameter setting of DFIG wind farms with virtual inertia control,” Int. J. Electr. Power Energy Syst., vol. 122, no. February, p. 106167, 2020.

[71] Adu, J. A., Tossani, F., Pontecorvo, T., Ilea, V., Vicario, A., Conte, F., & D'Agostino, F. (2022, June). Coordinated Inertial Response Provision by Wind Turbine Generators: Effect on Power System Small-Signal Stability of the Sicilian Network. In 2022 IEEE International Conference on Environment and Electrical Engineering and 2022 IEEE Industrial and Commercial Power Systems Europe (EEEIC/I&CPS Europe) (pp. 1-6). IEEE.

[72] Adu, J. A., Berizzi, A., Conte, F., D’Agostino, F., Ilea, V., Napolitano, F., ... & Vicario, A. (2022). Power System Stability Analysis of the Sicilian Network in the 2050 OSMOSE Project Scenario. Energies, 15(10), 3517.

[73] Heggarty, T., Bourmaud, J. Y., Girard, R., & Kariniotakis, G. (2019). Multi-temporal assessment of power system flexibility requirement. Applied Energy, 238, 1327-1336.

[74] Göke, L., Weibezahn, J., & von Hirschhausen, C. (2023). A collective blueprint, not a crystal ball: How expectations and participation shape long-term energy scenarios. Energy Research & Social Science, 97, 102957.

[75] GAUDI’ portal, available online at https://www.terna.it/it/sistema-elettrico/gaudi. Accessed: 22-Sep-2021.

[76] Map of Sicily, 380 – 220 kV system, http://www.regione.sicilia.it.

[77] F. Barroco Fontes Cunha, C. Carani, C. A. Nucci, C. Castro, M. Santana Silva, and E. Andrade Torres, “Transitioning to a low carbon society through energy communities: Lessons learned from Brazil and Italy,” Energy Res. Soc. Sci., vol. 75, 2021.

[78] F. Cappellaro, G. D’Agosta, P. De Sabbata, F. Barroco, C. Carani, A. Borghetti, L. Lambertini, and C. A. Nucci, “Implementing energy transition and SDGs targets throughout energy community schemes,” *J. Urban Ecol.*, vol. 8, no. 1, 2022.

[79] User Device, Chain 2. Available online at https://www.e-distribuzione.it/open-meter/chain-2.html.

[80] Emoncms database. Available online at https://emoncms.org.

[81] OpenVPN. Available online at https://openvpn.net/.

[82] ForecastSolar PV forecast service. Available online at https://forecast.solar/.

[83] Solcast PV forecast service. Available online at https://solcast.com/.

[84] U. B. Tayab, A. Zia, F. Yang, J. Lu, and M. Kashif, “Short-term load forecasting for microgrid energy management system using hybrid HHO-FNN model with best-basis stationary wavelet packet transform,” *Energy*, vol. 203, p. 117857, Jul. 2020.

[85] Cielo, A., Margiaria, P., Lazzeroni, P., Mariuzzo, I., & Repetto, M. (2021). Renewable Energy Communities business models under the 2020 Italian regulation. Journal of Cleaner Production, 316, 128217.

[86] ARERA, *Deliberazione 4 agosto 2020 318/2020/R/EEL regolamentazione delle partite economiche relative all’energia condivisa da un gruppo di autoconsumatori di enregia rinnovabile che agiscono collettivamente*. 2020.

[87] Prevedi, A., Penaloza, J. D. R., Pontecorvo, T., Napolitano, F., Tossani, F., Borghetti, A., & Nucci, C. A. (2023, September). Optimal Operation of Renewable Energy Communities Through Battery Energy Systems: A Field Data-Driven Real-Time Simulation Study. In 2023 International Conference on Smart Energy Systems and Technologies (SEST) (pp. 1-6). IEEE.

[88] GSE, “Regole tecniche per l’attuazione delle disposizioni relative all’integrazione di sistemi di accumulo di energia elettrica nel sistema elettrico nazionale.” 2021.

[89] P. G. McLaren, R. Kuffel, R. Wierckx, J. Giesbrecht, and L. Arendt, “A real time digital simulator for testing relays,” *IEEE Trans. Power Deliv.*, vol. 7, no. 1, pp. 207–213, 1992.

[90] Opal-RT Technologies Inc., “RT-LAB User Guide.” Canada, 2015.

[91] M. O. Faruque, T. Strasser, G. Lauss, V. Jalili-Marandi, P. Forsyth, C. Dufour, V. Dinavahi, A. Monti, P. Kotsampopoulos, J. A. Martinez, K. Strunz, M. Saeedifard, X. Wang, D. Shearer, M. Paolone, R. Brandl, M. Matar, A. Davoudi, and R. Iravani, “Real-Time Simulation Technologies for Power Systems Design, Testing, and Analysis,” *IEEE Power Energy Technol. Syst. J.*, 2015

[92] Opal-RT Technologies Inc., "Artemis User Guide," Canada, 2017.

[93] "Gestore Mercati Energetici (GME)." Available online at https://www.mercatoelettrico.org/en/.